Modeling and Analysis of Ultrasound Propagation in Layered Medium

Joyoni Dey

dey+@cs.cmu.edu

CMU-RI-TR-99-26

August 1999

Department of Electrical and

Computer Engineering,

Carnegie Mellon University

Pittsburgh, PA 15213, USA

Submitted in partial fulfilment of the requirements for

the degree of Doctor of Philosophy

in Electrical and Computer Engineering

Thesis Committee

Takeo Kanade, chair

Jose' Moura

Steven Shafer, Microsoft Corporation,

Roman Kuc, Yale University

Contents

List of Figures

List of Tables

I dedicate this thesis to little Sanyashi, with his imaginative tricks and harsh street-language; to Danise, Tyron, Olivia, tough outside, yet sensitive and vulnerable to others' ignorance and pre-conceived notions; And to Rhonda and Imon, who found an answer - the spirit of resilience, the spirit, that says, look forward to life and never ever give up.

Abstract

For many medical applications of ultrasonic devices, it is often of interest to determine the distortion of ultrasound waves due to tissue layers of fat and muscle. Bending of the acoustic rays due to refraction at intermediate layers degrades image resolution, causes distortion and other artifacts in ultrasound images. In this work, ultrasound propagation in layered media is modeled analytically. Closed-form expressions are presented for the field amplitude of spherical waves for the following cases: (1) transmission through a three-layered media, (2) extension to transmission through multi-layered medium, (3) a special case of modeling received echoes from an interface through two layers. In our derivations, ray-acoustic approximations have been assumed. We show that ray-acoustic approximations are valid for wavelengths (relative to medium layer dimensions) of interest. The field amplitude is calculated by taking differentials of the rays to form flux tubes and algebraically calculating the ratios of flux-tube areas. We also take into account the frequency dependent attenuation due to absorption and backscattering loss in the media. The interfaces between media are assumed to be arbitrary shaped, but can be broken up into small planar segments. The resulting response can be extended to different aperture geometries and different beam formations by delaying and summing the result for the Huygen waves emanating from the points forming the aperture.

We have considered the inversion problem for the case of two layers on a reflective interface, where the layers are planar and parallel to the aperture. We showed that it is better to use demodulated versions of signal ouputs

than use the raw signals themselves to avoid local minima at regular intervals around the global minimum.

Validation experiments were performed using custom made tissue mimicking phantoms of fat and muscle and a steel-block. We fit the forward-model to the experimental data using Levenberg-Marquardt inversion and show results of the parameter recovery and the simulation results with the final parameters. For a 3 mm circular aperture transducer operating at 7 MHz, we obtained the RMS ratio of the experimental to the simulated echoes from two interfaces as 1.03 and 0.95 respectively.

Acknowledgments

I thank Takeo for his advice, his perspective, direction and guidance. I am grateful for his trust in me and thank him for allowing me the time and freedom to learn.

Heartiest thanks to Professors Roman Kuc and Omar Ghattas for their feedback and encouragement.

Many thanks to Professors Steve Shafer and Jose' Moura for their feedback and valuable time.

I thank Rajesh Gopakumar at Harvard University for his feedback and particularly for reviewing an earlier version of the forward model. I want to thank Anurag for his support, encouragement and being an ever-ready answering machine for my random C-questions ! Farhana for her discussions, suggestions and readiness to sound out details. Thanks to David LaRose for his guidance, direction and kind support during a most difficult time.

Thanks to PD (Priyadarshee Mathur sounds so formal) for his help in terminating transducer cables and trouble-shooting equipment.

And all the wonderful and unique friends I have had in Pittsburgh - I thank them - Usha, for her support and help during troubled times; Anurag for support throughout; Sita for all his help (during moves, during emergencies), for the RPMG and Spicmacay days; Shravan for showing us AID-ers what is important; Vidhya for all the wonderful musical evenings, and for those random astro-physics discussions; Girija for her brilliant and steady companionship in those puzzling days; Dimitris for the help with the PC, for all the puzzles and movies; and PD particularly for his Xmastermind! And

Lily-di for her affection and her wonderful dinners, bringing a whiff of home to Pittsburgh. Anit-da for his spirit and honesty and wry humor; Rhonda and Imon for cheering up Royal Plaza no end; My wonderful roommates who became such good friends - Sapna, practical, vivacious and very considerate. Ratnapriya, the little rebel, so full of life. I want to specially thank them for loving and taking care of Khoyeri whenever I was away.

Thanks to all the other friends and colleagues who have helped me, however briefly, with advice and a balanced perspective, Ruhul Quddus, Justin Boyan, Anqi Ye, Teck Khim, Mei Chen, Sundar Vedula, Prem Janardhan, Shyjan Mahamud, and all the others I might be missing.

And my sources of inspiration ? My ever-practical mother, so thorough and methodical, the best teacher I ever had; my indomitable elder sister, Damini; my cousin Ritwik, practical and brilliant; but above all, the "Demions" (and perhaps also the demons!) of my life - Baba, always daring to be original and my cranky twin sister, so involved in her abstract world of mathematics. Thanks to Baba and Meji for defining for me what is most important in life.

Last but not the least, Khoyeri (aka Khoglu), my dogged soulmate, so silly, patient and understanding, the sweetest friend a person can have.

Thank you all !

Chapter 1

Introduction

Ultrasound is a very useful modality for many diagnostic medical applications. It is non-invasive and cheap. In certain applications such as fetal imaging, it is the only modality considered safe. It can also propagate fast and can be processed fast enough to be able to image moving organs such as the heart. It is a very useful tool for locating tumors as well as a guidance tool for biopsy. In addition to diagnostic applications, it is used for therapeutic purposes as well. Due to its inexpensive and non-invasive nature, it is becoming increasingly popular for more diverse applications such as intra-operative registration for computer-aided surgery.

1.1 The Problem

For many medical applications of ultrasonic devices, it is important to determine the distortion of ultrasound waves due to tissue inhomogeneities.

Investigating the propagation of ultrasound through layered media is important because the soft tissue in various regions of the human body is composed of multiple layers.

Sound velocity in different media varies considerably. For example, the propagation velocity in a typical fat layer is around $1470m/sec$ whereas the velocity in muscle is around $1570m/sec$. State-of-the-art ultrasound scanners, however, assume a homogeneous soft-tissue medium as well as a uniform longitudinal velocity of propagation ($1540m/sec$). In comparison, within-medium variation due to temperature, compression, and various other factors is usually less significant.

Presence of layered inhomogenieties result in degradation of resolution as well as cause geometric distortions of structures and other artifacts in ultrasound images.

We demonstrate a simple problem in Figure 1.1. In the top diagram we show a unfocussed transducer transmitting and receiving echoes from an interface parallel to the transducer aperture and at depth D from it. Suppose we are interested in recovering the depth of the interface, from time-of-flight of ultrasonic echoes. We show (by simulation) potential errors due to using a single average velocity of sound when we actually have intermediate layers with different sound speed. We assume typical values of velocities and layer thicknesses. The depth $D = 25mm$. We have two intervening planar layers with sound speed of $C_1 = 1.47mm/\mu s$ and $C_2 = 1.57mm/\mu s$, which are typical values of sound speed in fat and muscle. The depth of the first interface is assumed $15mm$ at the axial-center. We vary the angle θ in our simulation. The transducer is assumed to send Gaussian pulses modulated with carrier frequency at 1 MHz.

Figure 1.1 bottom plots shows the echoes received from the interfaces.

We show the close up of the two echoes in Figure 1.2.

Considering the plot shown in the rightside of Figure 1.2 we show two echoes (in dashed lines) from the second interface for two different values of θ. The first one is the echo when the angle θ is zero (the case when the intermediate interface is parallel to the aperture). The second one is when the interface is tilted at $\theta = 30$. The time signal is scaled by the standard velocity of $1.54mm/\mu s$, to give depth in mm. The correct depth is $D = 25mm$. We see that there is about $0.8mm$ error in the depth estimation for $\theta = 0$ case. For $\theta = 30deg$, the error is more. The echo shown in solid line is just reference of where the echoes would have been located if the medium is actually homogeneous with sound speed at the assumed $1.54mm/\mu s$. The start of this reference echo gives the right depth $D = 25mm$.

The plot in Figure 1.2 to the left shows the echo from the first interface. This can be used for rudimentary corrections to the velocity scaling for some simple parallel-interface cases. However for general media interface geometries, this may not be possible. For example in the $\theta = 30deg$ case, the first echo disappears. For general curved interfaces, more sophisticated estimation of the interfaces are necessary. Prior knowledge of the number of layers is needed.

The above was a simple illustration of how the echo positions are affected by intermediate layers and could lead to depth estimation errors.

An application of interest where one needs accurate estimation of the depths is registration of intra-operative ultrasound images and pre-operative

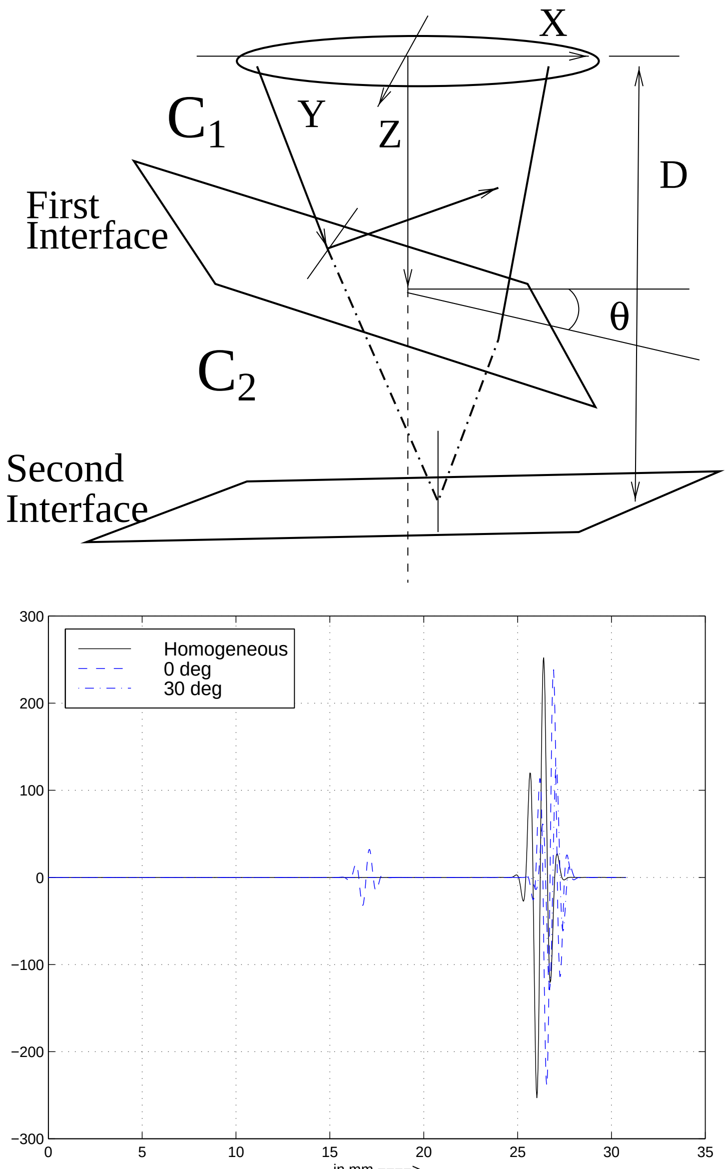

Figure 1.1: Inferring depth from simulated echoes from interfaces

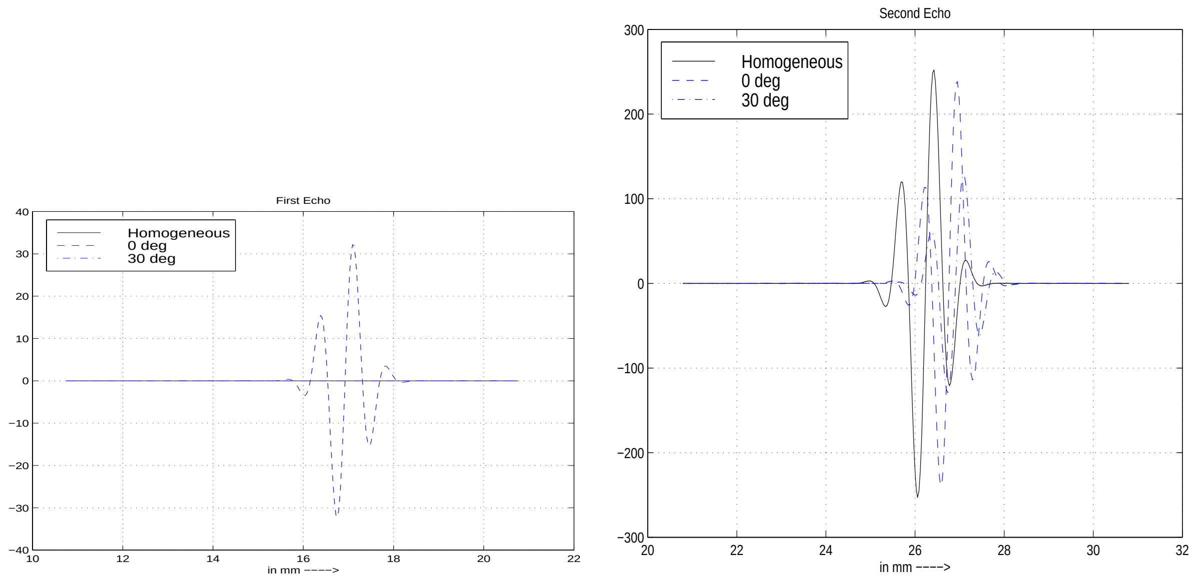

Figure 1.2: Close-up of echoes from the interfaces

Intra-operative Ultrasound Image **Pre-operative CT Data**

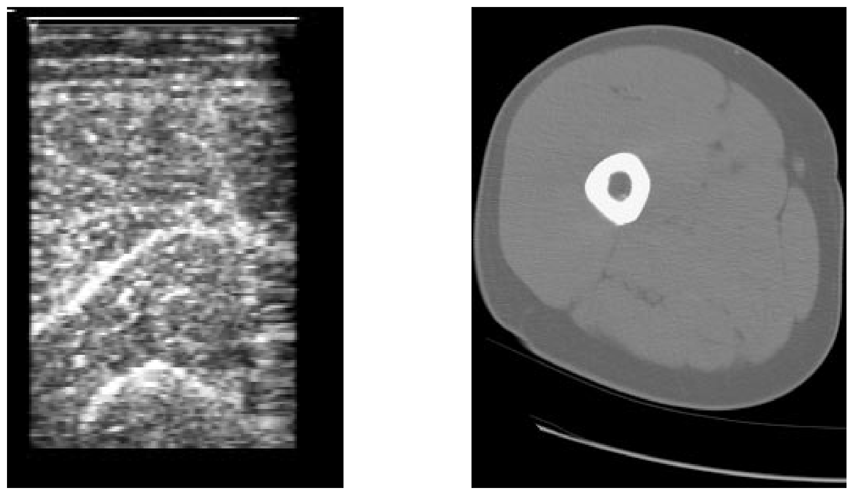

Figure 1.3: Ultrasound image and CT slice of human femur

CT slices. Figure 1.3 (left) shows an ultrasound image of a human femur bone (the semi-circular reflection at the bottom). There is an intervening interface, presumed to be separating fat and muscle. This intervening layers causes distortion in the bone shape as well as the depth.

So we should perform some processing step to “correct” for these distortions before proceeding with the registration, shown in Figure 1.4.

For other applications such as therapeutic ultrasonic applications, good localization of the beam is needed. Bending of acoustic rays due to refraction at layer boundaries can increase the lateral beam width and can cause shifts in the beams (which could be as high as a few millimeters depending on wavelength used and the depth of the tissue layers). These effects are shown schematically in Figure 1.5.

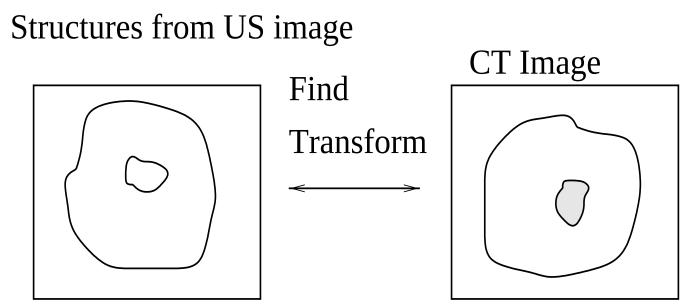

Figure 1.4: Registration of Ultrasound and CT

The top digram in Figure 1.5 shows a focussed beam in a homogeneous medium with a velocity of propagation $1540m/sec$. Figure 1.5 shows how the beam would shift away from the axis and broaden. The shift is more severe with the tilt angle of the intervening interface.

We see therefore a need to investigate, estimate and correct for the distortions. The exact parameters we are interested in estimating depends on the application.

1.2 Approach

In this thesis, we have taken the general approach of modeling and inversion to correct for distortion or artifacts.

We developed a general forward model of the propagation of ultrasound waves in the presence of layered inhomogeneities. We considered the inversion problem for estimating the correct depths for the case of two layers on a reflective interface, where the layers are planar and parallel to the aperture.

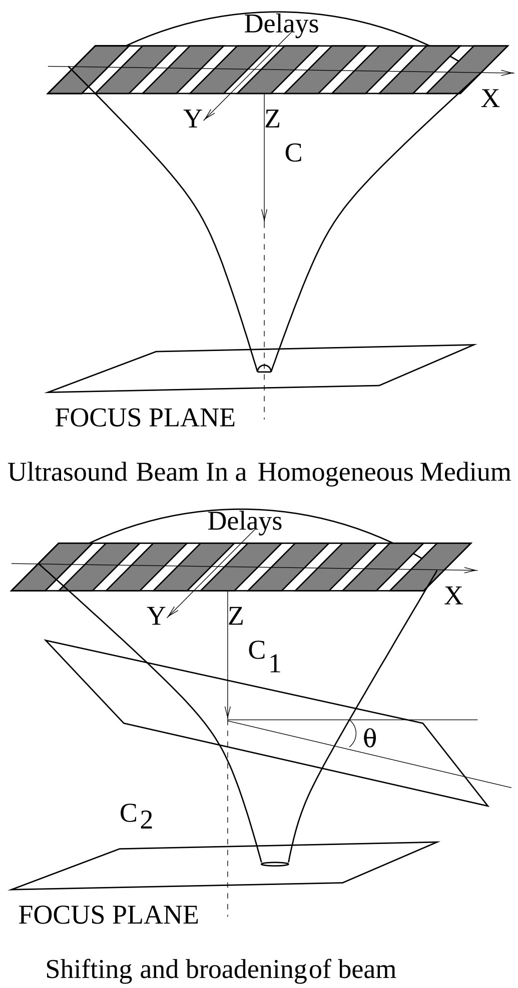

Figure 1.5: Effect of inhomogeneity on ultrasonic beam

1.2.1 Forward Model

We have developed an analytical model, under ray-tracing approximations, for ultrasound longitudinal propagation in multi-skewed media. We have developed closed form expressions for the field amplitude of hemi-spherical waves for: (1) transmission through a three-layered media, (2) extension to transmission through multi-layered medium, (3) a special case of modelling the received echoes from a reflective media under two intermediate layers. This last case is of special interest to us because it is similar to imaging the bone under intermediate fat-muscle layers. We are particularly interested in this case as it would be useful to be able to non-invasively track skeletal bones intra-operatively (through fat and muscle layers). In the derivations of the field for these cases, the interfaces between media are assumed to be arbitrary shaped as long as they can be broken up into small planar segments.

We first derived the case for a point source emitting a spherical wave. We use a ray-tracing approximation and derive the amplitude and the phase for each ray. To derive the amplitude, we derive (in closed form) the attenuation due to spreading of the wave within each medium and apply boundary conditions to each ray at media interfaces. We calculated the spreading factor within each medium algebraically by taking differentials of the rays and the points of intersections of the rays at the interfaces. Then we calculated the cross-section areas of the flux-tubes along the wavefront (locally perpendicular to the rays). We also take into account the frequency dependent attenuation in the medium, due to absorption losses and backscattering. We did not consider losses due to viscosity since this loss can be usually neglected.

This result can be extended to different aperture geometries and different beam formations by delaying and summing the result for the Huygen waves emanating from each point-source forming the aperture. We have extended the analysis to broad-band pulses. Each ray "carries" a pulse with a particular amplitude and delay specific to the ray and the different pulses interfere.

The work most similar to this in terms of generality is that of [1]. However in that work, the attenuation of the rays due to the spreading of the wave have been determined numerically while here we have attempted to develop an analytical form for the propagation with ray-acoustic approximations.

An analytical model has potential advantages over a numerical model. First, when determining the amplitudes of each of the rays, the accuracy in numerical methods could vary with the implementation and with the wave-front complexity. The analytical method is more consistent and potentially more accurate. Second, it is usually relatively easier and faster to invert as we can obtain closed form derivative expressions. In particular we do not have to evaluate the forward function multiple times by perturbing every parameter to determine the derivatives. Ease of inversion is important as a successful inversion of the model would allow us to recover parameters of interest such layer-boundaries and other physical parameters such as velocities, densities etc.

1.2.2 Simulator

We have used the model to develop a simulator (in C) for circular aperture transducers as well as linear-arrays for different media geometries. To validate the model, we performed real-life experiments on parallel tissue-mimicking phantoms with nominally known thicknesses.

1.2.3 Numerical Inversion of Model for A Simple Case

We considered the inversion problem for the simple case of two layers on a reflective interface, where the layers are planar and parallel to the aperture. We are interested in recovering the depths of the planar interfaces. For this simple two parameter case, we analyzed the error function to be minimized. We found an inherent problem of local minima at regular intervals of wavelength very near the global minimum because of the modulation of the ultrasound signals. We demodulated the signals and obtained a smoother objective function. Finally, we performed an iterative Levenberg-Marquardt inversion illustrated in diagram Figure 1.6.

The data signal is obtained from real-life experiment on tissue mimicking phantoms. In the first pass we use the the demodulated versions of the data and simulator output and obtained fast convergence to near the global minimum. For the final fine-tuning we used the modulated signals.

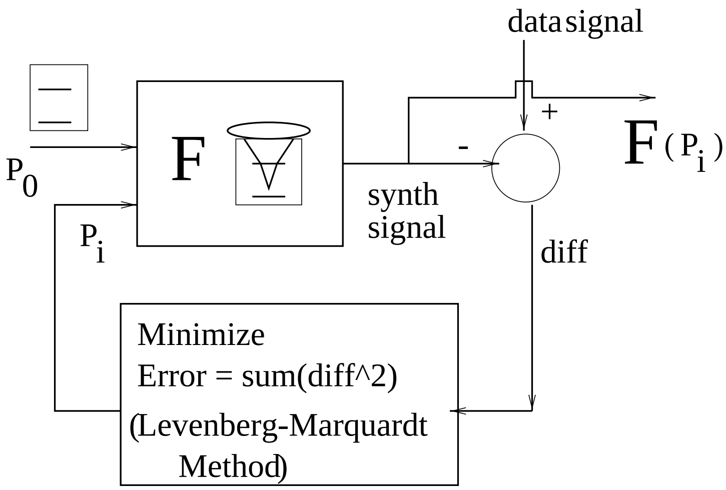

Figure 1.6: Iterative Inversion

1.3 Applicability

The model derived here could be used to describe the distorting effect of layered media for fairly common cases. Much of the human body is layered. We have assumed homogeneity within the individual layers. This, while somewhat restricting, is still an improvement over the state-of-the-art scanners, where the mechanism works under the assumption that the whole medium is homogeneous. Also, the within layer variations are usually not as significant as the across-medium variation. We have also assumed longitudinal propagation of sound, which is a good approximation for most soft-tissues.

For the transducer frequencies commonly used (1-10 MHz), this model is valid for near-field (and far-field) operations.

The model can work as long as the ray-tracing approximation holds. For this, the dimensions of the imaging system and the media structures should be large compared to the wavelength [2, 3, 4]. Some calculations in Chapter 8 show that the ray-tracing approximation is not very restricting. To quote a few calculations, for example, as long as we are interested in points at least at depth $z >> 0.2017mm$ away from the interface, we can use the ray-tracing approximation for the fat-muscle interface, for a 3.5 MHz transducer. The shorter the wavelength used, the less restricting is this criterion. [For a 7.5 MHz transducer, the required depth is $z >> 0.0941mm$]. The usual range of distances involved for the applications of interest to us are about 10 to 50 mm.

In Chapter 8 of this report we discuss some general applicability, the advantages and limitations of the model in more detail.

1.4 Example

An example for the use of the proposed model would be computer-aided Total Hip Replacement Surgery. For this application, it would be very useful if intra-operatively obtained ultrasound linear array images of bone could be used for accurate registration of pre-operative data. Ultrasound is a preferred modality as it is less invasive than existing registration techniques. For accurate registration however, it is necessary that the geometric distortion due to the layered inhomogeneities be estimated and compensated for. In Figures 1.7 and 1.8 we show a potential use for a good model for the propagation of ultrasound in layered media for registration purposes in an orthopedic surgery.

As explained schematically in Figure 1.7, if we have a comprehensive forward model of the imaging, we can attempt to invert the model and recover the parameters of interest (such as the boundaries between interfaces and other physical parameters such as velocities, densities etc). Then as a second step, in Figure 1.7 (b) we match and align the rigid structures (such as the bone surface) with pre-operative data and obtain the transformation.

Figure 1.8 shows another approach where we obtain the parameters of interest from the pre-operative data and simulate an "expected" ultrasound image based on these parameters. Note that to obtain the parameters, segmentation of the pre-operative data is necessary. We can then match and try to align the "expected" data and with the intra-operatively obtained ultrasound data. This approach assumes that the soft-tissue interfaces are not too deformed between the times of the pre-operative imaging of the patient and the actual surgery.

1.5 Related Work in Ultrasound Propagation in Stratified Layers

There has been considerable prior work for modeling ultrasound propagation in layered media [2, 1, 5, 6, 7, 8, 9]. In [7, 6, 8], a ray-tracing approach is taken to evaluate the beam distortion when propagating between two media. Experimentally validated simulation results have been presented in [7] for a 3.5 MHz, array-transducer geometrically focussed at 100 mm. Results show beam displacements as high as 1.5 mm for some cases where there is asymmetry of the interface with respect to the beam axis. The theoretical

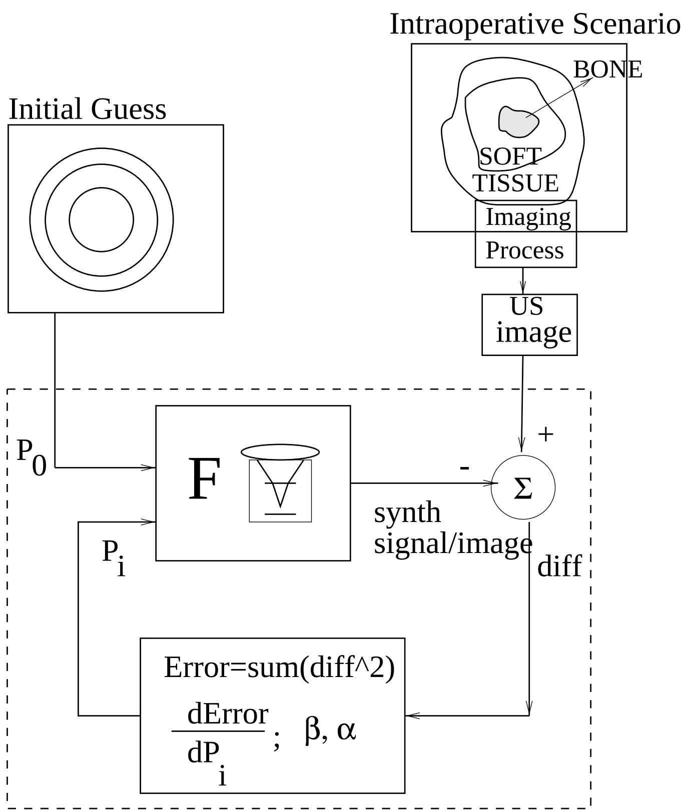

(a) Recover the Structure Intra-Opteratively

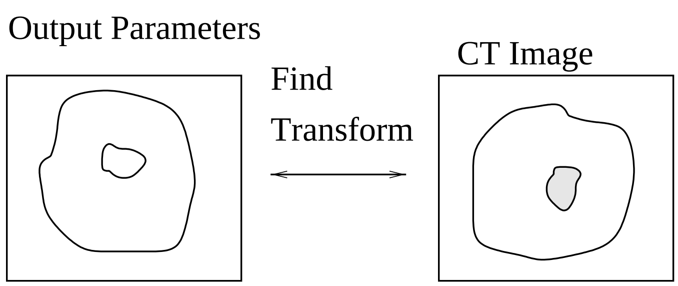

(b) Register with Pre-operative Data

Figure 1.7: **An Example Use of an Ultrasound Model**

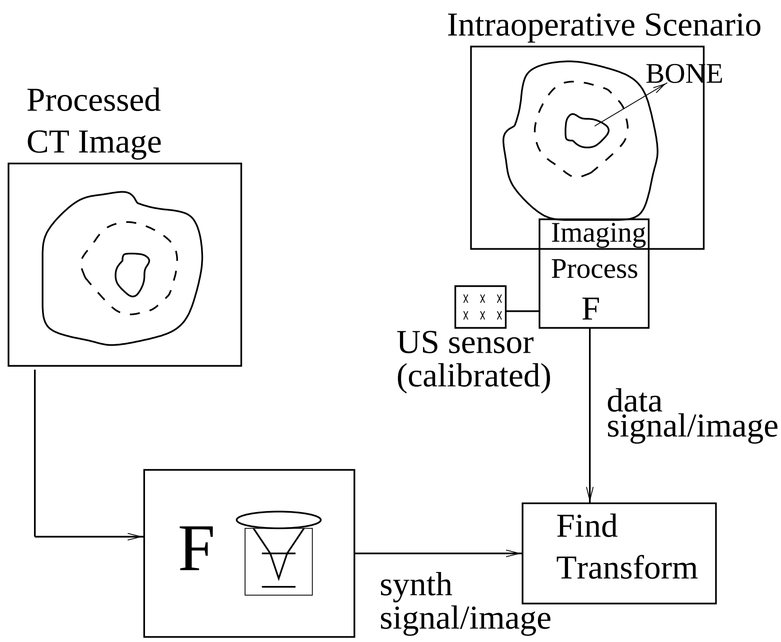

Figure 1.8: **Another Approach: Prior Use of Model in CT/MRI Images**

approximations as detailed in [7] involve assuming that for each element of the array, the region of interest is the far-field with respect to the element-widths and the near-field with respect to the element heights. The azimuth angle of each ray is used to find the directivity-factor due to the baffle, and the path-lengths of the rays in each medium are used for the range spreading.

In [1], the ray-tracing approximation has been extended to refraction and reflection at multiple interfaces, considering propagation through multiple media. Furthermore, absorption loss in the medium has been also considered. For each spherical wave, the resulting attenuation has three-factors, first is the attenuation for the range "spreading of the wave", second due to the absorption loss and the third, the attenuation due to reflection of energy at previous interfaces. The last two factors have been rigorously derived. The first, range spreading factor has been determined numerically, by perturbing each ray slightly in direction and forming the ray-tube. The numerically-calculated relative cross-sectional areas of the ray-tubes gives the broadening-factor.

In [9], experiments have been done to test phase-aberration due to refraction effects on planar tissue layers, parallel to the aperture. Both fat/organ as well as skull/brain interfaces have been considered. It shows even for a symmetric interface, the skull/brain planar interface degrades resolution and introduces geometric distortion.

The exact form of the distortion that a spherical wave undergoes after refraction at an interface under ray-tracing approximations, is given in [2, 3]. This is described in detail in the next chapter. This analysis assumes a planar interface.

In the present work we derive a theoretical model for more general media geometries.

1.6 Contents

In the next chapter, we first give the background theory relevant to this work.

In Chapter 3, we present the derivation of our model for sound propagation in three-layered media and then extend them to multi-layered media.

In Chapter 4, we present our derivations for a special case of modeling echoes received from an interface under two layers. We show that as far as the field amplitude is concerned, this case simply transforms into a case of three-layered media.

In Chapter 5, we describe the simulator and a validation experiment on custom-made phantoms, mimicking fat and muscle, using 7.5 MHz single element circular-aperture ultrasound transducer.

In Chapter 6, we consider inversion of the model for a simple two-parameter case. We investigated the objective function and found some of the inherent problems. One such problem was that of local minima at regular intervals due to modulation of the signals. We describe a demodulation scheme to overcome this problem.

Chapter 7, shows the inversion results on the experimental data on custom-made phantoms, mimicking fat and muscle, using 7.5 MHz single element circular-aperture ultrasound transducer.

In the last chapter we summarize our results, mention the contributions of the work, discuss the assumptions and possible future directions.

Chapter 2

Background

This chapter provides some background of ultrasound propagation and imaging.

In Section (2.1) we give the theoretical background of the different aperture integrals used to describe the field propagating into a homogeneous medium, in terms of the excited field at the aperture. The Raleigh-integral for a transducer in a rigid-baffle is of particular interest to us, in presence of absorption loss.

In Section (2.2), we give the background material for the full closed form equation of the field upon reflection and refraction of a spherical wave at a single boundary [2], with and without the ray-tracing approximation. This is derived in great detail in [2] for evaluating the field propagating through two media, separated by an interface.

2.1 Ultrasonic Transducers in Homogeneous Medium

2.1.1 Aperture Equation for monochromatic waves

The wave-equation guiding the propagation of a longitudinal wave in a loss-less homogeneous medium is given by [10, 11, 3, 12, 2]

$$\nabla^2 \phi = \frac{1}{C^2} \frac{\partial^2 \phi}{\partial t^2} \tag{2.1}$$

where ϕ is a scalar potential function of x, y, z, t, whose gradient is the longitudinal particle displacement, i.e, $\nabla \phi = \mathbf{u}$ where $\mathbf{u}$ is the displacement vector. C is the longitudinal-wave propagation velocity. From ϕ, all the other physical variables such as displacement and pressure, can be deduced.

For a monochromatic wave, we get the equivalent Helmholtz equation, [10, 11, 3, 12, 2]

$$\nabla^2 \Phi(r) + k^2 \Phi(r) = 0 \tag{2.2}$$

where $k = \frac{2\pi}{\lambda}$, where $\lambda = C/f$ where f is the frequency of the wave.

In [10] details are given how this equation can be solved with different Green's functions, depending on the type of baffle the flat-piston transducer is in.

For a rigid-baffle, as the name suggests, the z-component of the displacement is $u_z = 0$ on the baffle. And for a pressure-release baffle the pressure is zero on the baffle. In a later section we give examples of Rigid-Baffle and Pressure-release Baffle.

These two conditions would lead to two different Green's functions leading to two possible solutions of the Helmholtz equation [10].

The first solution (and the solution we are interested in), giving the response at any point in a homogeneous medium due an aperture excited at a single frequency is given by a linear sum given by,

$$\Phi(P_m) = \frac{1}{2\pi} \int \int u_z(P_a) \frac{\exp(-jkr_{am})}{r_{am}} dS \tag{2.3}$$

where $k = \frac{2\pi}{\lambda}$, where $\lambda = \frac{C}{f}$ where, f is the frequency of the harmonic wave. r_{am} denotes the radial distance between points "a" (on the aperture) and "m" (inside the medium). The $u_z(P_a)$ is the aperture transmittance. This transmittance can potentially have appropriate complex weighting functions (created by lenses in optics/acoustics, or electronically in acoustics applications) creating the delays needed to focus and steer the beam emanating from the aperture. The function u_z is zero out side the transducer (i.e., on the baffle), thus this solution corresponds to a rigid-baffle [10].

The physical meaning of equation 2.3 is that the response at any point in the media, is given by the sum of all the spherical harmonic waves (Huygen's waves) emanating from the point sources composing the aperture, weighted and delayed by the appropriate transmittance of the aperture at that point.

The second solution is appropriate for a **pressure-release baffle**, for which the pressure is zero on the baffle [10]. For this case, the aperture equation is,

$$\Phi(P_m) = \frac{jk}{2\pi} \int \int \Phi(P_a) \frac{\exp(-jkr_{am})(1 + 1/jkr_{am})}{r_{am}} \cos(\hat{n}, \hat{r_{am}}) dS \tag{2.4}$$

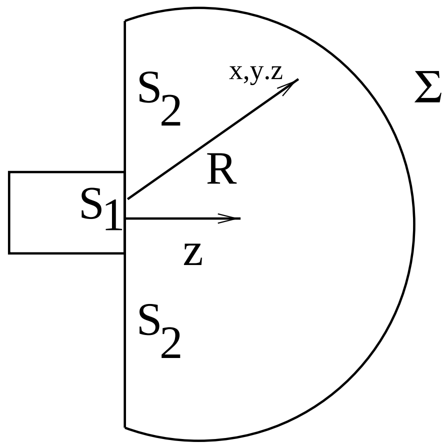

Figure 2.1: **Piston Tranducer in a Baffle**

For regions where the radius $r_{am} >> \lambda$, we can ignore kr_{am} with respect to 1 and get,

$$\Phi(P_m) = \frac{jk}{2\pi} \int\int \Phi(P_a) \frac{\exp(-jkr_{am})}{r_{am}} \cos(\hat{n}, \hat{r_{am}}) dS \qquad (2.5)$$

This equation has the added cosine factor, called the directivity function or the obliquity function.

2.1.2 Rigid-Baffle vs. Pressure-release Baffle

The transducer surface of area S_1 in a baffle of area S_2 is illustrated in Figure 2.1, reproduced from [10], Figure 3.1.1. $\sum$ is the rest of the enclosing surface of the volume of the medium.

Examples of rigid-baffle and pressure-release baffle are given in [10], at the end of Section 3.2.1 (Pg. 171). A transducer in water, surrounded by a metal disk whose impedance is much higher than that of water, would be one in a rigid-baffle. A transducer in a pressure-release baffle would be a small transducer (dimensions of one wavelength or less) or one element of an array of identical transducers, separated by a distance of a wavelength or more, separated from a water-bath, by a Mylar film, such that there is air on one side of the film and water on the other side.

An ultrasound array has an angular response somewhere in between that of a source in a rigid-baffle and that in a pressure-release baffle [1]. In this work, as in most simulations, we have assumed the Raleigh Integral (that is the equation for a rigid-baffle) given in Equation 2.6. This gives good results near the axis.

More details on baffled planar pistons, are found in the excellent paper [13] or [14].

2.1.3 Aperture Equation for a Pulse

In many cases, the incident field is not a monochromatic wave, but a pulse, with a range of frequencies. The generalization of the Rayleigh-Sommerfeld theory to these non-monochromatic waves is given in Section 3-5 in [11].

For a **rigid baffle**, the phase in the Equation 2.3 gives the time delays of the pulses, resulting in the so-called *Raleigh integral*,

$$\phi(P_m, t) = -\frac{1}{2\pi} \int\int \frac{1}{r_{am}} u_z(P_a, t - \frac{r_{am}}{C}) dS \tag{2.6}$$

But for the pressure-release baffle, the $\frac{1}{\lambda} = \frac{f}{C}$ term in the Equation 2.5 results in another interesting effect that disturbance in the medium is the time derivative of the disturbance in the aperture (apart from the delay).

Thus for a **pressure-release baffle** the disturbance in the medium is given by,

$$\phi(P_m, t) = \int\int \frac{\frac{d}{dt}\phi(P_a, t - \frac{r_{am}}{c})}{2\pi C r_{am}} \cos(\hat{n}, \hat{r_{am}}) dS \tag{2.7}$$

2.1.4 Linear-Arrays : focussing and steering

Different aperture transmittance functions can be applied to focus and steer the beam emanating from an aperture. The concepts are similar to focussing lens in optics [11]. For acoustical applications, since sound velocities are much lower than the electronic delaying speeds, the aperture can be broken up into little elements and each element can be delay-triggered according to what sort of beam is needed. The mathematical details can be found in many books and papers, such as [11, 10, 15, 16, 17], to cite a few.

Here we briefly give the intuitive idea behind the focussing. To focus at a point $z = r_f$, a curve given by $u_z(P_a) = \exp(-jkr_f)$ is required across the aperture. That is, instead the triggering all of the elements of the array at once, they are triggered with delays such that, for a uniform known velocity of the medium, the waves from all the elements would reach the point of focus in phase at the same instant. The delays would exactly compensate for the path-differences. Figure 2.2 shows focussing the aperture (composed of small rectangular elements) when transmitting.

There could be focussing during receiving as well, shown in Figure 2.3. The wave reaching "R" is scattered or reflected back. The signal coming back reaches the element just above it first, and the other elements later,

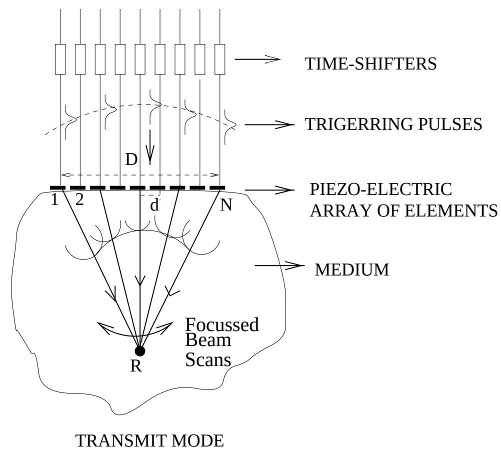

Figure 2.2: **Transmit Focus**

delayed by the path-differences. Hence the signals received are delayed (by the same curve as on transmit-focus) according to the path-differences again and added in phase.

The focussed beam can be steered to right/left as well, if we add a "linear" delay across the aperture in addition to the focussing-delays (which are almost "quadratic"-delays for focussing distance large compared to the aperture dimensions). Refer to Figure 2.4.

2.1.5 Homogeneous non-viscous medium with absorption loss

To consider absorption loss, the state equation used to derive the wave-equation can be modified as shown in [1] to incorporate absorption loss [1].

[1]The other two equations that are used to derive the wave-equation are the conservation of mass and momentum. For fluids with viscous loss, the momentum conservation equation

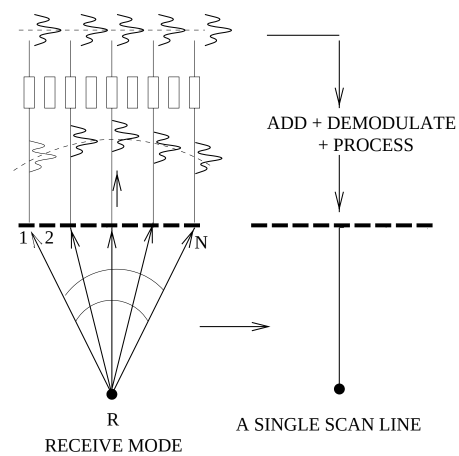

Figure 2.3: **“Listen” in Focus**

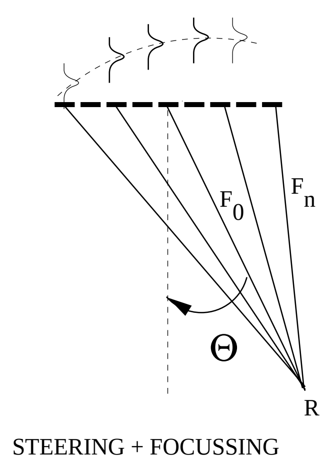

Figure 2.4: **Steering and Focussing**

The effect is that the k in the Helmholtz Equation 2.2 is complex as shown in [1, 2]. The complex k results in a factor $e^{-\mu r_{am}}$ multiplied to the *intensities*. Here μ is given by $\mu = RK\frac{\omega^2}{c}$, where K is the compressibility and R (which maybe a function of frequency) is the proportionality factor relating the rate of change of the normalized mass-density, to the energy absorbed (and transformed to heat) [1].

For multiple layers, under ray-tracing approximation, the absorption loss results in the intensities getting multiplied by a series of exponentials, i.e, $e^{-(\mu_1 L_1 + \mu_2 L_2 + \ldots)}$, where $L_1, L_2 \ldots$ are the distances travelled by the ray in successive media.

2.2 Ultrasound Propagation in Planar Layered Medium for an Incident Spherical Wave

We have considered propagation in a homogeneous medium. Now we are interested in propagation in a layered medium.

For the homogeneous case, the aperture Equations 2.3 and 2.5 are summing up the responses of the spherical waves emanating from each point in the aperture. When there is an impedance difference in the media the spherical waves get reflected and refracted.

It is of interest therefore to see what happens to a spherical wave upon

has to be modified. This effect is not considered in this work.

reflection and refraction at a planar boundary. This case has been considered in fullest detail in [2].

We refer to Figures 2.5 and Figure 2.6 to consider reflection and refraction respectively.

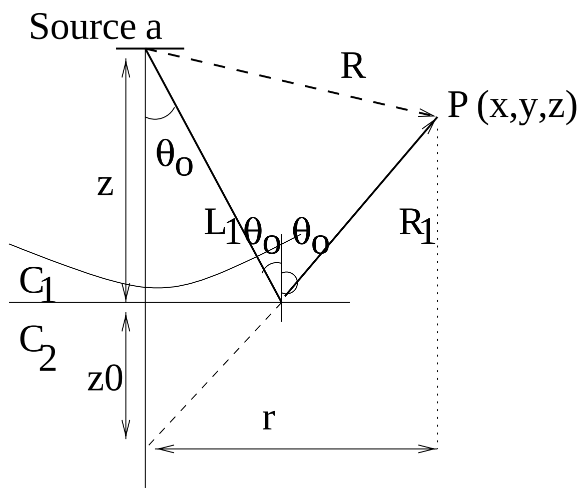

Figure 2.5: **Reflection a of Spherical Wave**

2.2.1 Exact Waveforms

The exact waveforms after refraction and reflection for a single intermediate layer is derived in [2]. The approach was to break up the spherical wave into a series of plane waves (Equations 26.17 (or 26.19) in [2]) and apply the boundary conditions for reflection and refraction for each of these plane waves.

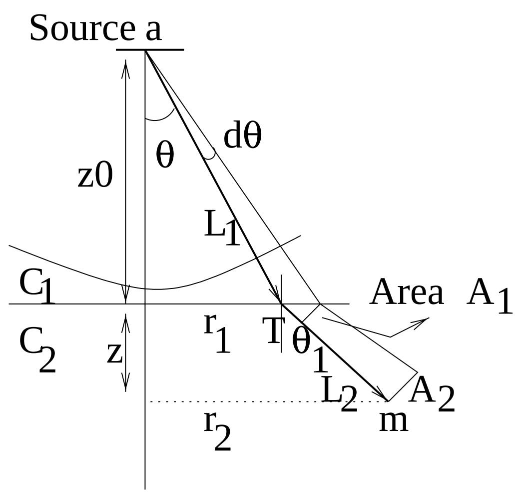

Figure 2.6: **Refraction of Spherical Wave**

Reflection

The reflected waveform is found in [2], Equation 26.27, as

$$G_{refl}(P) = (ik/2)\int_{-\pi/2+i\infty}^{\pi/2-i\infty} H_0^{(1)}(u)e^{ik(z+z_0)\cos\theta}V(\theta)\sin\theta d\theta \tag{2.8}$$

where, $H_0^{(1)}(u)$ is the Hankel function of first kind, and the argument $u = kr\sin\theta$. $V(\theta)$ is the reflection coeficient given by

$$V(\theta) = \frac{m\cos\theta - \sqrt{n^2 - \sin^2\theta}}{m\cos\theta + \sqrt{n^2 - \sin^2\theta}} \tag{2.9}$$

The total waveform at a point P in the first media is the sum of the wave directly incident on P and the reflected wave,

$$G_{total}(P) = \frac{e^{ikR}}{R} + G_{refl}(P) \tag{2.10}$$

Refraction

The refracted waveform is found in [2], Page 280, as

$$
\begin{aligned}
G_{refr}(P) \;&=\; \frac{ik}{2\pi m}\int_0^{\pi/2-i\infty}\int_0^{2\pi}\exp[i(k(x\cos\phi+y\sin\phi)\sin\theta \\
&\quad +kz_0\cos\theta+k_1 z\cos\theta_1)](1+V(\theta))\sin\theta d\theta d\phi \qquad (2.11)
\end{aligned}
$$

2.2.2 Ray-Tracing approximation and correction terms

This section gives an approximation of the exact-form for a spherical wave after it undergoes reflection and refraction at a planar boundary.

Different approximations of the exact equations can be obtained as derived in Section 27-28 and Section 32 of the book [2].

Reflection

When we $1/(kR_1)^2 << 1$, the approximate **reflected wave** is (from Equation 28.13 in [2]).

$$G_{refl}(P) = \frac{e^{jk_1R_1}}{R_1}[V(\theta_0) - jN/kR_1] \qquad (2.12)$$

where

$$N = \frac{1}{2}[V''(\theta_0) + V'(\theta_0)\cot\theta_0] \qquad (2.13)$$

where $V'(\theta_0)$ and $V''(\theta_0)$ are first and second derivatives of the reflection coefficient with respect to θ (evaluated at θ_0).

The first term, $G_{refl}(P) = \frac{e^{jk_1R_1}}{R_1}V(\theta_0)$ gives the **ray-tracing approximation.** This approximation indicates the reflection coefficient of the spherical wave is the same as that of the component plane waves. The physical structure of the reflected wave under ray-tracing approximation is spherical, as can be seen from the equation $G_{refl}(P) = \frac{e^{jk_1R_1}}{R_1}V(\theta_0)$, as well as deduced from the geometry. The other physical interpretation is that this approximation means that the field at the observation point P in Figure 2.5 is composed of mainly the component plane waves close to $\theta = \theta_0$.

The "correction term" is important only if the source and the receiver are close to the boundary, compared to the wavelength [2].

Refraction

The refracted wave with geometric-optics approximation and the first correction term are given for $n > 1$ and $n < 1$ in Equations 32.11 and 32.12 in [2], not reproduced here.

The criterion under which the "correction" term can be neglected are given as follows.

Referring to Figure 2.6, for $n > 1$, geometric-optics criteria would be valid if the elevation of the source were high enough from the boundary compared to the wavelength. The position of the observation point position is not so restricted.

$$k_1 z_0 >> \frac{m}{\sqrt{n^2 - 1}} \tag{2.14}$$

where $m = \rho_2/\rho_1$ and $n = C_1/C_2$ (where ρ denotes the density and C

denotes velocity, n is the relative refractive index).

However, for $n < 1$, the observation point needs to be far from the boundary, while the position of the source is not that restricted.

$$k_1 z >> \frac{1}{\sqrt{1-n^2}} \tag{2.15}$$

The approximate derivation of a spherical-wave after refraction is derived in Eqn. 32.8, page 279 of [2] (as well as in [3], page 411).

In [2] (or [3]) this is derived from a geometric viewpoint by taking a ray and perturbing it by $d\theta$ as shown in Figure 2.6. The proof is not reproduced here, but the main idea behind the derivation of the *amplitude* is that at the boundary, one applies the boundary conditions (continuity of the total wave above and below) to get the relationship between the waves just above and just below T in Figure 2.6. In the second medium, there is attenuation due to "spreading of the wave" given by the conservation of energy in annular-regions swept by Area A_1 and A_2, that is, the amplitude "drop" between point T in the medium and the point m is given by $\sqrt{\frac{2\pi r_2 A_2}{2\pi r_1 A_1}}$. These concepts are adopted in the next section where we derive the closed form amplitude for the more general cases. The *phase* is given simply as the $\exp(jk_1L_1 + jk_2L_2) = \exp[jk_1(L_1 + nL_2)]$, that is the delays in the time domain are simply the path-lengths in the two media divided by their corresponding velocities. The resulting waveform is given by,

$$G(P_m) = A(P_a, \theta, n) \exp(jk_1L_1 + jk_2L_2) \tag{2.16}$$

The amplitude is given by

$$A(P_a, \theta, n) = \frac{2\sqrt{\sin\theta}\exp[jk_1(L_1 + nL_2)]}{(m\cos\theta + n\cos\theta_1)\sqrt{[L_1\sin\theta + (L_2)\sin\theta_1][L_1\cos^{-2}\theta + \frac{L_2}{n}\cos^{-2}\theta_1]}} \tag{2.17}$$

Note that the final result in [3] (Equation 8-7.7) and [2] (Equation 32.8) are slightly different in that there is a factor of density ratio $m = \rho_2/\rho_1$ in [3] that is absent in [2]. This is because in the former, the variable of interest is pressure, while in the other it is velocity potential. The analysis are identical except that when the field variable is velocity potential, the boundary condition (continuity of pressure) leads to the inverse density ratio $\frac{1}{m}$ in the potential field which cancels out the original density-ratio factor.

2.3 Total Field for a Point in a Planar Layered Medium

Now we have an approximate form for the spherical wave after refraction at a planar interface.

We attempt to obtain the aperture equation by modifying the Raleigh integral in Equation 2.3 for the homogeneous medium case.

We substitute the pure spherical wave $\frac{\exp(-jkr_{am})}{r_{am}}$ in the Raleigh integral in Equation 2.3 (for the homogeneous medium case), by the $G(P_m)$, (derived in Equation 2.16), to obtain the response at a medium under one planar layer.

$$\Phi(P_m) = \int_{P_a}\int A(P_a, \theta, n) u_z(P_a) \exp(jk_1 L_1 + jk_2 L_2) dS \qquad (2.18)$$

For $n = 1$, the amplitude is $A(P_a, \theta, n) = \frac{1}{r_{am}}$, (the expected inverse of the radial distance between point "a" in the aperture and point "m" in the medium, for a spherical wave) and Equation 2.18 reduces to the equation for the aperture in a rigid-baffle.

So far we have equations to derive the response inside a medium with an intermediate planar layer. The interface is parallel to the aperture. In the next chapter we derive similar aperture equations for a more general case where we have multiple layers and the interfaces need not be parallel or planar. We assume that the interface can be broken into small planar segments.

Chapter 3

Ultrasound Propagation in Multi-Skewed-Layered Medium

In this chapter we derive a closed form function modeling the ultrasound field propagating through layered media under ray-tracing approximations. We note that numerical evaluation of this function has been done before [1]. However, we are motivated by the fact that closed-form modeling is accurate as well as more amenable to numerical inversion techniques.

The next section summarizes the assumptions under which we derive the field.

In the next two sections, we present a closed form equation for the field for propagation through 3-layered lossless media and extend it to multiple media. In Section 3.4 we consider absorption and backscattering losses. In the last section, Section 3.5 we write full response equation inside the multi-layered medium for broad band pulses.

3.1 Model Assumptions

The derivation presented here is for longitudinal propagation only. It has certain assumptions. First is that each of the layers are homogeneous within themselves. The second assumption is that ray-acoustics approximation is valid for the relative dimensions of the layers considered and the wavelength used. The third assumption is that interfaces separating the media are locally planar (to the order of the wavelength used). The derivation in the next section assumes lossless media. However, we incorporated absorption and backscattering loss in a later section, following [1, 5]. We also do not consider multiple reflections with the assumption that the path-lengths are large for most of these cases and the echoes would be attenuated.

3.2 Derivation of Field in a three-layered medium for an incident spherical wave

In this section we derive the propagation equations through three layers. We generalized to multiple layers later.

In Figure 3.1 we show an aperture which is idealized to be composed of point sources, emitting spherical waves into the first medium in contact. We consider monochromatic excitation for now. We consider what happens to

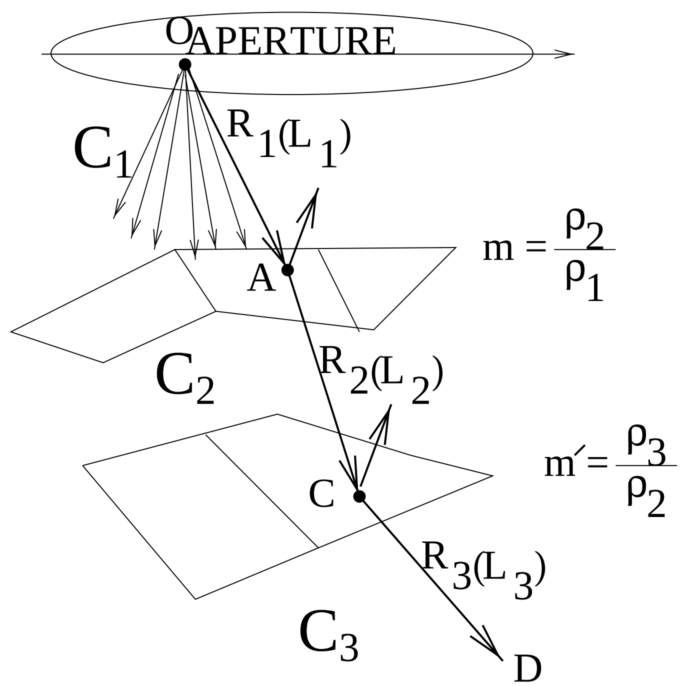

Figure 3.1: **Ultrasound Rays Through Three Layers**

the monochromatic spherical wave emitted by each of these point sources when propagating through 3-layered medium. We take the velocity potential as the variable of interest. However a similar relation is valid for other variables such as pressure.

A spherical wave can be thought of an infinite sum of plane waves (Equations 26.17 (or 26.19) in [2]). When we adopt ray-tracing approximations, we assume each spherical wave can be approximated by a cone of rays. Each ray approximate the contribution of the component plane wave in the direction of the ray. And the boundary conditions that were applicable to the component plane wave can be applied to the ray [2].

In Figure 3.1 we trace a ray passing through Medium 1, 2, 3, with acoustic propagation velocities C_1, C_2 and C_3 (and densities ρ_1, ρ_2 and ρ_3) respectively. The ray is partly reflected and partly transmitted at every interface. In Figure 3.1 the different sections of rays in the different media are denoted by vectors $\mathbf{R_1}$, $\mathbf{R_2}$, ... etc. The corresponding lengths of the rays are (denoted in brackets), L_1, L_2, ... etc.

The emitted wave from the point source O is a spherical wave of the form $\frac{\exp(j(2\pi f)R)}{R}$, where R is the radial length and f is the frequency of the monochromatic wave. After propagating through the layers, the waveform is no longer spherical, due to refraction. The range spreading factor as well as phase factor changes. Our aim is to calculate the amplitude and phase at an arbitrary point D inside the third-medium.

Under ray-tracing approximation, the phase is derived simply the time delay from point O to D [2, 3]. The total time delay is $\frac{L_1}{C_1} + \frac{L_2}{C_2} + \frac{L_3}{C_3}$. The phase factor is,

$$\Phi = \exp[j(2\pi f)(\frac{L_1}{C_1} + \frac{L_2}{C_2} + \frac{L_3}{C_3})] \tag{3.1}$$

We need to derive the amplitude at point D. Following the approach taken in [2, 3] (where planar layers were analyzed), at the boundary of successive layers, we apply boundary conditions (continuity of pressure) to obtain the relationship between the field just below and just above the interface. Within each medium we take into account the attenuation due to "spreading of the wave". A main point of difference from the analysis in [2, 3] is that for a general medium, we can not take advantage of the symmetry that is available in case of the planar layers when calculating the spreading factors. In [2, 3] annular-zones could be taken instead of triangular areas, making the analysis somewhat simpler. In our case, we take each ray and find the differential rays analytically in two directions and form flux-tube areas. Then we derive the ratios of differential flux-tube areas to obtain the spreading factor.

To eventually calculate the field at D, we have to calculate the field at each intermediate boundary points, A and C.

The incident field at A is still an undistorted spherical wave with amplitude of $\frac{1}{L_1}$. A fraction of this wave is reflected and another factor is transmitted through A. The amplitude of the reflected wave is

$$|f_{Ar}|_{above} = \frac{V(\theta)}{L_1} \tag{3.2}$$

where $V(\theta)$ is the reflection coefficient given by

$$V(\theta) = \frac{m\cos\theta - \sqrt{n^2 - \sin^2\theta}}{m\cos\theta + \sqrt{n^2 - \sin^2\theta}} \tag{3.3}$$

where θ is the angle of incidence at the first interface (that is, angle between $\mathbf{R_1}$ and normal $\mathbf{n_1}$), $m = \frac{\rho_2}{\rho_1}$ (that is the density ratio of second-medium to the first), $n = \frac{C_1}{C_2}$ is the refractive index, the velocity ratio of the first-medium to that in the second-medium.

This Equation 3.2 and 3.3 follows by applying the continuity of pressure condition to obtain the reflected wave (shown in [2, 3]).

The field just above A is the sum of the incident (spherical) wave and the reflected wave [2]. Hence, the field, above the point A is given by,

$$|f_A|_{above} = \frac{|1 + V(\theta)|}{L_1} \tag{3.4}$$

To find the field just below A (after refraction), we again apply the boundary conditions of continuity of pressure. Then, the velocity potential field is just $\frac{1}{m}$ times the field above A, [2] [1].

$$|f_A|_{below} = \frac{|1 + V(\theta)|}{mL_1} \tag{3.5}$$

To obtain the field at C (inside the second medium) we have to consider the attenuation due to spreading between A and C. We denote this factor as S_{f_2} and derive it later. Hence the *incident* field just above the boundary at C is,

$$|f_C|_{inc} = |f_A|_{below} S_{f_2} \tag{3.6}$$

[1]Note that this density factor would have been missing if the field of interest was pressure

But again part of the incident wave is reflected at C. The total field just above the point C is sum of the reflected and the refracted wave [2].

$$|f_C|_{above} = (1 + V^{'}(\theta_t))|f_C|_{inc} \tag{3.7}$$

And finally, to obtain the field just below C, we apply the boundary condition again,

$$|f_C|_{below} \quad = \quad |f_C|_{above}\frac{1}{m'} \tag{3.8}$$

where, $m^{'} = \frac{\rho_3}{\rho_2}$ and

$$V^{'}(\theta_t) = \frac{m' \cos\theta_t - \sqrt{n'^2 - \sin^2\theta_t}}{m' \cos\theta_t + \sqrt{n'^2 - \sin^2\theta_t}} \tag{3.9}$$

Here θ_t is the angle of incidence at second interface (that is, angle between $\mathbf{R_2}$ and normal $\mathbf{n_2}$) and $n^{'} = \frac{C_2}{C_3}$ is the relative refractive index between Medium 2 and Medium 3.

Combining Equations 3.8, 3.7, 3.6, and 3.5, we arrive at,

$$|f_C|_{below} \quad = \quad \frac{|1 + V(\theta)|}{mL_1}\frac{1 + V^{'}(\theta_t)}{m'}S_{f_2} \tag{3.10}$$

Finally going from C to D, we have to consider the spread-factor S_{f_3}.

The amplitude of the field at D, is therefore,

$$|f_D| = \frac{|1 + V(\theta)|}{m}\frac{|1 + V^{'}(\theta_t)|}{m'}\frac{1}{L_1}S_{f_2}S_{f_3} \tag{3.11}$$

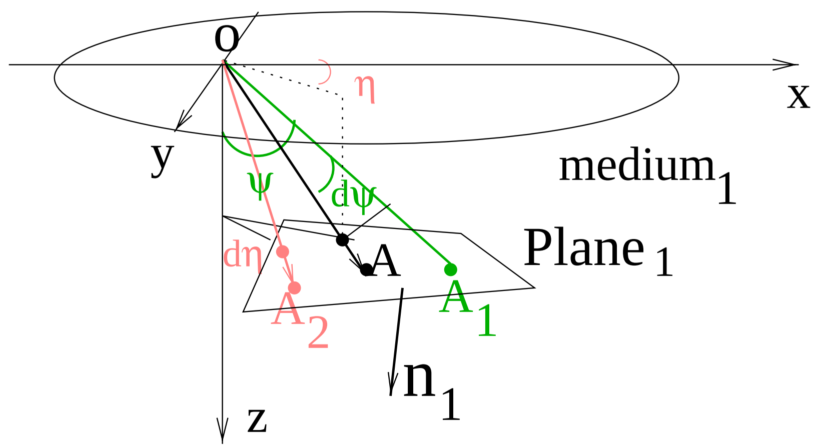

Figure 3.2: **Considering Differential Rays in Two Directions**

In writing Equation 3.11 we have regrouped the terms, so that we have the boundary factors, B_{f_1} and B_{f_2} at two interfaces, and the spreading factors in each of the medium, S_{f_1} and S_{f_2} and S_{f_3} grouped together.

The boundary factors, are $B_{f_1} = \frac{|1+V(\theta)|}{m}$ and $B_{f_2} = \frac{|1+V'(\theta_t)|}{m'}$.

Only one of the spreading factors is known at this point, $S_{f_1} = \frac{1}{L_1}$ (in the first medium, the incident wave being spherical, the spreading factor is simply the inverse radial distance).

We calculate the product $S_{f_2}S_{f_3}$ next.

To calculate the spreading factors in second and third medium, we compose a differential "flux-tube" composed of three rays - the ray in consideration and two other rays obtained by shifting differentially from this ray, as shown in Figure 3.2.

In absence of absorption or viscosity loss, energy is conserved across flux tube areas perpendicular to the ray. The area, perpendicular to the ray locally signifies the wavefront. The spreading factor, is given by the square-root of the inverse ratio of the flux-tube cross-sectional areas [2, 3].

The co-ordinate system we consider is shown in Figure 3.2. The plane of the aperture is the x-y plane and z-axis is downward into the media. The origin is shifted to the source point we consider. We define the ray in spherical-coordinates. ψ is the angle the ray makes with the z-axis and η is the angle that the projection makes with the x-axis. The flux-tube we construct is illustrated in Figure 3.2. To form the flux-tube, a second ray is taken by perturbing the ray slightly to another angle $\psi + \mathrm{d}\psi$ (keeping η fixed). The origin is the same. We call this the $\mathrm{d}\psi$-ray hence forward. Similarly, the third ray is obtained by perturbing the ray by an angle $\mathrm{d}\eta$ (keeping ψ fixed). We call this the $\mathrm{d}\eta$-ray hence forward. The primary ray, is called the main-ray from now on.

Figure 3.3 shows the three-rays undergoing refraction at the two interfaces. The shaded triangles AA_1A_2 and CC_1C_2 are the vertices of intersection of the rays with the (locally planar) interfaces. Note that these are differential areas.

To obtain the spreading factors, we need the triangles which are orthogonal to the rays. Referring to Figure 3.3, Δaa_2A_1 is formed where the plane perpendicular to the main ray $\mathbf{R_2}$ (in the second medium) intersects the $\mathrm{d}\psi$-ray (at A_1) and the $\mathrm{d}\eta$-ray (at a_2). Since we can ignore lengths of second order of differentials (that is of form $\mathrm{d}l\mathrm{d}\theta$ in comparison to lengths of $\mathrm{d}l$), the triangle, Δaa_2A_1 is a projection of ΔAA_1A_2 on to the plane perpendicular to $\mathbf{R_2}$ at A. [2].

[2]Note that the projection would have been exact if the vector $\mathbf{A_2a_2}$ had been parallel

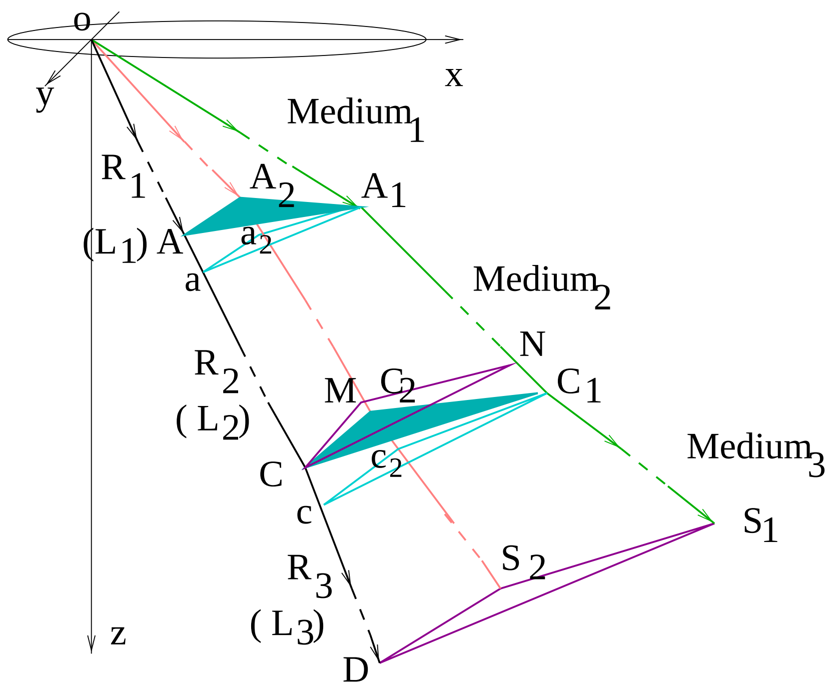

Figure 3.3: **Areas of Energy Conservation**

Δaa_2A_1 is crossectional-area of the the flux tube formed by the three rays just under A.

Similarly, at point C, referring to Figure 3.3, the cross-sectional area of the flux tube is given by $Area\Delta CMN$ (area perpendicular to $\mathbf{R_2}$ at C).

Hence, the spreading attenuation is in medium 2 (between point A and point C) is,

$$S_{f_2} = \sqrt{\frac{Area\Delta aa_2A_1}{Area\Delta CMN}} \tag{3.12}$$

The spreading factor inside medium 3, between point C and D is, from Figure 3.3,

$$S_{f_3} = \sqrt{\frac{Area\Delta cc_2C_1}{Area\Delta DS_2S}} \tag{3.13}$$

Before, trying to evaluate these areas, we make a further simplification when considering the product of the spreading factors $S_{f_2}S_{f_3}$, We refer to Figure 3.4. This shows the two cross-sectional triangles just above and just below the point C.

$Area\Delta CMN$ is the projection of $Area\Delta CC_2C_1$ onto a plane perpendicular to ray $\mathbf{R_2}$ and $Area\Delta cc_2C_1$ is the projection of $Area\Delta CC_2C_1$ onto

---

to $\mathbf{Aa}$. But we can show that the difference is negligible. Let us consider a point $a_2{}'$ on the plane perpendicular to $\mathbf{R_2}$, such that $\mathbf{A_2a_2}'$ is parallel to $\mathbf{Aa}$. This would be the exact projection of A_2 on to this plane. The difference between $a_2{}'$ and a_2 is given by the arc swept by A_2a_2 in going through a differential angle (the angular difference between $\mathbf{R_2}$ and its dη-ray counterpart). Since A_2a_2 is by itself of differential length, the arc is therefore of second order differential, of negligible dimensions. That is, a_2 and $a_2{}'$ are virtually coincident in this differential world.

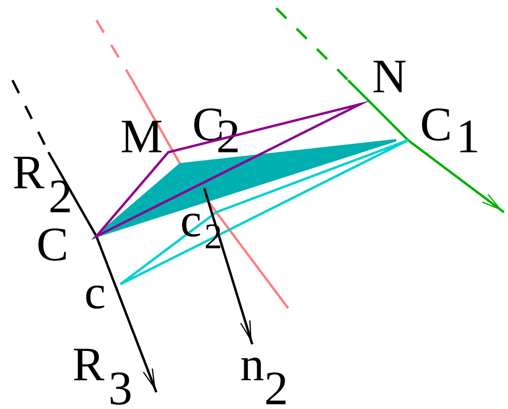

Figure 3.4: **Projections of Area**

a plane perpendicular to ray $\mathbf{R_3}$. Hence, by laws of orthogonal projection, $Area\Delta CMN = \cos\theta_t Area\Delta CC_2C_1$ and $Area\Delta cc_2C_1 = \cos{\theta_t}' Area\Delta CC_2C_1$, where θ_t is the angle of incidence (angle between $\mathbf{n_2}$ and $\mathbf{R_2}$) and ${\theta_t}'$ is the angle of refraction at the interface (angle between $\mathbf{n_2}$ and $\mathbf{R_3}$).

Hence, we can write

$$\begin{aligned} S_{f_2}S_{f_3} &= \sqrt{\frac{Area\Delta aa_2A_1}{Area\Delta CMN}}\sqrt{\frac{Area\Delta cc_2C_1}{Area\Delta DS_2S_1}} \\ &= \sqrt{\frac{Area\Delta aa_2A_1}{Area\Delta DS_2S_1}}\sqrt{\frac{\cos\theta_t'}{\cos\theta_t}} \end{aligned} \tag{3.14}$$

We have to therefore derive only the last (ΔDS_2S_1) and the first (Δaa_2A_1) areas.

To derive the areas, we derive the sides of the triangles. The derivation is elaborate and given in Appendix A.

To briefly outline the proof we derive the equations of the rays and find the points of intersections of rays and the planes. Then we differentiate the equations for the points of intersections to arrive at the sides of the shaded triangles formed by the points of intersections (shaded triangles in Figure 3.3). From these sides and ray directions and lengths, we can arrive at the sides of the unshaded triangles.

First consider the sides of the triangle $\Delta a a_2 A_1$ in Figure 3.3. In order to derive these, we derive the sides of the triangle $\Delta A A_2 A_1$, the intersected triangle first. This triangle is formed by the main-ray, dψ-ray and the dη-ray intersecting the first planar segment. The sides of the triangle $\Delta A A_2 A_1$ are then derived by differentiating the equation of point of intersection A of the plane and the ray, with respect to ψ and η. We can then derive the sides of the triangle $\Delta a a_2 A_1$ from those of $\Delta A A_2 A_1$ and $\mathbf{R_2}$. The details of the derivation of $\mathbf{aA_1}$ is given in Appendix A.

The final expression for $\mathbf{aA_1}$ is,

$$\begin{aligned} \mathbf{aA_1} &= L_1 d\psi[\hat{\mathbf{x}}_{\mathbf{1}\psi} - \frac{(\mathbf{n_1} \cdot \hat{\mathbf{x}}_{\mathbf{1}\psi})}{(\mathbf{n_1} \cdot \hat{\mathbf{R}}_\mathbf{1})}\hat{\mathbf{R}}_\mathbf{1} \\ &\quad -((\hat{\mathbf{x}}_{\mathbf{1}\psi} \cdot \hat{\mathbf{R}}_\mathbf{2}) - \frac{(\mathbf{n_1} \cdot \hat{\mathbf{x}}_{\mathbf{1}\psi})(\hat{\mathbf{R}}_\mathbf{1} \cdot \hat{\mathbf{R}}_\mathbf{2})}{(\mathbf{n_1} \cdot \hat{\mathbf{R}}_\mathbf{1})})\hat{\mathbf{R}}_\mathbf{2}] \end{aligned} \tag{3.15}$$

where $\hat{\mathbf{R}}_\mathbf{1}$ and $\hat{\mathbf{R}}_\mathbf{2}$ are the unit ray vectors, $\hat{\mathbf{x}}_{\mathbf{1}\psi}$ is the derivative of $\hat{\mathbf{R}}_\mathbf{1}$ with respect to ψ, given in Equation A.6, $\mathbf{n_1}$ is the normal to the first interface and L_1 is the intercept of the ray $\hat{\mathbf{R}}_\mathbf{1}$ in the first medium.

The other side, $\mathbf{aa_2}$ can be derived in a similar way. The final result is shown in Equation A.43, repeated below.

$$\mathbf{aa_2} = L_1 d\eta[\hat{\mathbf{x}}_{\mathbf{1}\eta} - \frac{(\mathbf{n_1} \cdot \hat{\mathbf{x}}_{\mathbf{1}\eta})}{(\mathbf{n_1} \cdot \hat{\mathbf{R}}_\mathbf{1})}\hat{\mathbf{R}}_\mathbf{1}$$

$$-((\hat{\mathbf{x}}_{\mathbf{1}\eta} \cdot \hat{\mathbf{R}}_{\mathbf{2}}) - \frac{(\mathbf{n_1} \cdot \hat{\mathbf{x}}_{\mathbf{1}\eta})(\hat{\mathbf{R}}_{\mathbf{1}} \cdot \hat{\mathbf{R}}_{\mathbf{2}})}{(\mathbf{n_1} \cdot \hat{\mathbf{R}}_{1})})\hat{\mathbf{R}}_{\mathbf{2}}] \tag{3.16}$$

where vector $\hat{\mathbf{x}}_{\mathbf{1}\eta}$ is the direction of the derivative of the $\hat{\mathbf{R}}_{\mathbf{1}}$ (with respect to η) as shown in Equation A.41.

Then, the area Δaa_2A_1 is the magnitude of the crossproducts of these two vectors,

$$Area\Delta aa_2A_1 = |\mathbf{aA_1} \times \mathbf{aa_2}| \tag{3.17}$$

Note there is factor L_1^2 in this cross-product. Under the square root, of Equation 3.14, this would result in a factor of L_1 to cancel with the $1/L_1$ in Equation 3.11.

The measure $d\psi d\eta$ in this cross-product gets cancelled with the same ratio in the area in the denominator of Equation 3.14.

The denominator, area of triangle ΔDS_2S_1 can be derived from sides of the triangle ΔCC_2C_1 and the additional "arcs" swept by the length L_3, in bending of the unit ray $\hat{\mathbf{R}}_{\mathbf{3}}$ in two directions (Figure 3.5).

The expression for $\mathbf{DS_1}$ can be obtained from Equation A.32 (after substituting the terms from Equation A.30 and A.34) in Appendix A.

$$\mathbf{DS_1} \quad = \quad \delta_\psi \mathbf{P_C} - (\hat{\mathbf{R}}_{\mathbf{3}} \cdot \delta_\psi \mathbf{P_C})\hat{\mathbf{R}}_{\mathbf{3}} + L_3(\delta_\psi \hat{\mathbf{R}}_{\mathbf{3}}) \tag{3.18}$$

where $\delta_\psi \mathbf{P_C}$ and $\delta_\psi \hat{\mathbf{R}}_{\mathbf{3}}$ are given as

$$\delta_\psi \mathbf{P_C} \quad = \quad (d\psi)[L_1(\hat{\mathbf{x}}_{\mathbf{1}\psi} - \frac{(\mathbf{n_1} \cdot \hat{\mathbf{x}}_{\mathbf{1}\psi})}{(\mathbf{n_1} \cdot \hat{\mathbf{R}}_{1})}\hat{\mathbf{R}}_{\mathbf{1}})$$

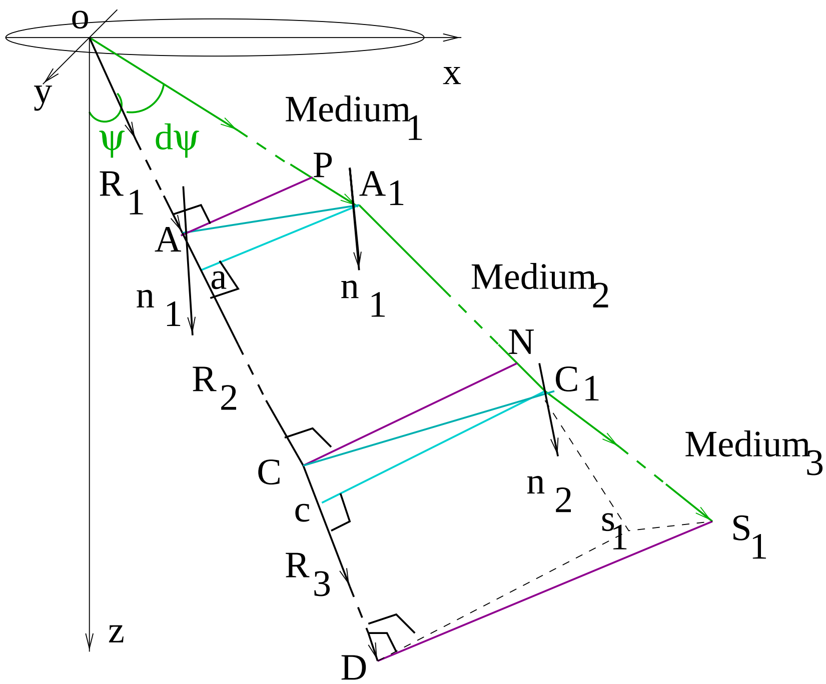

Figure 3.5: **Calculation of Differential Vectors**

$$-L_1\hat{\mathbf{R}}_\mathbf{2}(\frac{(\mathbf{n_2}\cdot\hat{\mathbf{x}}_{\mathbf{1}\psi})(\mathbf{n_1}\cdot\hat{\mathbf{R}}_\mathbf{1})-(\mathbf{n_1}\cdot\hat{\mathbf{x}}_{\mathbf{1}\psi})(\mathbf{n_2}\cdot\hat{\mathbf{R}}_\mathbf{1}))}{(\mathbf{n_1}\cdot\hat{\mathbf{R}}_\mathbf{1})(\mathbf{n_2}\cdot\hat{\mathbf{R}}_\mathbf{2})})$$
$$+L_2\hat{\mathbf{x}}_{\mathbf{2}\psi}-L_2\hat{\mathbf{R}}_\mathbf{2}\frac{(\mathbf{n_2}\cdot\hat{\mathbf{x}}_{\mathbf{2}\psi})}{(\mathbf{n_2}\cdot\hat{\mathbf{R}}_\mathbf{2})}] \quad (3.19)$$

and

$$\delta_\psi\hat{\mathbf{R}}_\mathbf{3} = \frac{d\psi}{n'}[\hat{\mathbf{x}}_{\mathbf{2}\psi}-\mathbf{n_2}(1-\frac{\tan\theta_t{}'}{\tan\theta_t})(\mathbf{n_2}\cdot\hat{\mathbf{x}}_{\mathbf{2}\psi})] \quad (3.20)$$

where $\hat{\mathbf{x}}_{\mathbf{1}\psi}$ and $\hat{\mathbf{x}}_{\mathbf{2}\psi}$ are given in Equations A.6, A.26 respectively.

$\mathbf{DS_2}$ can be similarly obtained.

$$\mathbf{DS_2} = \delta_\eta\mathbf{P_C}-(\hat{\mathbf{R}}_\mathbf{3}\cdot\delta_\eta\mathbf{P_C})\hat{\mathbf{R}}_\mathbf{3}+L_3(\delta_\eta\hat{\mathbf{R}}_\mathbf{3}) \quad (3.21)$$

where $\delta_\eta\mathbf{P_C}$ and $\delta_\eta\hat{\mathbf{R}}_\mathbf{3}$ are given in Equations A.48 and A.54.

So, once again, the cross-product gives the area as,

$$Area\Delta DS_2S_1 = |\mathbf{DS_1}\times\mathbf{DS_2}| \quad (3.22)$$

Note that this area has the differential measure $d\psi d\eta$ which gets cancelled with the same measure in Equation 3.17 when we take the ratio of the two, in Equation 3.14.

3.3 Extension to multi-layered medium

We extend the analysis in the last section to the case where there are multiple layers of media.

Again the time-delays encountered in each medium constitute the phase factor. Inside the i-th medium, at the point $\mathbf{D_i}$, the phase is given by,

$$\Phi_i = \exp[j(2\pi f)(\frac{L_1}{C_1} + \frac{L_2}{C_2} + ... + \frac{L_i}{C_i})] \tag{3.23}$$

To obtain the amplitude at the point $\mathbf{D_i}$ at the i-th layer, Equation 3.11 can be extended to

$$|f_{D_i}| = \frac{|1 + V_{12}(\theta_{12})|}{m_{12}} \frac{|1 + V_{23}(\theta_{23})|}{m_{23}} ... \frac{|1 + V_{(i-1)i}(\theta_{(i-1)i})|}{m_{(i-1)i}} \frac{1}{L_1} S_{f_2} S_{f_3} ... S_{f_i} \tag{3.24}$$

The spreading factor $S_{f_2} S_{f_3} ... S_{f_i}$ can be similarly derived as square root of the area of the first and the last triangles with the chain of cosine factors.

Figure 3.6 shows the interface between i-th and the (i-1)-th medium. Just for notational convenience, the interface between medium i and medium $i-1$ is denoted by triangle $\Delta P_i P_{i2} P_{i1}$, while the normal is $n_{(i-1)}$. There is no confusion. For example the interface between Medium 1 and 2, would be called $\Delta P_2 P_{22} P_{21}$, same as $\Delta A A_2 A_1$ in earlier section (Figure 3.3), while it has normal n_1. The rationale behind such nomenclature is that the unshaded triangle just underneath, perpendicular to the ray $\mathbf{R_i}$ would be correspondingly called $p_i p_{i2} P_{i1}$. This is appropriate because it is inside the Medium i and not (i-1). At the point of interest in Medium i, D_i, the area perpendicular to the ray is $D_i s_{i1} S_{i1}$.

Similar to the discussion in the earlier section, we can arrive at the following relation.

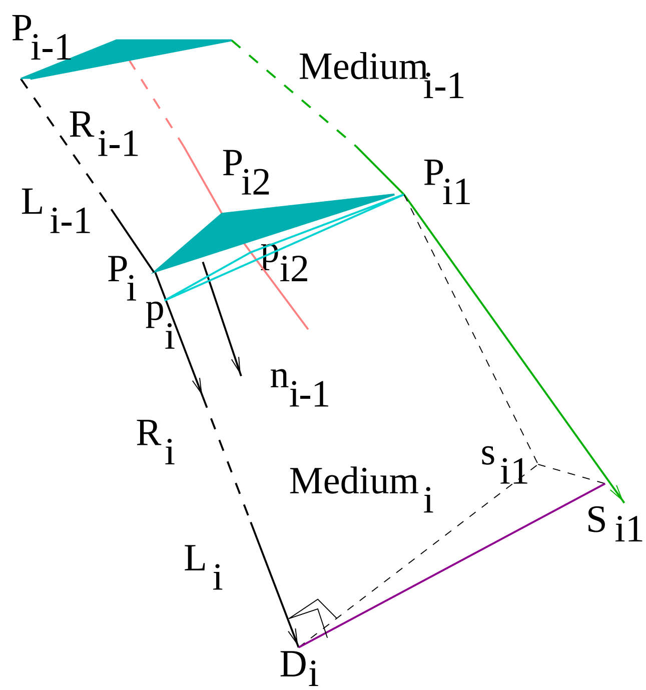

Figure 3.6: **Recursive Relations**

$$S_{f_2}S_{f_3}...S_{f_i} = \sqrt{\frac{\Delta a a_2 A_1}{\Delta D_i s_{i1} S_{i1}}}\sqrt{\frac{\cos\theta'_{23}}{\cos\theta_{23}}\frac{\cos\theta'_{34}}{\cos\theta_{34}}...\frac{\cos\theta'_{(i-1)i}}{\cos\theta_{(i-1)i}}}$$

$$= \sqrt{\frac{\Delta p_2 p_{22} P_{21}}{\Delta D_i s_{i1} S_{i1}}}\sqrt{\frac{\cos\theta'_{23}}{\cos\theta_{23}}\frac{\cos\theta'_{34}}{\cos\theta_{34}}...\frac{\cos\theta'_{(i-1)i}}{\cos\theta_{(i-1)i}}} \qquad (3.25)$$

where $\theta_{(i-1)i}$ and $\theta'_{(i-1)i}$ are the incident and refractive angles at the interface between Medium i-1 and i.

The area at the numerator has been derived already in the last section. We refer to Equation 3.17.

To derive the general area at the point $\mathbf{D_i}$, $\Delta D_i s_{i1} S_{i1}$, we resort to recursive equations. When going through the derivations for three-medium (in the Appendix A) it is evident that many of the vectors and lengths can be arrived at recursively. The generalized recursive extension to multiple layers is given in the Appendix A.

We can use the final result in Equation A.60 to arrive at the two lengths corresponding to the sides of the triangle $\Delta D_i s_{i1} S_{i1}$ as follows,

$$\mathbf{D_i S_{i1}} = \delta_\psi \mathbf{P_i} - (\hat{\mathbf{R}}_\mathbf{i} \cdot \delta_\psi \mathbf{P_i})\hat{\mathbf{R}}_\mathbf{i} + L_i(\delta_\psi \hat{\mathbf{R}}_\mathbf{i}) \qquad (3.26)$$

and

$$\mathbf{D_i s_{i1}} = \delta_\eta \mathbf{P_i} - (\hat{\mathbf{R}}_\mathbf{i} \cdot \delta_\eta \mathbf{P_i})\hat{\mathbf{R}}_\mathbf{i} + L_i(\delta_\eta \hat{\mathbf{R}}_\mathbf{i}) \qquad (3.27)$$

The various components of these equations such as $\delta_\psi \mathbf{P_i}$ can be obtained using the recursive relations derived in Equations A.57-A.59 in Appendix A.

Then, finally the area is given by,

$$Area\Delta D_i s_{i1} S_{i1} = |\mathbf{D_i s_{i1}} \times \mathbf{D_i S_{i1}}| \tag{3.28}$$

Thus we can evaluate Equation 3.25 and substitute in Equation 3.24 to get the field f_{D_i}.

3.4 Losses

In our derivations, we had assumed a loss-less medium. In reality there are energy losses in the propagation of sound. There is loss due to absorption and back-scattering within medium. We can lump these two effects into a bulk attenuation coefficient characteristic of the medium. The attenuation is an exponential function of the product of this coefficient and the path-length traversed in the each medium. Section 2.1.5 has some details on the absorption loss. The attenuation coefficient in general is a function of frequency [18, 1]. The frequency dependence is linear for muscle and is specified in db/cm/MHz. Fat (like water) has very low attenuation coefficient but the frequency dependence is not linear but quadratic. Bone is highly attenuative.

There is another frictional loss - viscosity. However, we can ignore this loss in comparison to other phenomenon for the soft-tissues involved. In this work we ignore this effect.

3.5 Final Propagation Equation: for Broad-band Pulses

So far we have considered monochromatic waves. But ultrasonic transducers emit (broad-band) pulses. We can measure the emitted pulses in advance or can model them by using some model of transducer (such as the KLM model [10]).

The propagation amplitude derived so far is virtually independent of frequency. The refractive index doesn't vary much with frequency because velocity of sound changes only slightly with frequency in the medical range.

But to incorporate the true frequency dependent attenuation across the pulse's bandwidth, we the analyze the response in the frequency domain. The inverse Fourier transform gives the received pulse in time-domain, appropriately distorted by the attenuation coefficient.

The final response at a point D inside a multi-layered medium is,

$$f(P_{D_i}, t) = \int_{P_O} \sum_{rays} |f_{D_i}| (\int_{\omega} e^{-(\mu_1(\omega)L_1 + \ldots + \mu_i(\omega)L_i)} \mathbf{F_p}(\omega) e^{-j\omega(\frac{L_1}{C_1} + \ldots + \frac{L_i}{C_i})} e^{j\omega t} d\omega) dS \tag{3.29}$$

where $|f_{D_i}|$ is given by Equation 3.24. $\mathbf{F_p}(\omega)$ is the transducer pulse (denoted by the suffix $\mathbf{p}$), in the frequency-domain. C_i are the velocities and μ_i are the attenuation coefficients. In Equation 3.29, there are three levels of summation. To evaluate the response at D, we take the cone of rays from each point source P_O; we accumulate the pulses carried by all the rays that reach P_O to the point D ; for each of these rays we calculate the attenuation and phase of the pulse in the frequency domain and transform to the time domain.

We can re-write the Equation 3.29 and take the inverse Fourier integral outside; that is we interfere the pulses carried by each ray in the frequency domain and take the inverse Fourier integral just once on the entire sum.

Note that for a focussed transducer, there is an aperture transmittance. This could be a complex weighting-function, another set of phase-delays applied to the pulse (in addition to the intrinsic propagation phase-delay, $L_1/C_1 + ... + L_i/C_i$).

We can get a simplified equation if we take the attenuation at the center-frequency as a good representation of the attenuation coefficient across the bandwidth. In that case, we can add the pulses undistorted. This is often a good approximation and computationally convenient. In this case, the final equation is given by,

$$f(P_{D_i}, t) = \int_{P_O} \sum_{rays} \exp(-(\mu_1 L_1 + ... + \mu_i L_i)) |f_{D_i}| \mathbf{f_p}(t - (\frac{L_1}{C_1} + ... + \frac{L_i}{C_i})) dS \tag{3.30}$$

where μ_i are the attenuation coefficients in each medium, approximately evaluated at the center-frequency of the pulse $\mathbf{f_p}(t)$. The center-frequency is usually the specified operational or resonance frequency of the transducer.

3.5.1 Pressure as the variable of interest

The analysis this chapter is done assuming that the field variable of interest is the velocity potential.

However, for practical applications, the emitted transducer pulse is usually a pressure pulse and the variable measured by the receiver is pressure. Hence we need to point out the potential changes if the variable of interest is pressure instead of velocity potential.

When the field f denotes pressure, the analysis is identical as done here, expect for the density factors at the boundaries. The boundary condition of pressure being the same above and below gives the straightforward relation $f_{above} = f_{below}$ above and below. This would change Equation 3.5 and 3.8. The only difference this makes is that the final equation for the amplitude factor in Equation 3.11 would not have the $\frac{1}{m}$ density factors. And we would get,

$$|f_D| = |1 + V(\theta)||1 + V^{'}(\theta_t)|\frac{1}{L_1}S_{f_2}S_{f_3} \tag{3.31}$$

Similarly, for multiple layers, the equation becomes,

$$|f_{D_i}| = |1 + V_{12}(\theta_{12})||1 + V_{23}(\theta_{23})|...|1 + V_{(i-1)i}(\theta_{(i-1)i})|\frac{1}{L_1}S_{f_2}S_{f_3}...S_{f_i} \tag{3.32}$$

Chapter 4

Modeling Ultrasound Echoes from a Reflective Interface Under Two-Layers

In this chapter we are interested in modeling the received echoes from a reflective media under two intermediate layers. This case is of special interest to us because it could be an useful tool for tracking the skeletal bone of a patient (through intervening layers of fat and muscle) intra-operatively. A potential application is accurate intra-operative registration with pre-operative CT data.

In this chapter we show that as far as calculating the amplitudes and phases are concerned, this particular case (of reflection under two layers) essentially reduces to the case of propagation through three media and therefore the results arrived at in the last chapter can be used.

4.1 Assumptions

We make the same assumptions as in the last chapter, Section 3.1. We re-iterate the main assumptions here: longitudinal propagation, ray-tracing approximation, and homogeneity within each medium. The ray-tracing approximation means that the dimensions considered (such as thicknesses of layers) are large in comparison to the wavelength.

4.2 Derivation of total response

We model the received echoes from a reflective media under two intermediate layers. This case is of special interest to us because it could be an useful tool for accurately tracking the skeletal bone of a patient (through intervening layers of fat and muscle) intra-operatively. A potential application is accurate intra-operative registration with pre-operative CT data. We show that in this particular case (of reflection under two layers) we can use the results in the last chapter.

Referring to the diagram in Figure 4.1, we want to derive the total response at a point D in the aperture. Ignoring multiple reflections, $f(P_D, t)$ would have two terms, $f_1(P_D, t)$ and $f_2(P_D, t)$. The first term is due to the reflection from the first interface and the second term is due to the reflection from the second interface.

Let us consider the first term, $f_1(P_D, t)$, which is the reflection from the interface between the first and second layer. The ray-paths are those shown in dashed lines in Figure 4.1. The amplitude of this term again consists of

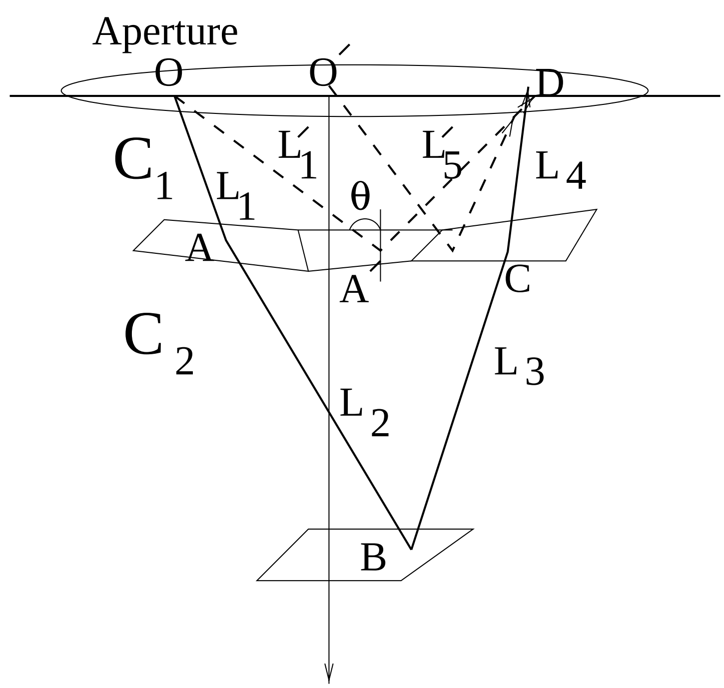

Figure 4.1: **Paths of Pulses Echoed From Two Surfaces**

the boundary terms and the spreading factor. Since this is pure reflection, the boundary factor is the reflection coefficient and the spreading factor is simply $1/r$. Here we assume that the μ_i are the attenuation at the center-frequency, hence we can simply delay and weight the pulses undistorted (as in Equation 3.30).

$$f_1(P_D,t) = \int_{P_O} \sum_{rays'} e^{-(\mu_1(L_1^{'}+L_5^{'}))} \frac{1}{(L_1^{'}+L_5^{'})} V(\theta)\mathbf{f_p}(t-(\frac{(L_1^{'}+L_5^{'})}{C_1}))dS \quad (4.1)$$

where $L_1^{'}$ and $L_5^{'}$ are the path lengths and $V(\theta)$ is the reflection coefficient, given by Equation 3.3, where θ is the angle of incidence of the ray. $rays^{'}$ denote the set of rays that reached from O to D upon reflection at first interface.

The second term is due to the reflection from the second layer. The ray O-A-B-C-D, is the ray to be considered for this term. The segments OA and CD (with path lengths L_1 and L_4) are in the first medium with propagation velocity C_1. AB and BC (of lengths L_2 and L_3) are in the second medium, with propagation velocity C_2.

The second term has the boundary factors at both the interfaces and the spreading factor due to propagation from the source to the point D and also the attenuation due to loss.

The equation for $f_2(P_D,t)$ is written as follows,

$$\begin{aligned} f_2(P_D,t) &= \int_{P_O} \sum e^{-(\mu_1 L_1+\mu_2(L_2+L_3)+\mu_1 L_4)} |f_D| \\ &\quad \mathbf{f_p}(t-(\frac{L_1}{C_1}+\frac{L_2+L_3}{C_2}+\frac{L_4}{C_1}))dS \end{aligned} \quad (4.2)$$

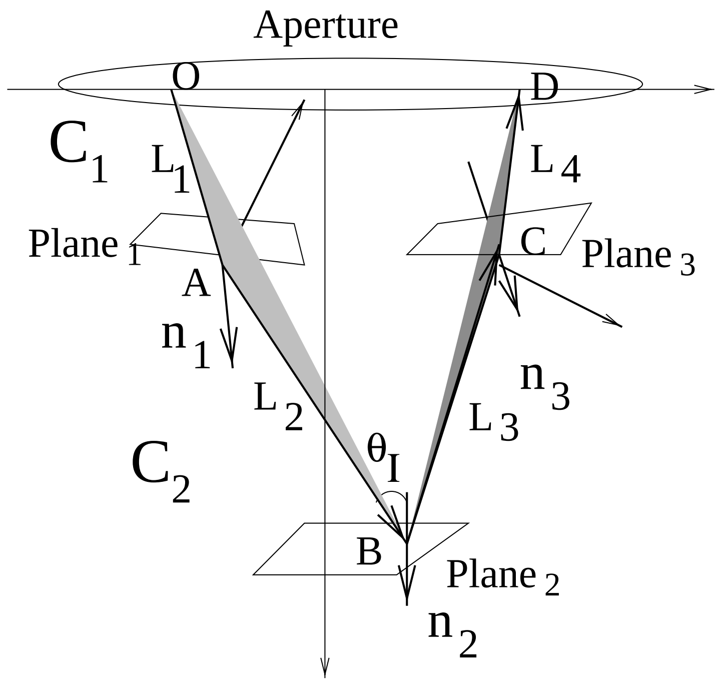

Figure 4.2: **Ray Skeleton For Analysis**

where L_i are the lengths of the path in each media for the ray in Figure 4.1.

In Equation 4.2, the yet-unknown factor $|f_D|$ is the amplitude with the spreading and boundary factors. We show that as far as calculating the spreading factor is concerned, this particular case (of reflection under two layers) essentially reduces to the case of propagation through three media and therefore the results arrived at in the last chapter can be used.

To calculate the factor $|f_D|$, we need to consider just the main skeleton [1]. of rays shown again in Figure 4.2. At a later section (Section 4.2.1) we

[1]We use the term skeleton loosely here to indicate a minimum set of rays tracing the path from the source to the receiver point needed for the particular case under analysis

give the reasons for this. At this point, it suffices to say that when we are considering the boundary conditions at C, we need not consider the incident field at C direct from the source O. That field belongs to another skeleton and is to be considered when we process that. In Figure 4.2, Plane 1 and Plane 3 (the dimensions are exaggerated here for convenience) are polygonal sections of the first interface. Plane 2 is the reflective surface. The normals of these planes are $\mathbf{n_1}$, $\mathbf{n_2}$, $\mathbf{n_3}$ all of which could be in general positions (and not necessary aligned perpendicular to the aperture). The shaded regions indicate that one half (OAB) of the set of rays is in a different plane than the other half (BCD). OA, $\mathbf{n_1}$ and AB are coplanar (by Snell's Law), while BC, $\mathbf{n_3}$ and CD form a different plane.

The incident wave at A (Figure 4.2) is a spherical wave, the outgoing wave is distorted in shape due to refraction. The subsequent reflection at B does not change the waveform further (under ray-tracing approximation). The path ABC is entirely in the second medium. Hence we can reflect ray BC about the Plane 2, and imagine it as a continuation along AB. Then the CD part can also be reflected about Plane 2, but there is a change in the waveform again due to transfer to another medium (medium 1).

The equivalent picture of the skeleton is given in Figure 4.3, where Plane $3'$ is the reflected plane and normal about the plane $\mathbf{n_3'}$ is the normal $\mathbf{n_3}$ reflected about $\mathbf{n_2}$. C' and D' are points C and D, reflected about the Plane 2. We are interested in figuring out the field at the point D', which represents the equivalent point back at the aperture. Note that the length OA and $C'D'$

(in this case, the analysis of the reflected echoes from the second interface).

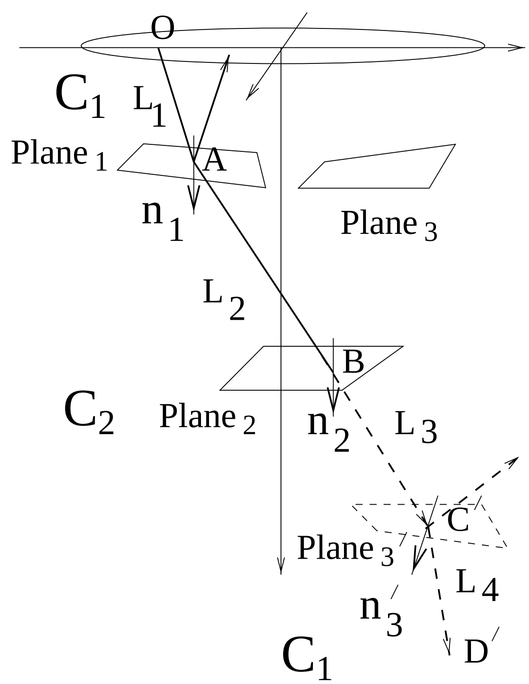

Figure 4.3: **Equivalent Ray Skeleton**

are in first medium here while ABC' is in second.

We see that this is the same three-medium case considered in the last chapter, Figure 3.1, except in this case, Medium 3 is the same as Medium 1. An important difference is that we have an additional factor $R(\theta_I)$ in Equations 3.7 and 3.11 corresponding to the reflection at the second interface (plane B in Figure 4.3). This is a function of the incident angle θ_I. For a perfect reflector, this factor is unity. There are other obvious nomenclature differences, such as $L_2 + L_3$ is the segment of $\mathbf{R_2}$ in the second medium, and was called L_2 in the last chapter.

To summarize, the factor $|f_D|$ in Equation 4.2 is given by Equation 3.11 or Equation 3.24 ($i = 3$) with an additional reflection coefficient (at second interface) term $R(\theta_I)$. We note again, that for the case considered here, the first and third medium are the same, hence density ratio where $m = 1/m^{'}$ [or, $m_{23} = m_{21} = 1/m_{12}$ in Equation 3.24]. Hence effectively the overall density factor is unity. The relative refractive index (velocity ratio) is also, $n_{23} = n_{21} = 1/n_{12}$.

We had noted in the last chapter that, when our variable of interest is pressure, we donot have the density factors in f_D; we need to take Equation 3.31 instead of Equation 3.11. In this special case of a reflective layer inside two-layers however, since the density ratios get cancelled anyway, because the first and the third media are the same, the equations are the same, whether the field variable is pressure or velocity potential.

We can write the final received signal at any point in the aperture by,

$$
\begin{aligned}
f(P_D, t) &= f_1(t) + f_2(t) \qquad (4.3)\\
&= \int_{P_O} \sum_{rays'} e^{-(\mu_1(L_1^{'}+L_5^{'}))} \frac{1}{(L_1^{'} + L_5^{'})} V(\theta)\mathbf{f_p}[t - (\frac{(L_1^{'} + L_5^{'})}{C_1})]dS\\
&+ \int_{P_O} \sum e^{-(\mu_1 L_1 + \mu_2(L_2+L_3)+\mu_1 L_4)} |f_D| \mathbf{f_p}[t - (\frac{L_1}{C_1} + \frac{L_2 + L_3}{C_2} + \frac{L_4}{C_1})]dS \qquad (4.4)
\end{aligned}
$$

The Equation 4.4 suggests we have to accumulate and add (interfere) all the pulses arriving at the point D. This would give the time signal received at each receiver point.

Finally, we can apply the aperture transmittance (such as apply the focusing delays) if any and add the signals for all of these as shown in Figure 4.4.

For the simplest, unfocussed transducer case, we would simply add the response arriving at all the points of the transducer so that the final received time signal is,

$$
f(t) = \frac{1}{Area} \int_{P_D} \int f(P_D, t) dS \qquad (4.5)
$$

where the summation is over the entire aperture. We divide by the total aperture area.

4.2.1 A Note on Independence of Each Ray-skeleton

In this section we explain why we can consider the ray-skeletons shown in Figure 4.2 independently from another.

Here we consider the point C in Figure 4.2, for the explanation, but similar arguments apply to point A as well.

Let us consider the point C and all the waves incident on it from the source O as well as from below, after reflection at the bone. This is shown in Figure 4.5. In this figure the solid lines represent the waves for the skeleton considered in Figure 4.2 while the dotted lines incident wave direct from the source (which starts another skeleton at C). f'_I, f'_R, f'_T denote the incident, reflected, refracted velocity potentials from below, and f_I, f_R, f_T are those from above.

For an incident plane wave, continuity of the pressure and normal component of velocity at a planar interface gives the reflected plane wave (angle of reflection = angle of incidence) and the refracted plane wave (Snell's law) as derived in many books [2, 3] to cite a few. Now for the spherical wave, under ray-tracing approximations, we can apply the boundary conditions ray-by-ray to obtain the reflected, refracted rays, as was done for the analysis in [2]. This is because the ray-tracing approximation essentially means that a component plane wave (at an angle θ) composing the spherical wave is effective only locally, around the ray (at an angle θ). This was discussed in Section 2.2.2.

Now we refer to Figure 4.5. First for each set of waves, f_I, f_R, f_T and f'_I, f'_R, f'_T by themselves have to satisfy the boundary conditions. This can be seen simply as follows. If for example we could block out the incident ray from above, the set of rays f'_I, f'_R, f'_T (shown by the solid-rays) are by themselves and have to satisfy the boundary conditions.

Hence by continuity of pressure condition, we would get, the following two equations, as shown below,

$$\rho_2(f_I + f_R) = \rho_1 f_T \tag{4.6}$$

and,

$$\rho_1(f'_I + f'_R) = \rho_2 f'_T \tag{4.7}$$

Then, we add LHS of Equation 4.6 to RHS of Equation 4.7 and also add RHS of Equation 4.6 to LHS of Equation 4.7, and equate the sums, to get,

$$\rho_2(f_I + f_R + f'_T) = \rho_1(f'_I + f'_R + f_T) \tag{4.8}$$

Which essentially says that for the set of six rays in Figure 4.5, the boundary condition is satisfied, that is the total potential at the top $(f_I + f_R + f'_T)$ is related to the total potential at the bottom $(f'_I + f'_R + f_T)$ with the inverse ratio of the density.

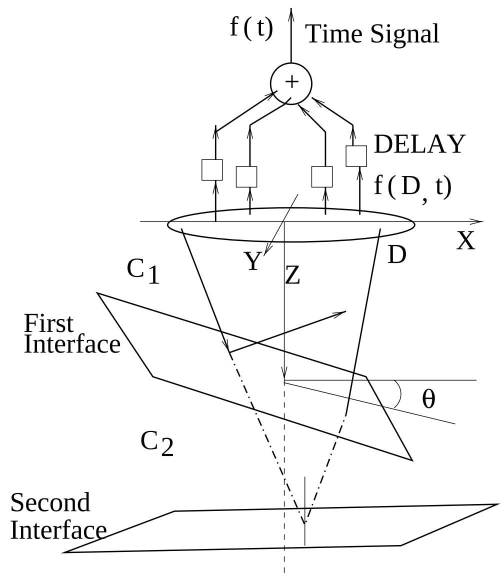

Figure 4.4: Delay and sum the response over the apeture area

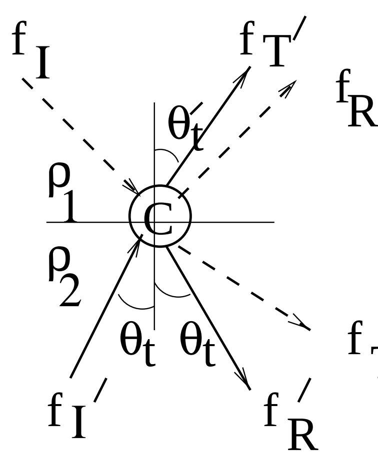

Figure 4.5: **Incident, Reflected and Refracted waves on point C**

Chapter 5

A Computer Simulator of The Model

We built a software simulator for the special case of interest of received echoes from an interface under two layers. We will show the results of simulation and comparison for this type of medium configuration, for a single-element circular aperture transducer.

The simulator can be adapted to simulate the response under 3-layered medium for other apertures (such as linear-arrays) and so on. It can also be extended to accommodate additional layers.

In the first section we describe the simulator inputs, and go through the main steps of the simulation for the particular case of receiving echoes from a reflective interface through two layers.

In the second section we describe an experiment done on tissue-mimicking phantoms for parallel layers.

In the third section we show the simulation parameters (medium and transducer) used for this experimental case and compare results with experiments.

5.1 Computer Simulator

We simulate the $f(t)$ in Equation 4.5 where $f(P_D, t)$ is given by the Equation 4.4.

5.1.1 Simulator Inputs

The input to the simulator are the following:

- Physical parameters of medium: density, velocity and attenuation coefficients.
- Geometrical parameters of medium: number and vertices of triangular segments forming the surfaces in three interfaces.
- Modulated Gaussian Pulse parameters: center modulation frequency, phase, σ, mean, amplitude.
- Sampling frequency and the number of samples of the output (limits the maximum depth of interest).
- Aperture geometry : dimension of aperture and aperture sampling intervals(usually $< \lambda/8$).

5.1.2 Example: Reflective Layer Under Two layers

In particular we are interested in simulating the special case of a two-layered medium on a strong reflector as considered in Chapter 4. We are simulating for a single-element circular aperture transducer. The same element is involved in transmitting and receiving.

We go through the main steps of the simulation as an illustration.

- We digitize the aperture into small elements. Each element should be small enough to be treated as a point source. We should digitize the aperture so that each element is less than $\lambda/8 \times \lambda/8$.

- From each point source we take a solid-cone of rays simulating a spherical wave. We trace the ray through the geometry of the medium. We calculate the ray-segment lengths in each medium and the angles rays makes with the normals of the surface segments.

- For the rays that reach back to an aperture element (this includes the rays that hit the aperture directly from the first interface) we calculate the amplitude and phase of the pulse. We add and accumulate the pulse carried by the ray hitting each aperture point.

- Finally we add up the time signals for all the aperture elements and divide by the number of elements. The final output is a time signal.

5.2 Experiments

We have performed real-life experiments for the special case considered in the last chapter. In this section we describe the experimental equipment, procedure and the experimental results.

5.2.1 Experimental Equipment and Procedure

The ultrasonic transducer used is 7.5 MHz, single element circular aperture transducer. We use a RiTec control box with variable amplitude and frequency to trigger the transducer. We excite the transducer with a short square pulse of time-duration half of the time-period at resonance, (that is, $1/(2 \times 7.5)\mu s$ or about 67 ns). We place the transducer over the fat-phantom and obtain the return-echoes. The echoes are captured, and filtered by a low pass and a high pass filter. The low pass filter is set at 10 MHz. The high pass filter is set at 20 KHz, to remove the DC bias. The filtered signal is sampled at 25 MHz by an Analog to Digital Converter. [1]. A Sonix board is used for this purpose. The buffer length is 4096 samples. The Sonix board is triggered by a synchronizing trigger source from the control box at the exact time of excitation of transducer.

We used “fat” and “muscle” mimicking phantoms. These physical objects (designed from water-agar-gel mixtures) mimic some ultrasound characteristics (such as propagation velocity) in human fat and muscle. We also used a steel-block about 5 cm thick.

[1]Hence the cut-off frequency of lowpass filter at 10 MHz is adequate to avoid aliasing

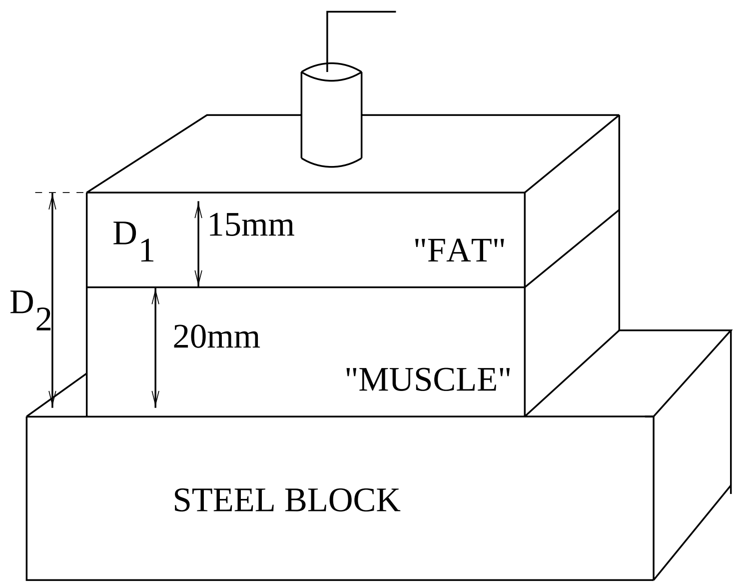

Figure 5.1: Experimental Set Up

The set up is shown schematically in Figure 5.1. We place the phantoms on top of the steel-block and obtain the pulse-echoes from the fat-muscle interface as well as the muscle-steelblock interface. To obtain good coupling between the phantom layers we wet them with water. Then we stack on the steel-block so that the muscle-phantom lies on the steel-block and the fat-phantom on top of the muscle. The purpose is to create a highly reflective interface under two layers (fat and muscle). The values of the media parameters of the phantom provided by the manufacturer is given in Table 5.1. In particular the thicknesses are correct to within a millimeter.

5.2.2 Experimental Data

We show the experimental data here in Figure 5.2.

Experiment

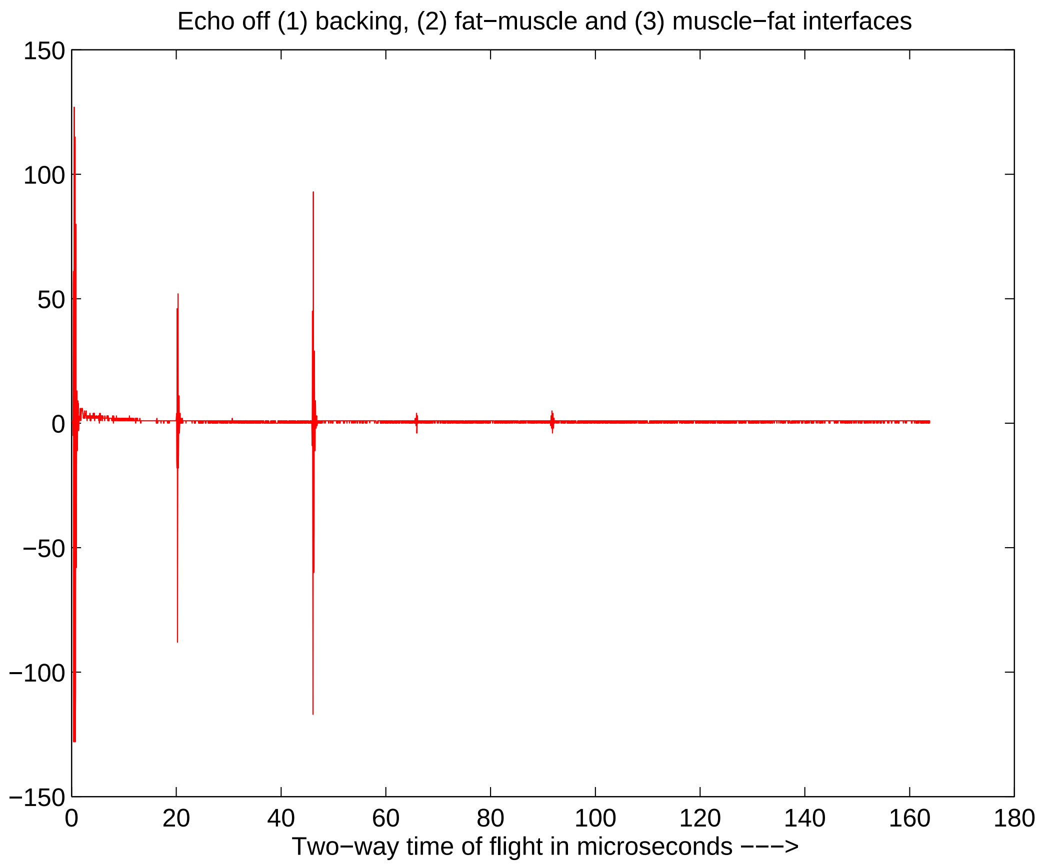

Figure 5.2: **Experiment**: Echo Signals from fat-muscle and muscle-steel interface

Media Parameters Provided		
Parameters	Phantom 1 (fat)	Phantom 2 (muscle)
Relative density (wrt water)	1.010	1.041
Velocity in $mm/\mu s$	$C_1 = 1.508$	$C_2 = 1.582$
Attenuation in $db/cm/MHz$	0.067	0.188
Thickness in mm	15 ± 1	20 ± 1

Table 5.1: **Media Parameters**

In Figure 5.2, the first very high-amplitude echo at the beginning (adjacent to the y-axis, near zero-time) is the echo off the interface between the transducer backing and the fat-phantom. The second echo is that from the fat-muscle interface. The next higher echo is from the muscle and steel-block interface. The last two echoes are shown in close-up in Figures 5.3 and 5.4.

5.3 Simulation and Comparison with Experiment

We got the experimental data. We now simulate the received echoes for the parameters of the controlled experiment. But before doing so, we had to estimate the transducer pulse to be used in the simulator. We first describe the experiment to obtain the transducer pulse. And fit the parameters of the pulse, assuming it is a gaussian. Then we compare the experimentally obtained signal shown in Figures 5.3 and 5.4 in with the simulation, using

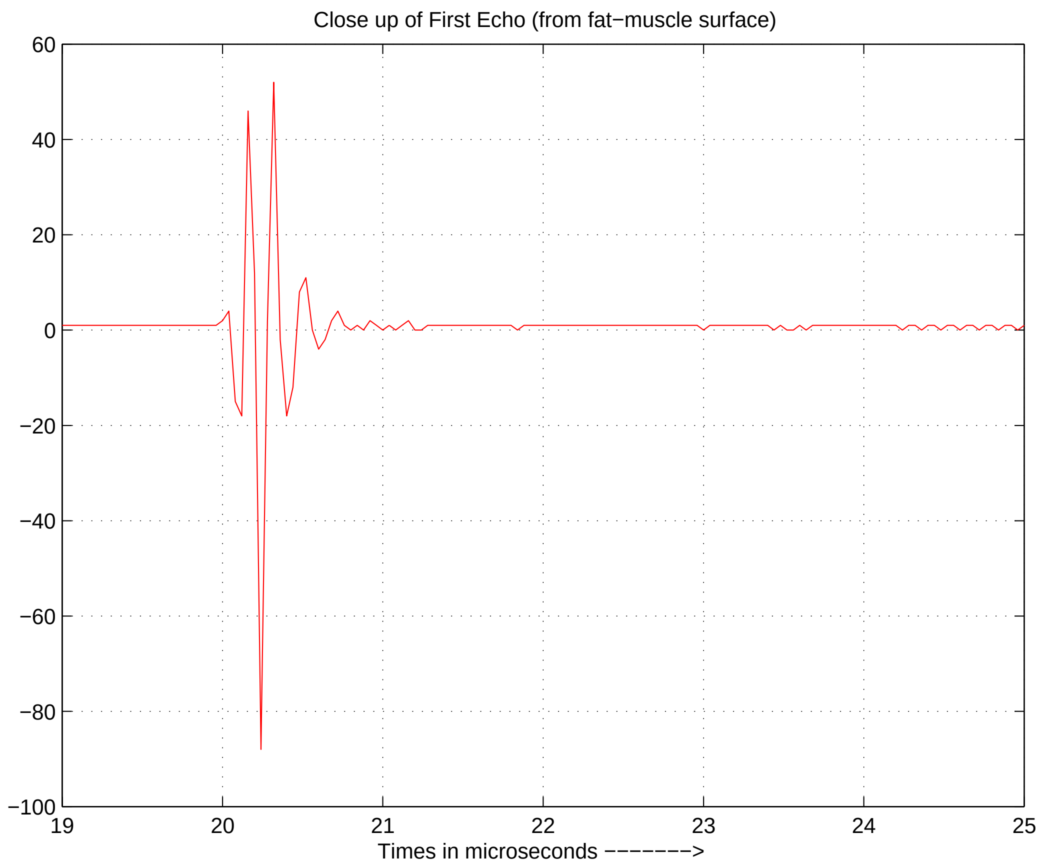

Figure 5.3: **Experiment**: Echo Signal from fat-muscle interface

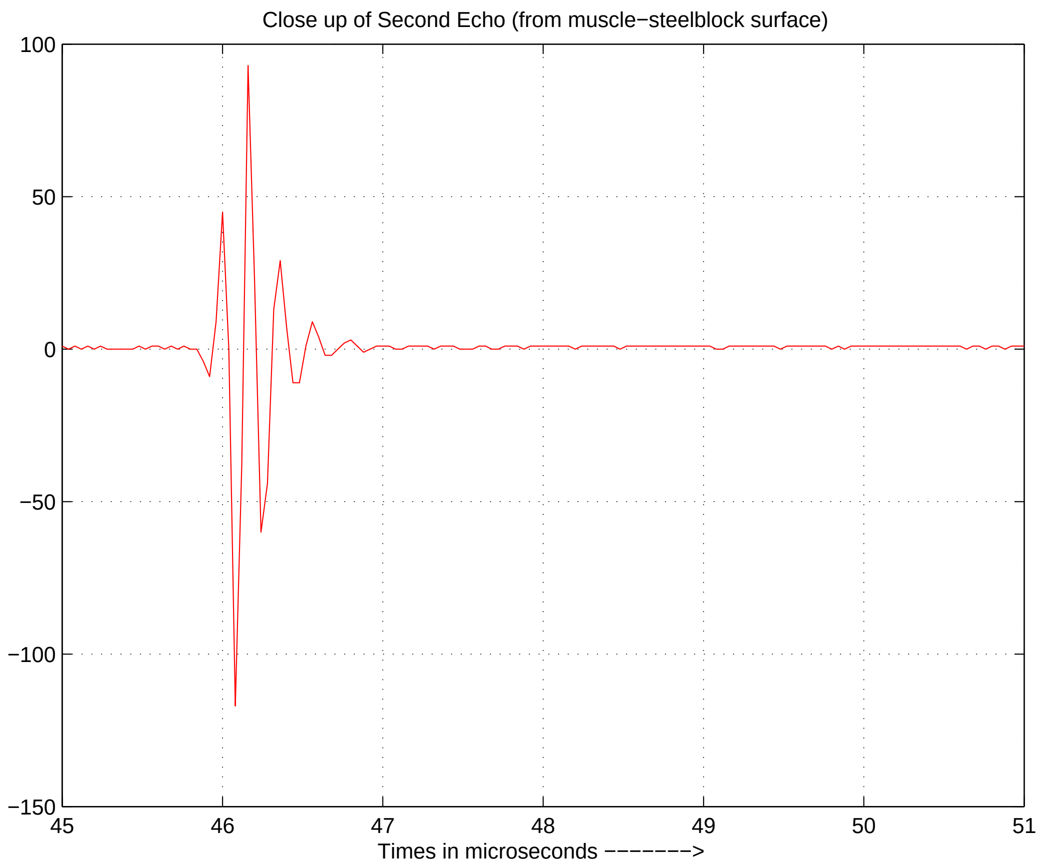

Figure 5.4: **Experiment**: Echo Signal from muscle-steel interface

the nominal values of the thicknesses. However we observed mismatch in the position of the echoes. So we estimated correct parameters and show the simulation results again with the fitted parameters.

5.3.1 Determining the Transducer Pulse

We experimentally determined the pulse for this transducer.

We obtained an echo from the steel-block, under water, placed far away (about 5 cm) from the transducer. This is to make sure that the delays experienced by the emitted-pulse in going through the different ray-paths are all roughly the same. This is true if the distance from the transducer is far enough away in comparison to the aperture diameter and the wavelength[2]. This type of experimental determination of pulse is a standard method to measure the pulse when the transducers are tested by designers [3]. The pulse obtained is observed to be nearly a Gaussian. We fit a Gaussian curve modulated by a sine function at the carrier frequency. We use simplex algorithm to obtain the parameters. The parameters fitted to the Gaussian are amplitude, mean, standard deviation, and the center frequency of modulation and phase of the sine function. In the next section we show the results.

[2]Strictly speaking, this experiment does not just give the pulse emitted from the transducer but that pulse, convolved twice (forward and return) with the transducer (and filter) impulse responses. However, that in fact is necessary. Because all the echoes we are going to subsequently measure by the transducer are also going to be convoluted twice with this impulse-response. Hence, we do need the emitted pulse after twice convolution with the transducer impulse response.

[3]personal communication, Mr. Xue, Advanced Devices.

Table 5.2: **Gaussian Pulse Parameters**

Parameters of the fitted Gaussian	
	Parameters
Amplitude	162.3744
Mean (samples)	9.0017
Sigma (samples)	2.2762
Frequency (MHz)	6.8857
ϕ (radian)	-0.4538

Figure 5.5 shows the pulse we obtained. We maximize the return echo from the steel-block under water, about 5 cm from the 3 mm diameter transducer.

The parameters of the Gaussian fitted to the experimental data are given in Table 5.2.

The frequency of modulation was $6.8857 MHz$, while the transducer is specified to operate at $7.5 MHz$. This discrepancy was guessed to be because of the excitation - we used a square pulse instead of an impulse. To test this hypothesis, we later performed another experiment to determine pulses, this time using the shortest pulse the control box could produce. We set the pulser at 12.82 MHz. We got the pulse and fitted the modulated Gaussian and we obtained the frequency as 7.38 MHz. This was done just as a test. Our experiments with tissue mimicking phantoms were performed with the

Estimating Pulse emitted by transducer

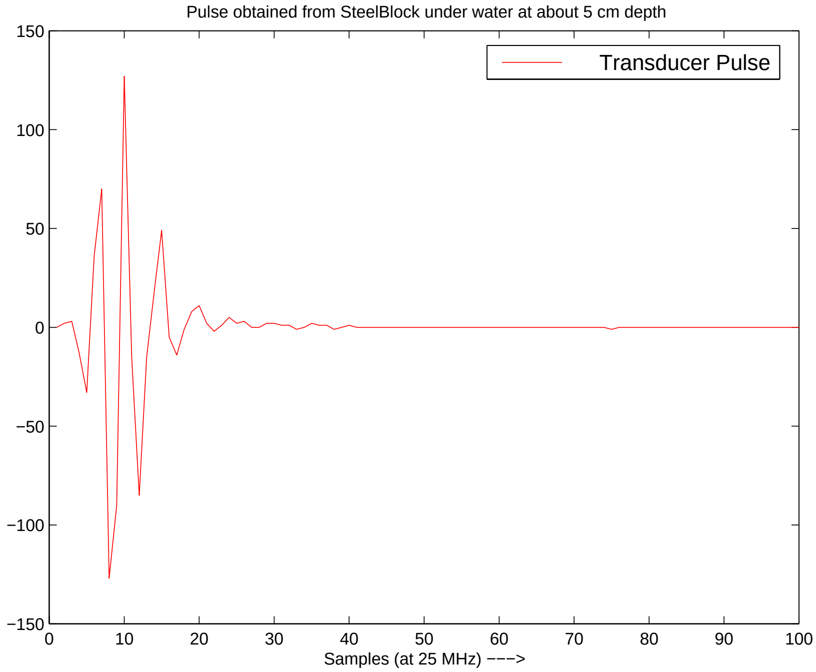

(a) Pulse from Steel-block

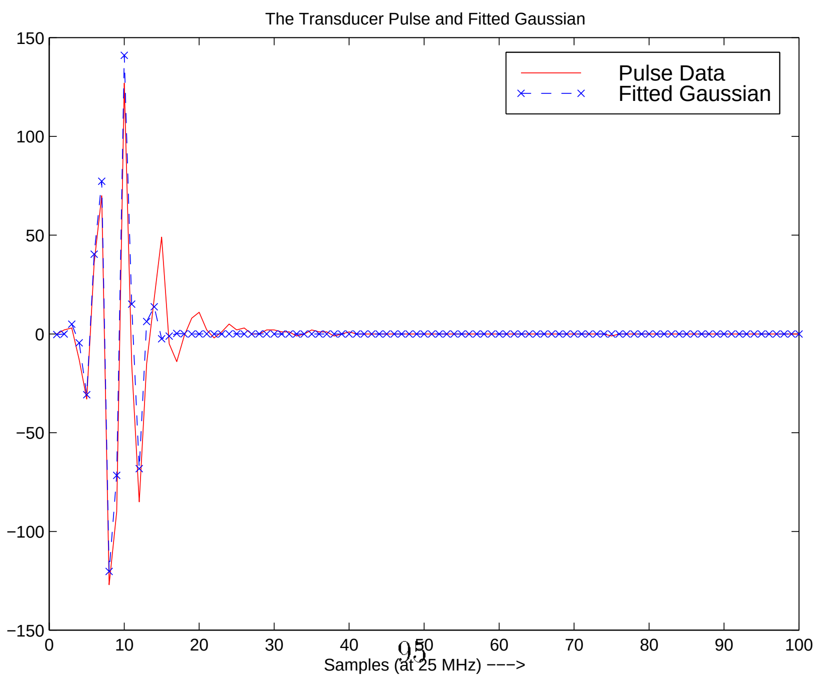

(b) Pulse compared to a best fit Gaussian.

Figure 5.5: **Transducer Pulse and the best fit Gaussian used for simulations**

original excitation giving the pulse at 6.8857 MHz and simulations at the pulse parameters in Table 5.2.

It is noted that the pulse obtained by this experiment give estimates of the transducer-pulse only to a scale. Therefore, we do not know the exact amplitude scaling of the pulse emitted out of the transducer. When comparing simulations and experiments we use a scaling factor given by the relative energy for a start.

There is a shape mismatch with the transducer pulse and the matched gaussian in Figure 5.5. This could to be due to a small amount of attenuation in water which we did not take into account when fitting the gaussian. It is noted that the misfit is more towards the end of the pulse than in the center or beginning.

5.3.2 Using Nominal Medium Parameters

A previous Table 5.2 showed the parameters of the gaussian pulse used as the transducer pulse in our simulations. The Table 5.3 shows the medium parameters used for the simulations. The thicknesses are assumed at the *nominal* value at this point. The phantoms are designed as flat slabs with designated thicknesses. So the geometry of the phantom surfaces are assumed planar and parallel to the aperture for simulation purposes. The same is true for the steel-block surface as well. The steel block is assumed a perfect reflector.

The attenuation (due to loss) parameter is converted to db/cm by multiplying the listed attenuation values with the center frequency of the pulse,

Parameters used in simulations		
Parameters	Phantom 1 (fat)	Phantom 2 (muscle)
Relative density (wrt water)	1.010	1.041
Velocity in $mm/\mu s$	$C_1 = 1.508$	$C_2 = 1.582$
Attenuation in $db/cm/MHz$	0.067	0.188
Thickness in mm	15	20

Table 5.3: **Simulation Parameters**

6.8857 MHz. The attenuation (in db) is obtained by multiplying the individual ray lengths in each medium by the given attenuation factor.

Since we do not know the amplitude scale of the emitted pulse, for purpose of comparison, we have scaled the simulation data by the ratio of the RMS amplitude of the experimental data to that of the simulated data. In order to get this scaling ratio, we remove the first big echo (near zero) from the experimental data in Figure 5.2.

The Figures 5.6-5.8 show the first experimental results (solid lines) and the simulation (dashed lines).

The plot in Figure 5.6 shows the echoes off the fat-muscle and the muscle-steelblock interfaces. The solid-lined plot shows the experiments and the dashed-line plot shows the simulations.

The Figures 5.7 and 5.8 show the echoes close-up. We see that the echoes have not matched exactly in position. There are small delay-errors (in fractions of mm), of the echoes. The reason for this is that we know the thick-

Comparison of Experiment with Simulation

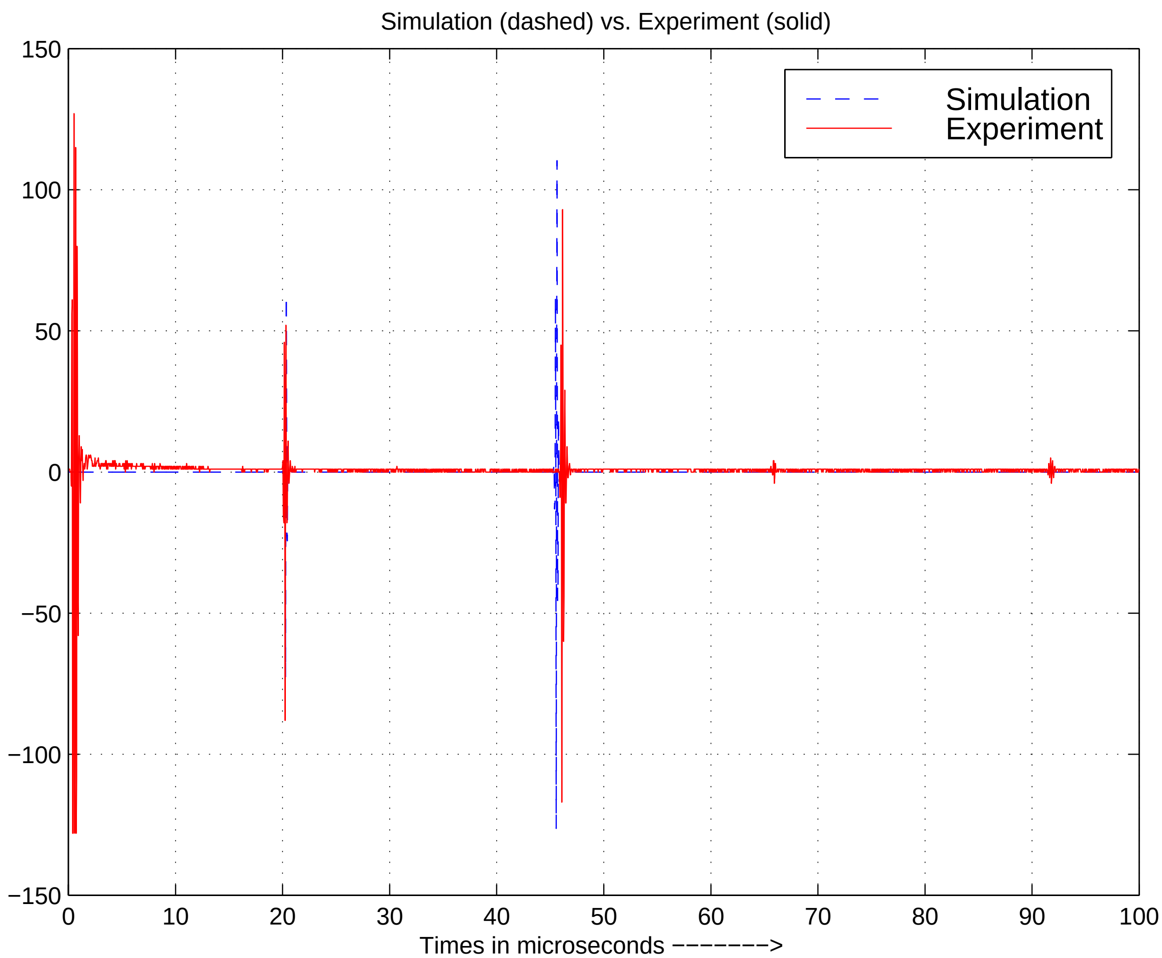

Figure 5.6: Comparison of Experiment and Simulation

Comparison of Experiment with Simulation

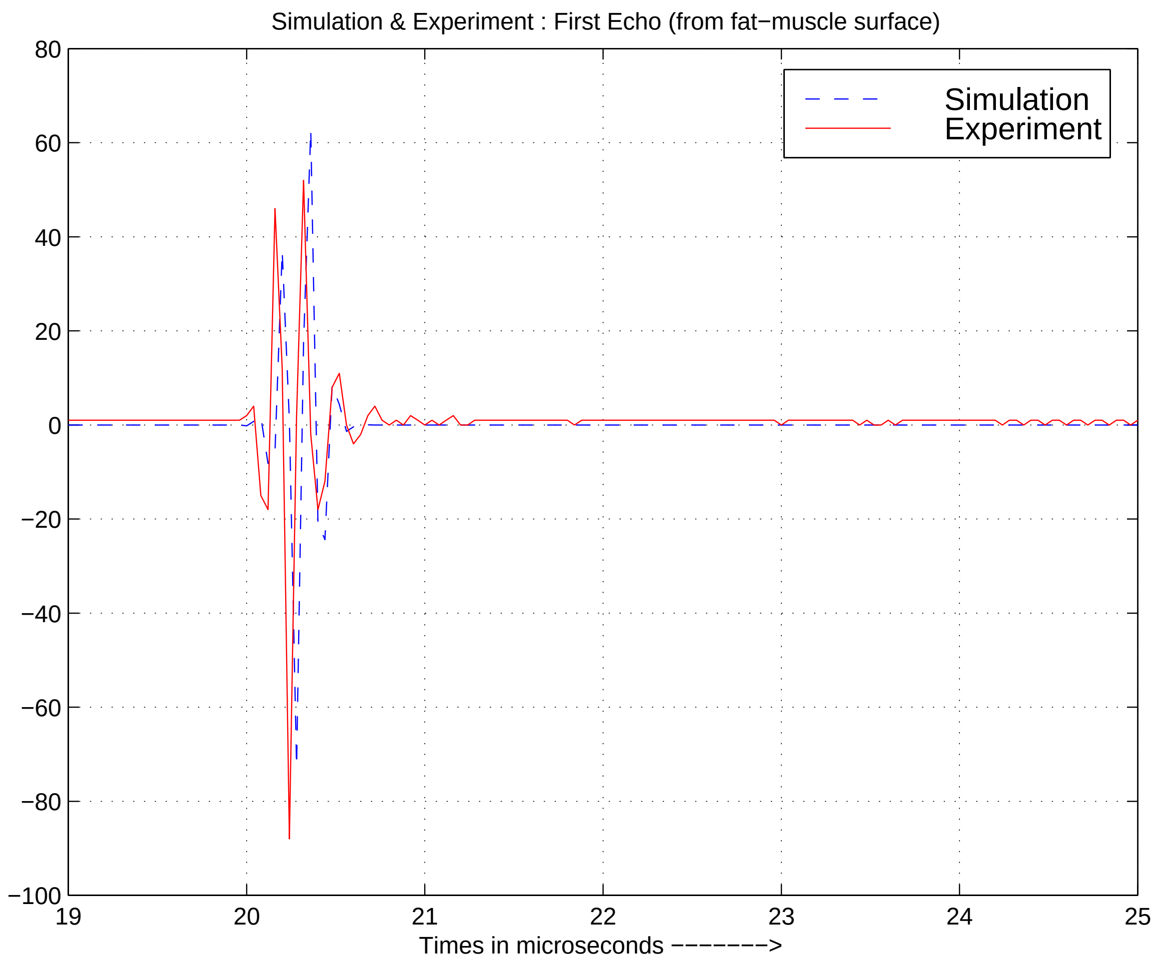

Figure 5.7: Comparison of close-up of the first echo

Comparison of Experiment with Simulation

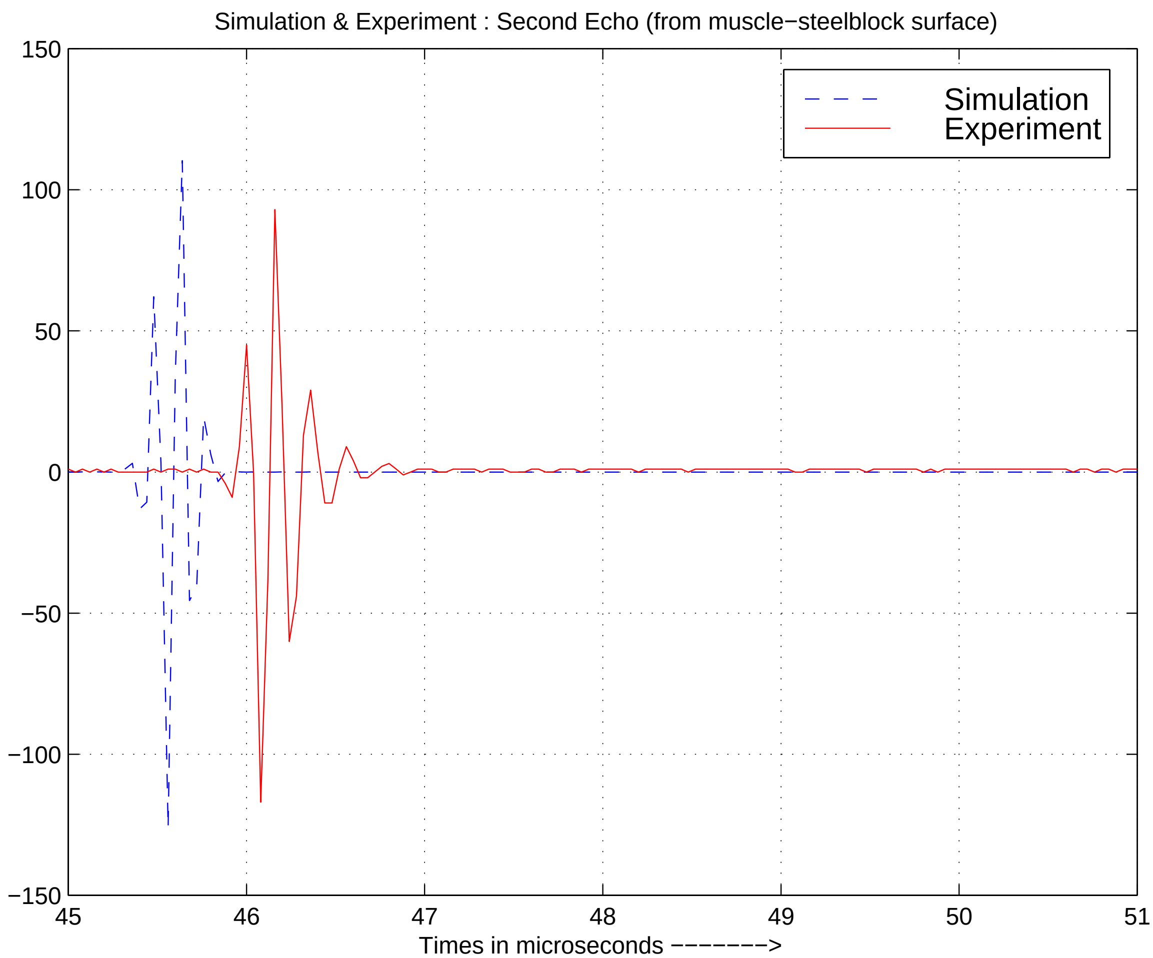

Figure 5.8: Comparison of close-up of second echo

nesses of the phantom only to within a millimeter.

These results lead us to believe that we should attempt to estimate the correct parameters (of thicknesses) first. We determine for what values of the parameters the simulation signal and the experimental signal matches the best in a mean-squared error sense. The comparison of the experimental data with the simulated signal at those parameters makes more sense.

5.3.3 Using Estimated Media Parameters

We carried out an iterative procedure to minimize the mean-squared error and to recover the depths of the planar surfaces for which the simulated data matches the experimental data best (in a mean-squared sense). [We describe the procedure in detail in the next two chapters]. We take the final parameters (depths of the two interfaces) obtained by that minimization. The depths of the first and the second interfaces at the minimum error are $D_1 = 14.9727mm$ and $D_2 = 35.4220mm$. The estimated correct thicknesses of the two layers are $14.9727mm$ and $20.4493mm$, which are within the manufacturing tolerance of the two layers. The rest of the parameters used are the same as in Table 5.3.

We compare the experimental data with the simulated signal with these estimated values of thicknesses.

Figures 5.9-5.10 we observed that the echoes qualitatively matched well with the simulation.

Table 5.4 shows the amplitude ratios and normalized RMS error.

The first entry is the ratio of RMS amplitude ratio of the experimental

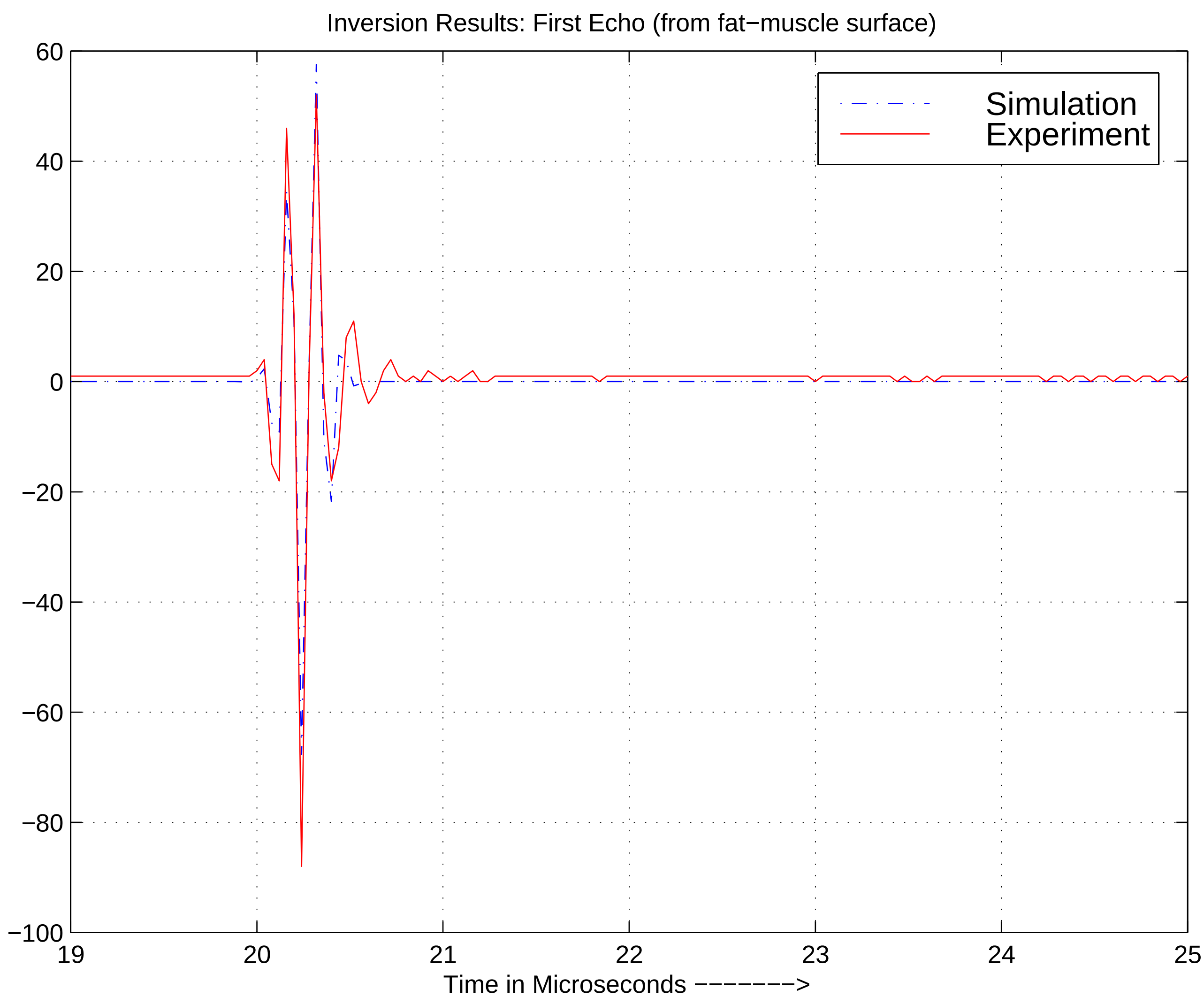

Figure 5.9: Results using modulated signals: close-up of Echo1

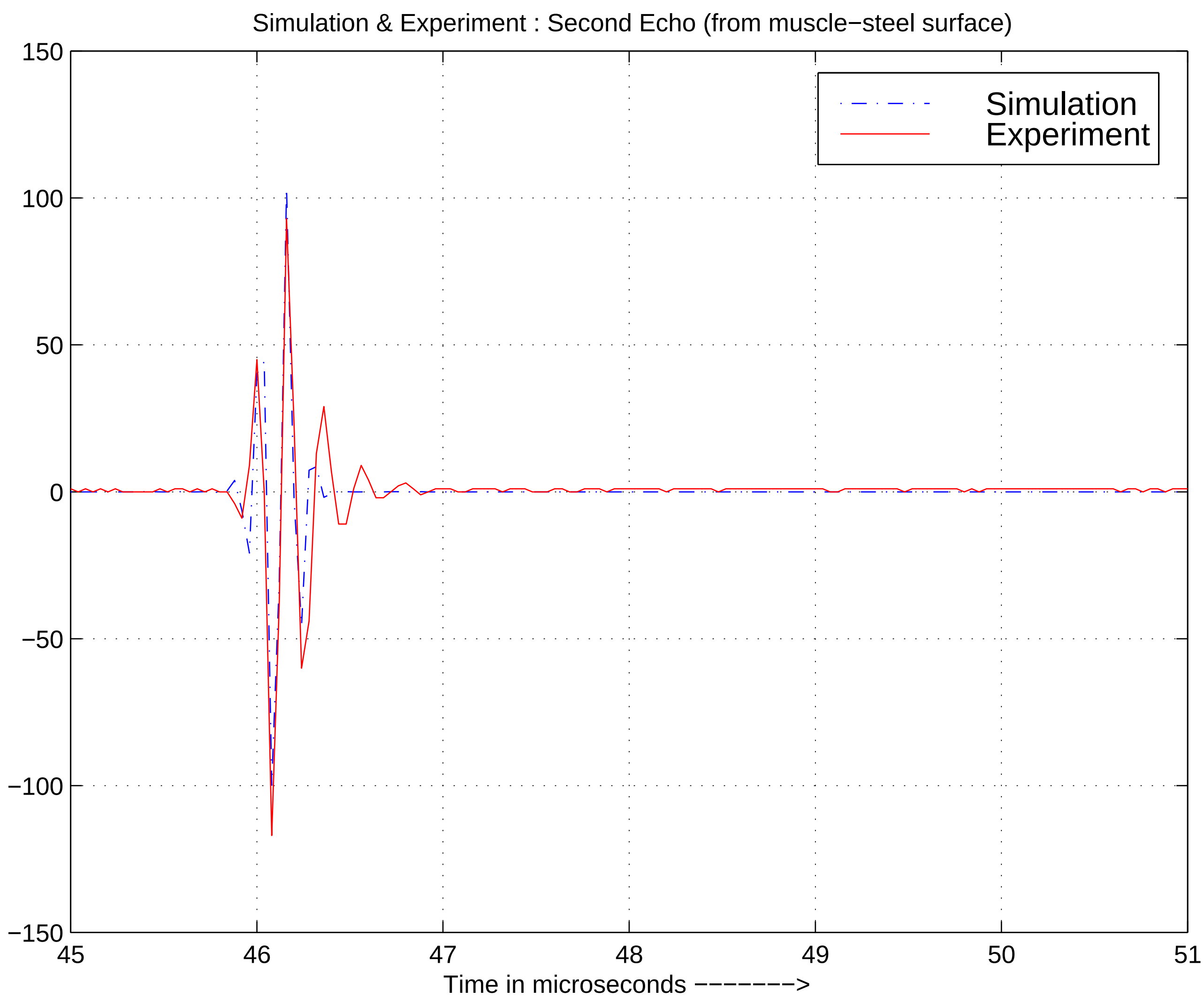

Figure 5.10: Results using modulated signals: close-up of Echo2

Table 5.4: **Relative Magnitude Comparisons**

Comparison of Experiment and Simulation	
[RMS Experiment Echo1]/[RMS Simulation Echo1]	1.0353
[RMS Experiment Echo2]/[RMS Simulation Echo2]	0.9564
[RMS Echo1]/[RMS Echo2] - simulation	0.5987
[RMS Echo1]/[RMS Echo2] - experimental	0.6481

first echo to that of the first echo of the fitted model. We see in a root mean-squared sense the match is 1.0353 (or 0.1507 db). Ideally this should be close to unity.

The second entry is the ratio of RMS amplitude ratio of the second echo, experimental to simulation. In this case the the match is -0.1936 db.

The next two entries shows the relative RMS amplitude between the first echo and the second echo for the simulation data and the experimental data respectively. Ideally these ratios should have been the same.

More quantitative comparisons between the simulation and experimental results are given in Chapter 7.

5.4 Conclusions

The simulations with the final parameters of inversion show fairly good qualitative matches with the experimental data. The differences of the shape (specially towards the ends of the echoes) is mainly due to errors in estimating the transducer pulse. The other factor is the frequency-dependence of the attenuation coefficient. In the simulation we took the attenuation at the center-frequency. For the first echo, this was expected to be not much of a problem because the attenuation coefficient itself was small for the first medium. The second medium is more attenuative. For the second echo, we do observe a small frequency-downshift of the experimental pulse relative to the simulator echo in Figure 5.10. This effect can be attributed the fact that the higher frequencies in the real signal is more attenuated than the attenuation considered at the center-frequency. And the lower ones are less attenuated than at the center frequency considered in our simulator. Another consideration is that ideally we should also have estimated the attenuation coefficients as well as the velocities, apart from the thicknesses.

Chapter 6

Numerical Inversion: Analysis and Tests

In this chapter we consider the problem of inverting the forward model derived in Chapter 4, in order to recover some of the parameters. The parameters of interest here are limited to the geometrical interfaces of the media. For our application of interest, our aim would be to recover the surface of the bone, which would correspond to the second (reflective) interface. However, the method is applicable for recovery of the physical parameters as well.

We consider the case of two layers over a reflective medium, as considered in Chapter 4. The layers are both parallel to the aperture. In this case the inversion is with respect to two parameters, the depths of the two interfaces.

Here we analyze the objective function and point out a few inherent problems. We overcome some of the problems and show test cases of the inversion using a non-linear iterative technique, Levenberg-Marquardt.

6.1 Parameter Recovery by Iterative Inversion

We refer to the block diagram in Figure 6.1. We start with an initial guess of the parameter values, in this case the depth of the two interfaces from the aperture. The parameters are used by the forward transform F and we get a synthesized signal output (or an ultrasound image in general).

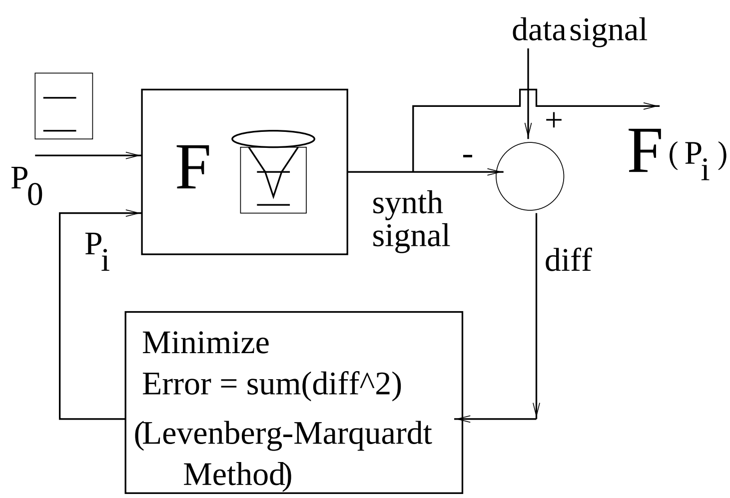

Figure 6.1: Iterative Inversion

The error difference between the synthesized output (or some processed version of it) and the data signal (processed in the same way) drives the parameters to their next values. We adopt the Levenberg-Marquardt inversion method [19] for this purpose.

The output signal from the receiver in our case is a time signal, $y = y(n; \mathbf{p})$ where n is the time sample index and $\mathbf{p}$ is the parameter set used. In this case the parameter set consists of the two depths of the planar interfaces, given by D_1 and D_2.

The scalar error that is minimized is given as follows,

$$E(\mathbf{p}) = \sum_n (y_n - y(n;\mathbf{p}))^2 \tag{6.1}$$

Before proceeding with the inversion, we test and evaluate the error function at different frequencies.

6.2 Error Function Analysis

We consider the difference of the signals, $y(n;\mathbf{p})$ and y_n and compute the error function given by

$$E(\mathbf{p}) = \sum_n (y_n - y(n;\mathbf{p}))^2 \tag{6.2}$$

6.2.1 Testing of Error Functions at 1, 1.5 and 2 MHz

We test the error function at relatively smaller frequencies rather than the experimental case (of about 7 MHz) because of computational convenience. In our simulation code, the aperture is sampled at $\lambda/8$ in each dimension. Hence the speed is inversely proportional to f^2. The lower the frequencies, the faster is the code and easier it is to test with. We keep the sampling frequency the same (at 25 MHz).

Let us investigate the errors at 1 MHz. For purpose of evaluation we take the "data" signal, y_n as the *simulated* output signal at parameter $D_1 = 10mm$ and $D_2 = 20mm$. Then, we change the parameters and simulate the output signal at various values of the parameters and compute the error with this "data" y_n.

Figure 6.2 shows the error when depth of the second interface D_2 is kept fixed at $D_2 = 20mm$ and D_1 is varied. When we fix the depth of the first interface $D_1 = 10$ and D_2 is varied we get the error function as in Figure 6.3. We vary both D_1 and D_2 we get the error function given in Figure 6.4.

We observe that at the "correct" parameter values, at $D_1 = 10mm$, $D_2 = 20mm$ we obtain the expected zero-error for all three plots. However, there are oscillations around that value giving local minima. These minima are regularly spaced and as calculations showed, at intervals of the wavelength, from the global minima.

Another interesting effect is that there is an overall declining trend in the error function in Figure 6.3. We will analyze this effect and also its absence in the first case (Figure 6.2) at a later section.

The third observation is that the error plot with respect to D_1 and D_2 in Figure 6.4 is very "flat", in one direction (along D_1). From Figures 6.2 and 6.3, we see that the error is about ten times smaller when varying D_1 as opposed to varying D_2. Hence we see the "flatness" of error in Figure 6.4. This does not pose a serious problem if during our minimization we use second order terms. We will discuss this later.

6.2.2 Oscillations around global minimum

First we try to explain the oscillations around the global minimum and try to arrive at a method to remove the oscillations.

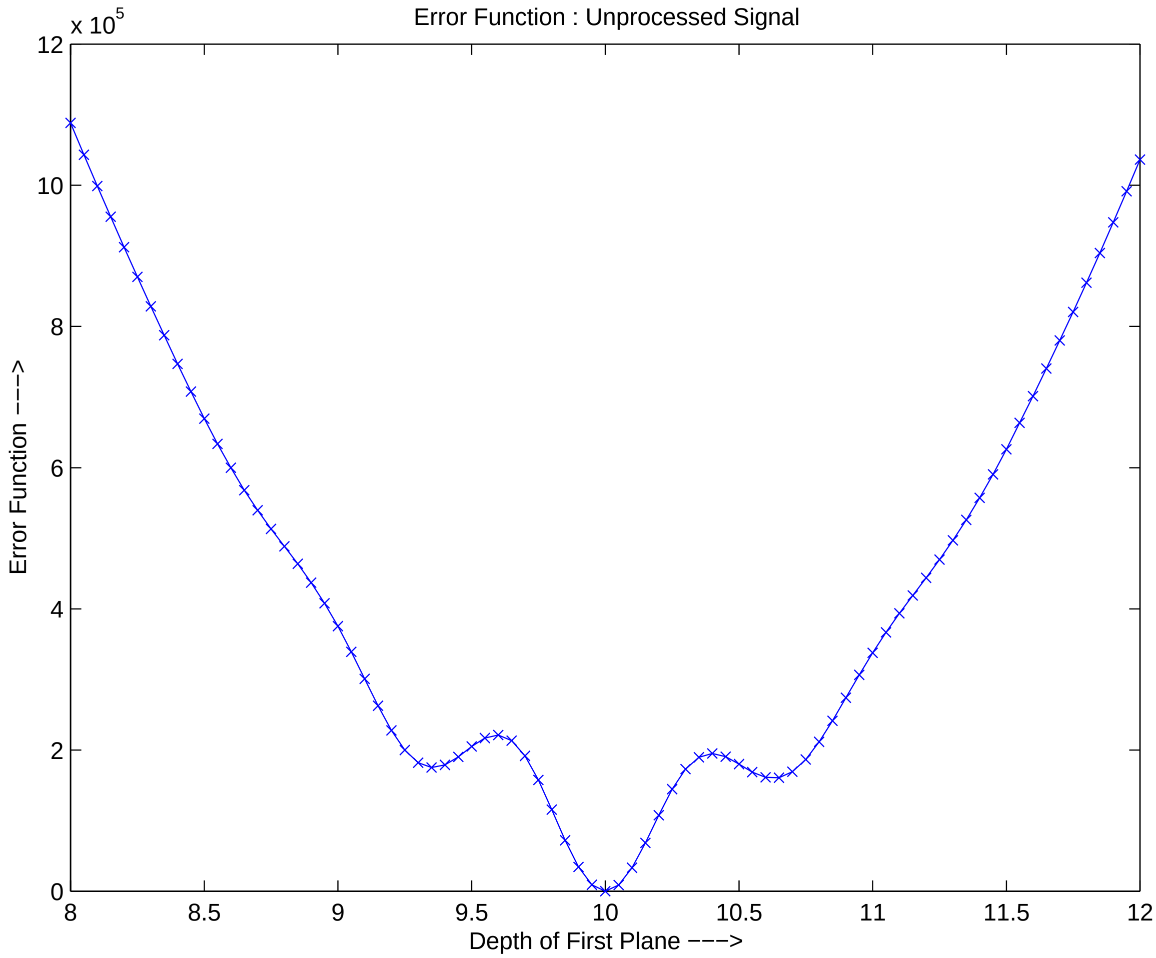

Figure 6.2: Error Function when varying D_1

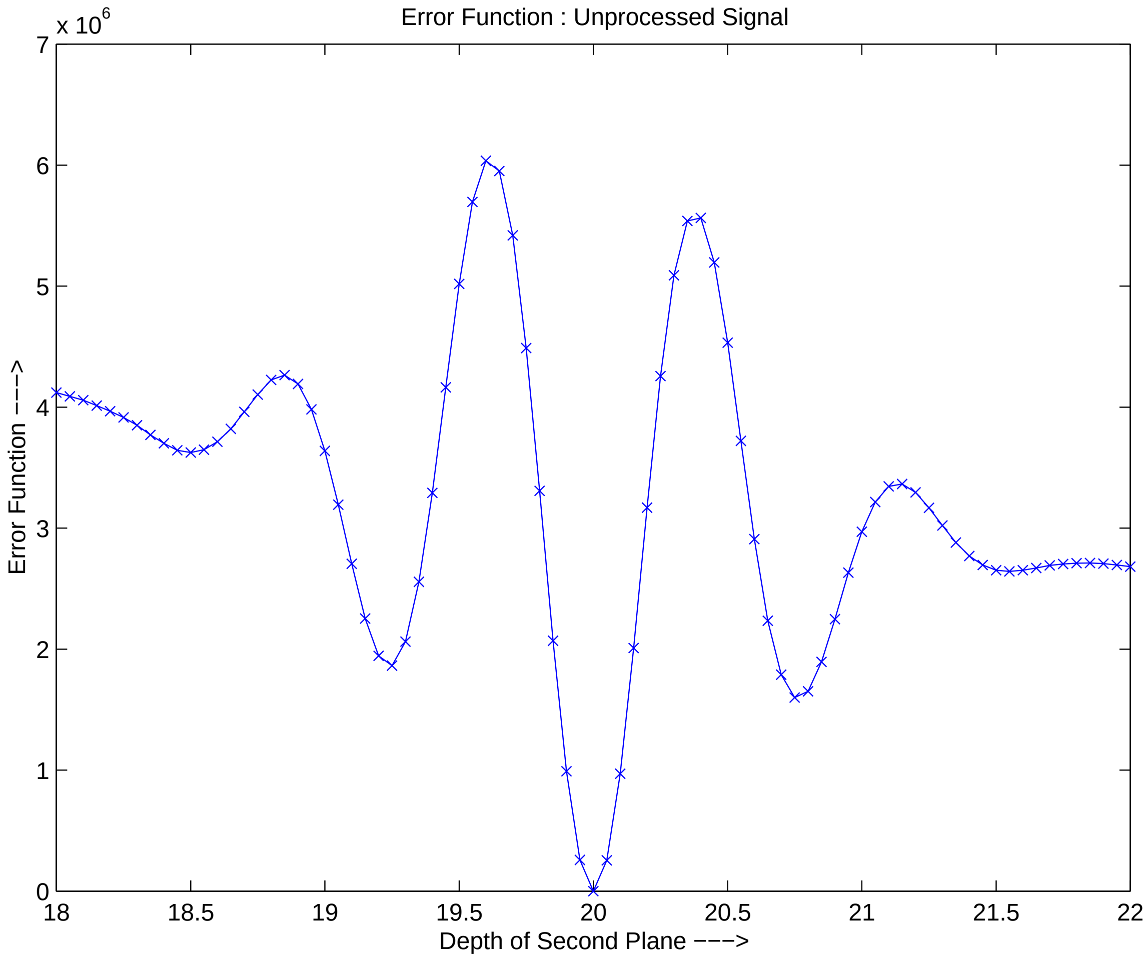

Figure 6.3: Error Function when varying D_2

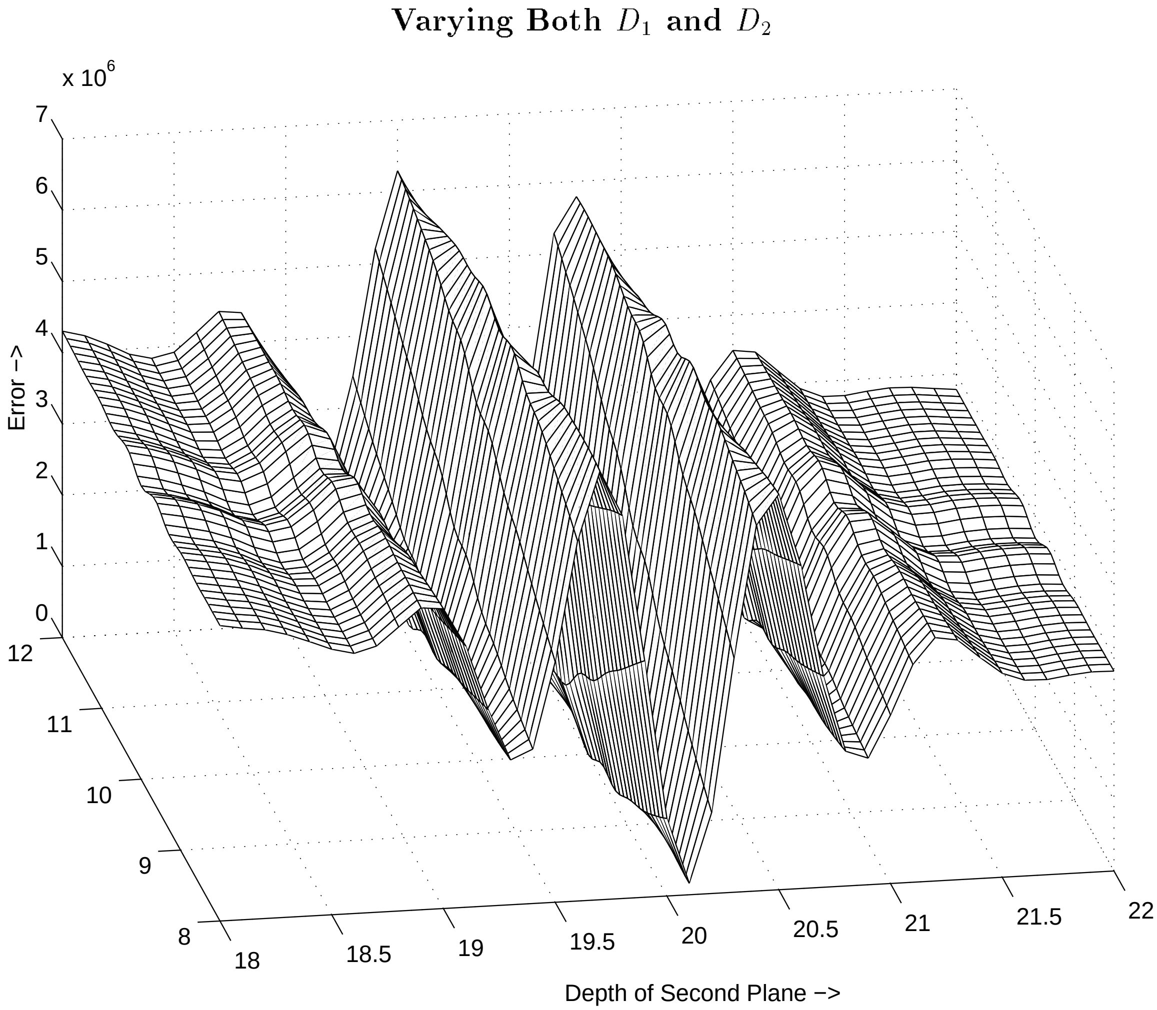

Figure 6.4: Error Function when varying D_1 and D_2

These minima are spaced at roughly the λ intervals corresponding to the wavelength λ of modulation and are due to local matches of the oscillations at intervals of λ. To explain this more clearly, we show the signal y_n and $y(n;\mathbf{p})$ at a minima and a maxima.

We choose the minima at (roughly) $D_2 = 19.2mm$ and maxima at (roughly) $D_2 = 19.6mm$ in Figure 6.3.

The data signal y_n and $y(n,\mathbf{p})$ are plotted for these two cases ($D_1 = 10mm$) in Figure 6.5.

We see that for the first case, (at $D_2 = 19.2mm$) the oscillations match in phase. Hence the error is smaller. But for the second case, (at $D_2 = 19.6mm$), the oscillations are out of phase and the error rises sharply.

To confirm this further, we redo the error function for frequencies 1.5 MHz and 2 MHz to check if the oscillation intervals reduce appropriately. In Figures 6.6 and 6.7 we have the two error sets of functions. We observe that the oscillation intervals are again λ. In particular, the interval at the 2 MHz case in Figure 6.7 is half of that for the 1 MHz cases shown in Figures 6.2 and 6.3.

This indicates that we should attempt to demodulate the signal. The envelopes of the signals should be involved in the minimization, rather than the signals themselves.

6.2.3 Pre-processing the signals

In the last section, we observed that the modulation of the signals causes minima in the error function around the global minima. To address this

Minima

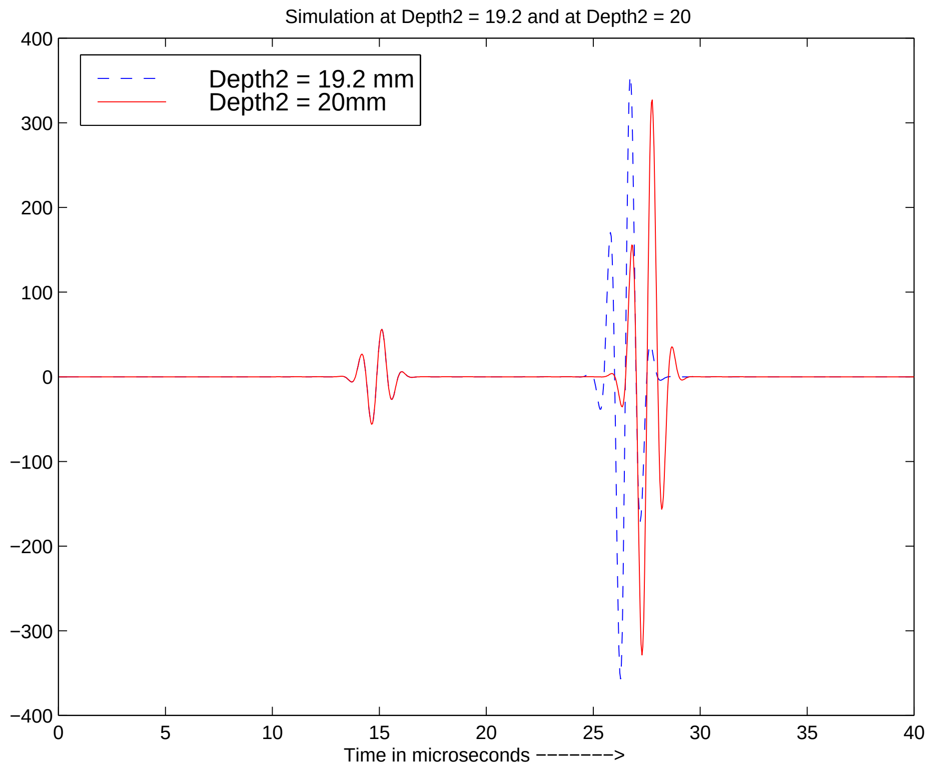

Maxima

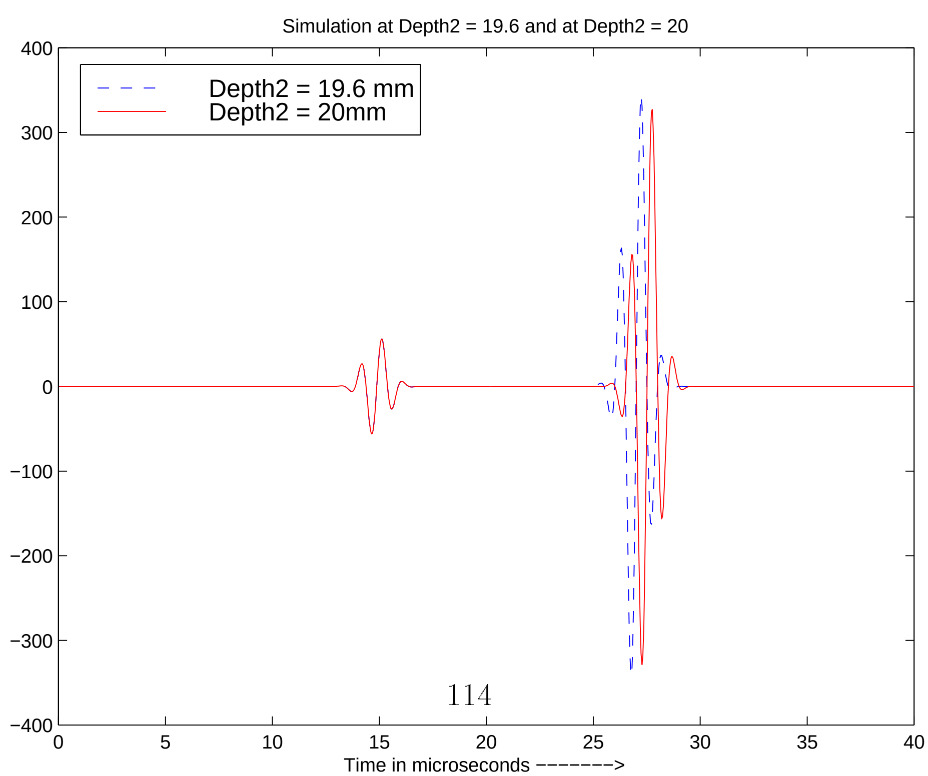

Figure 6.5: Simulator Outputs for Parameters at Minima and Maxima of Error

(a) Varying D_1, keeping $D_2 = 20mm$

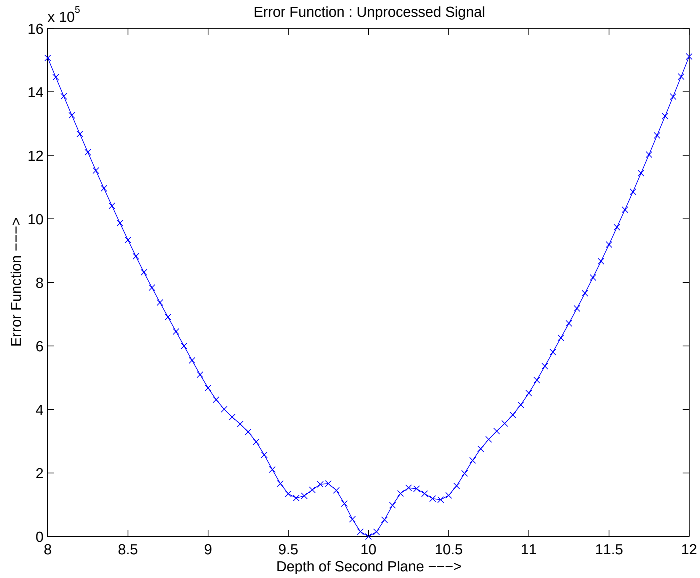

(b) Varying D_2, keeping $D_1 = 10mm$

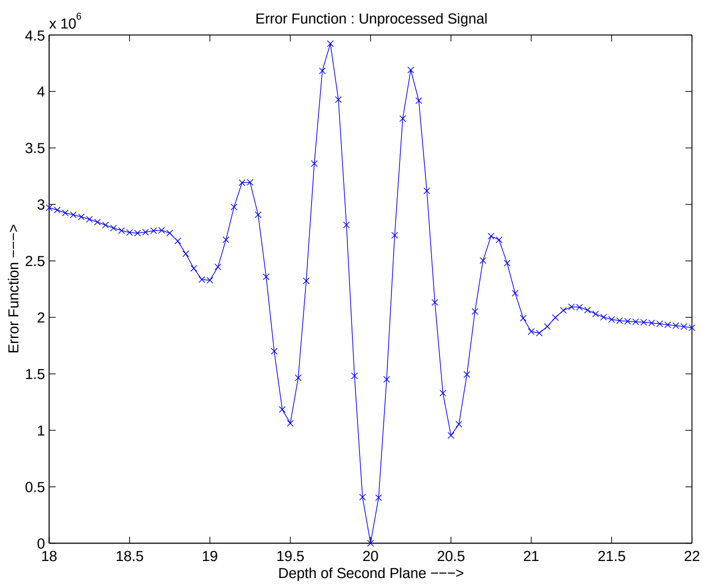

Figure 6.6: The Error Functions for 1.5 MHz

(a) **Varying** D_1, **keeping** $D_2 = 20mm$

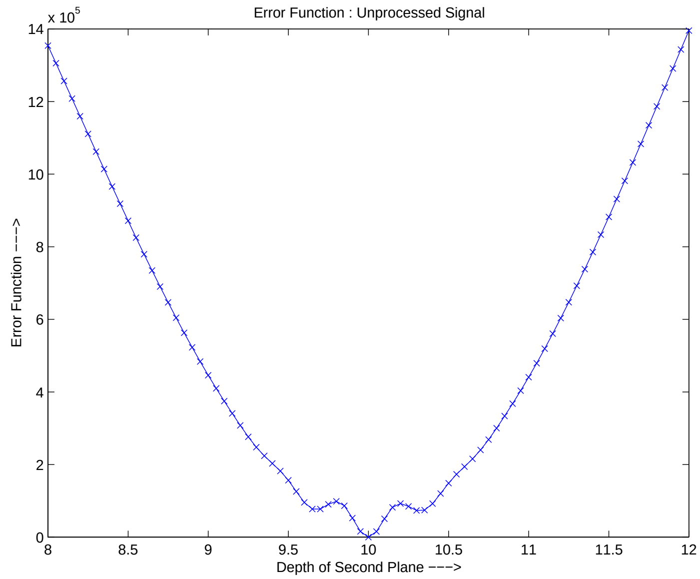

(b) **Varying** D_2, **keeping** $D_1 = 10mm$

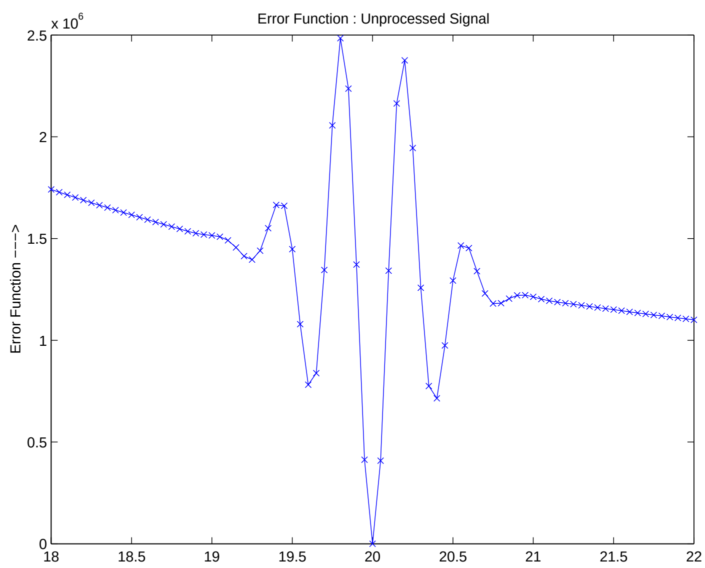

Figure 6.7: The Error Functions for 2 MHz

problem we simply try to obtain a demodulated signal before considering their difference. Let s_n and $s(n, \mathbf{p})$ be the processed signals. Ideally we want a processing that would give an "envelope" signal and also preserve the energy.

The original signal has a maxima at the carrier frequency, f_0. Since the output is a real signal, the FFT is conjugate symmetric ; the real part is symmetric, the imaginary part is antisymmetric. All the information of the signal is inherent in a signal consisting of the real and imaginary "humps" centered around f_0. We extract these "humps" in the following three steps shown in Figure 6.8. At the Step II, we obtain a signal $G_r(f)$ and $G_i(f)$.

The IFFT of $G(f)$ gives a time signal which is however complex in general (because the individual humps in the original signal may not be conjugate symmetric in general). After some manipulations, we can derive the original signal y_n in terms of the derived signal $g(n)$ as

$$y_n = g(n)e^{-jw_0 n} + g^*(n)e^{jw_0 n} \tag{6.3}$$

Since $g(n)$ is complex, it is difficult to use in the minimization. Hence we multiply $g(n)$ by its complex conjugate to obtain a real output. We notice that we have only one half of the original signal in terms of energy, because we only considered one-side of the frequency axis. Hence we also multiply by a factor of two, to finally obtain,

$$s_n = \sqrt{2g(n)g^*(n)} \tag{6.4}$$

Note that by these "demodulation" steps the energy is preserved, that is,

Step 0: $\mathbf{Y(f) = FFT(y_n)}$

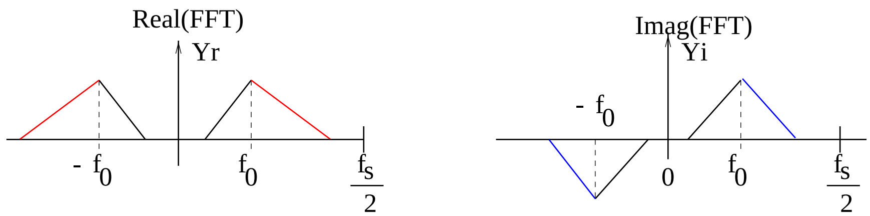

Step I: One sided filtering

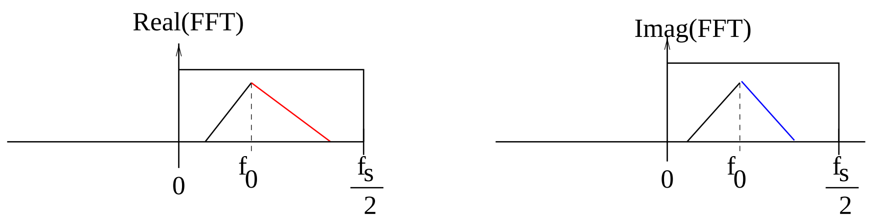

Step II: Shift

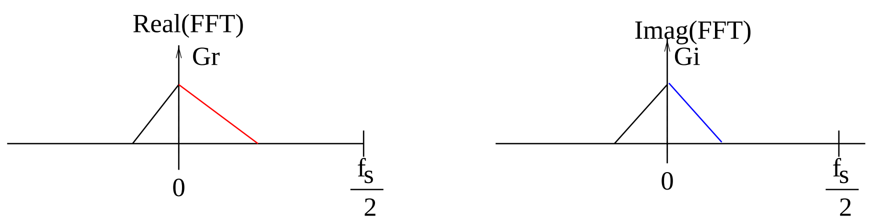

Step III : Take IFFT

$$g(n) = IFFT[G_r(f) + jG_i(f)]$$

Step IV: Sqrt of Energy Function

$$s_n = \sqrt{2g(n)g^*(n)}$$

Figure 6.8: Processing Steps

$$\sum_n s_n^2 = \sum_n y_n^2 \tag{6.5}$$

In Figures 6.9 and 6.10 we give an example of this transformation for a signal y_n at 1 MHz. The lighter plot is the FFT of the original signal. We observe that the FFT is centered at 1 MHz. We extract one side of the FFT first and shift it to zero, to obtain $G(f)$.

We take the IFFT of $G(f)$ to get g_n and obtain s_n according to Equation 6.3. The "envelope" signal s_n and the original "modulated" signal y_n are shown in Figure 6.10 in dashed and solid lines respectively.

We do a similar processing on the simulation output $y(n, \mathbf{p})$ to obtain $s(n, \mathbf{p})$.

6.2.4 Error Function with Pre-processed Signal

We compute the error function given in Equation 6.1 on the "demodulated" signals, s_n and $s(n, \mathbf{p})$ and obtain smoother bowls. Figure 6.11 shows the results for varying D_1 while keeping D_2 fixed as well as varying D_2 while keeping D_1 fixed. It is apparent that the oscillations near the global minima have been removed.

Figure 6.11 shows the error with varying D_1 and D_2, similarly smoothed.

6.2.5 Declining Trend in Error

We come to the second problem factor in the error function. When we vary the parameter D_2, there is an overall declining trend, apparent with or without modulation (Figure 6.11 or Figure 6.3). This is a problem because if

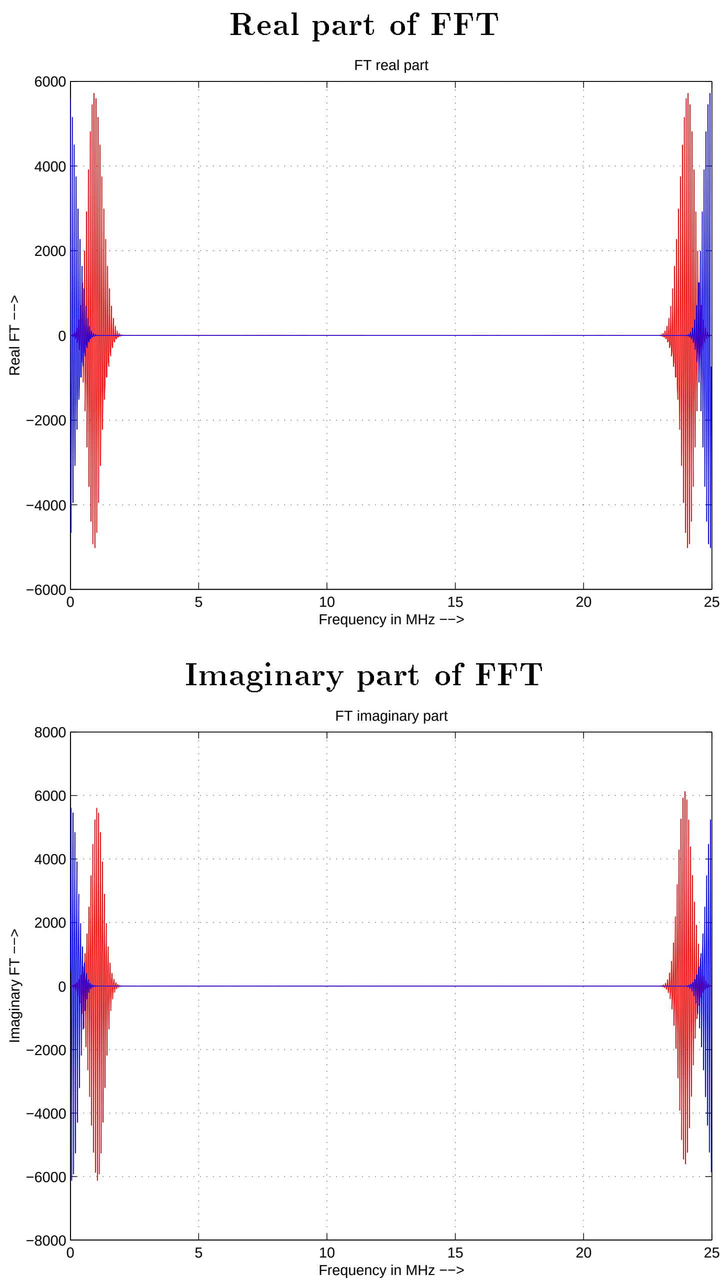

Figure 6.9: Real and Imaginary FFTs : $Y(f)$ (centered at 1 MHz) and $G(f)$ (shifted to zero)

Time domain: Original and Processed signal

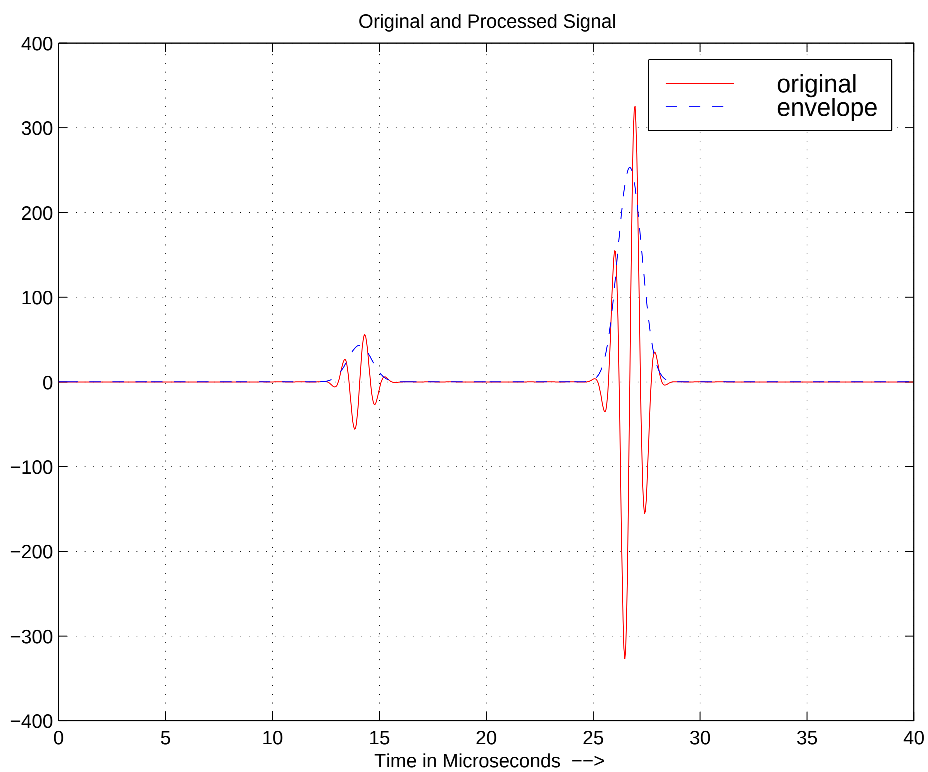

Figure 6.10: Time domain : y_n and s_n

(a) **Varying** D_1**, keeping** $D_2 = 20mm$

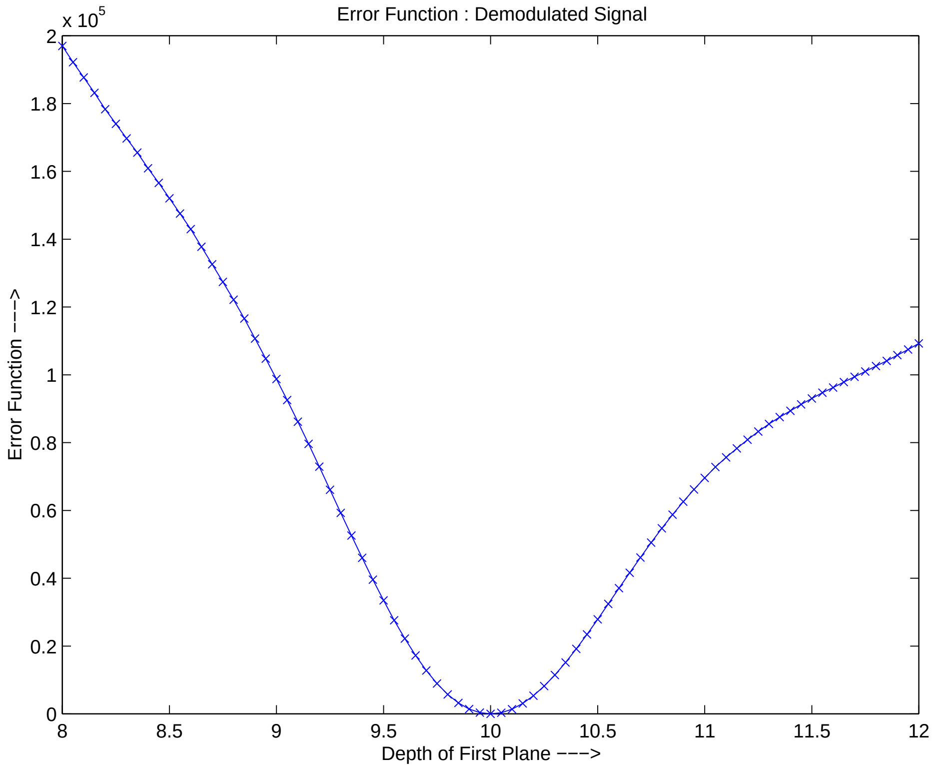

(b) **Varying** D_2**, keeping** $D_1 = 10mm$

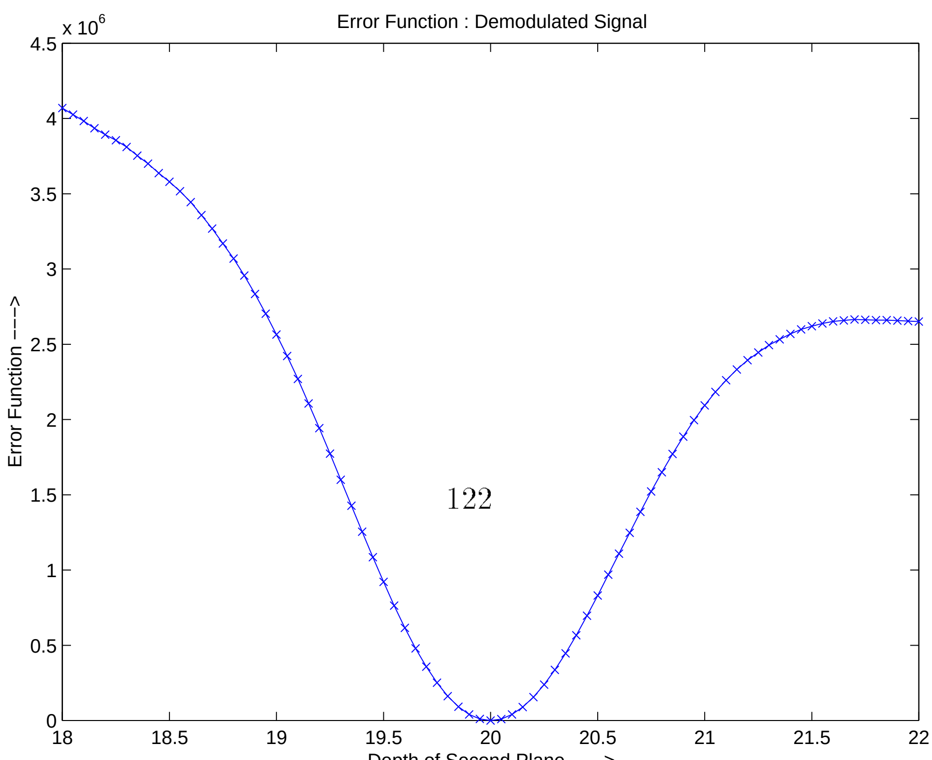

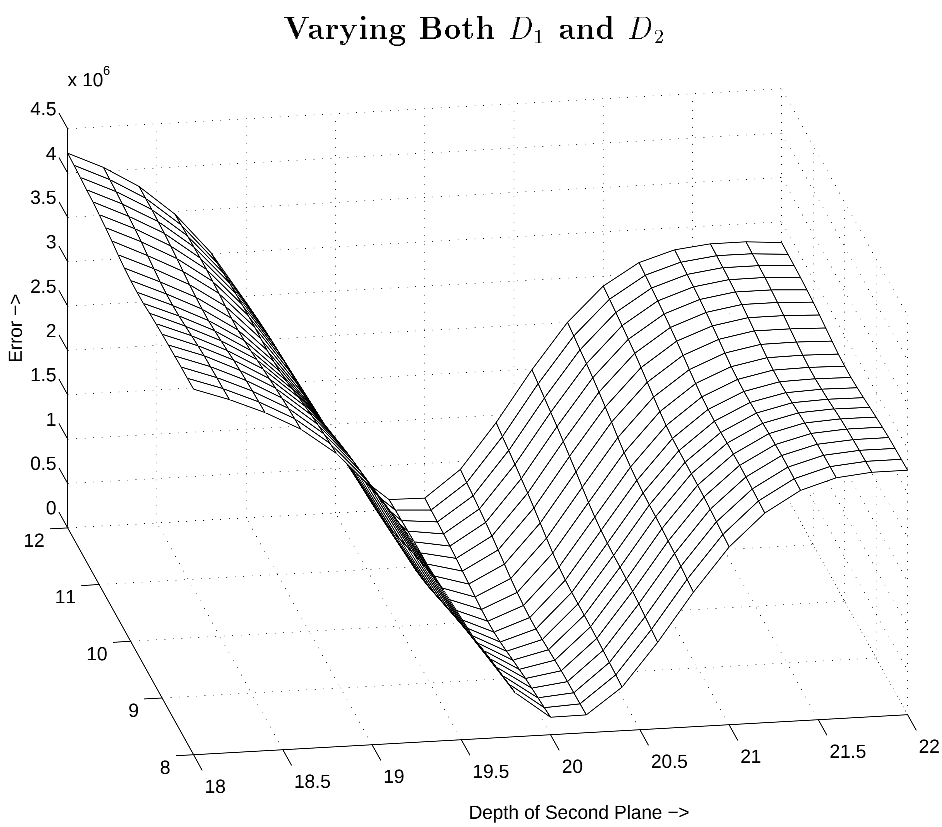

Figure 6.12: Error Function Varying D_1 and D_2 for Demodulated Signals

we happened to start at a point beyond the error bowl, we go further and further away. We ignored this effect earlier to consider the more crucial oscillations very near the global minimum. Now we can investigate this declining trend, very pronounced in Figure 6.3 (modulated case), less pronounced but present, in Figure 6.11 (demodulated case).

We take the demodulated case to explain this effect. Figure 6.13 plots the signals $s(n, \mathbf{p})$ for three different values of $D_2 = 23, 24, 25mm$, keeping $D_1 = 10mm$. For each of these, we superposed the "data" signal, s_n at $D_2 = 20mm$ ($D_1 = 10mm$).

We observe that the echoes do not overlap and they are reducing in magnitude. The decreasing nature of the echoes with depth makes sense physically. There is increasing attenuation (due to spreading factor, backscatter and absorption) with increasing depth.

We investigate the difference signal,

$$d(n) = s_n - s(n; \mathbf{p}) \tag{6.6}$$

The difference signals are plotted in Figure 6.14 for the three values of D_2 chosen.

The reason for the declining trend is obvious from the Figure 6.14 (b). The first "hump" common to the three difference signals belongs to the "data" signal s_n and located corresponding to a depth of $D_2 = 20$. At depths $D_2 = 23, 24, 25mm$ the humps have ceased to overlap (with that at $D_2 = 20mm$) and hence appear in the difference function in totality (the negative ones in Figure 6.14). It is evident that these are decreasing in amplitude with depth.

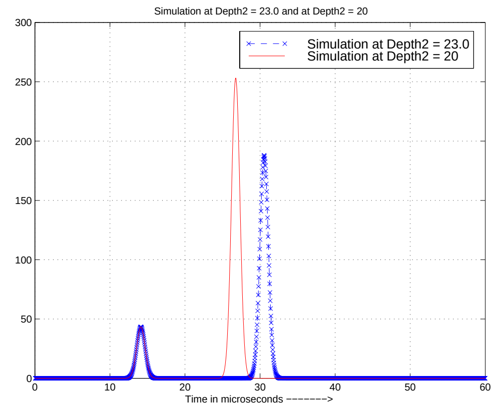

(a) Demodulated Signal at $D_2 = 20$ and $D_2 = 23$ ($D_1 = 10$)

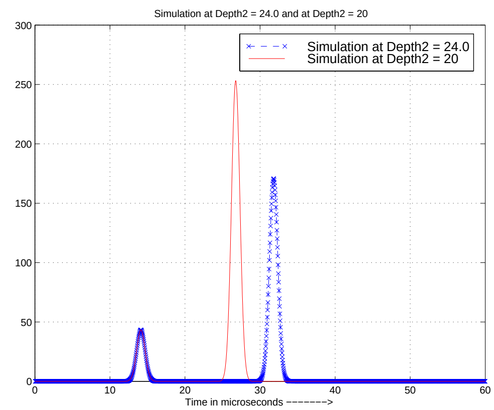

(b) Demodulated Signals at $D_2 = 20$ and $D_2 = 24$ ($D_1 = 10$)

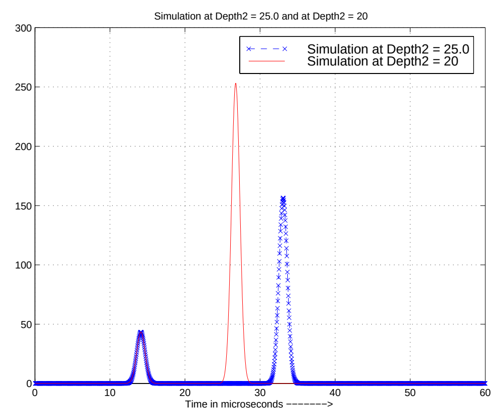

(c) Demodulated Signal at $D_2 = 20$ and $D_2 = 25$ ($D_1 = 10$)

Figure 6.13: Demodulated Signals for $D_2 = 23, 24, 25mm$ and "data" at $D_2 = 20mm$

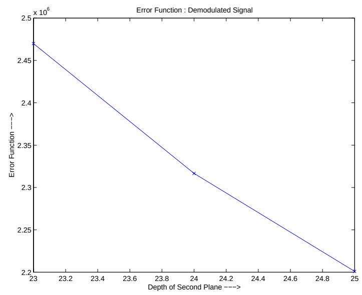

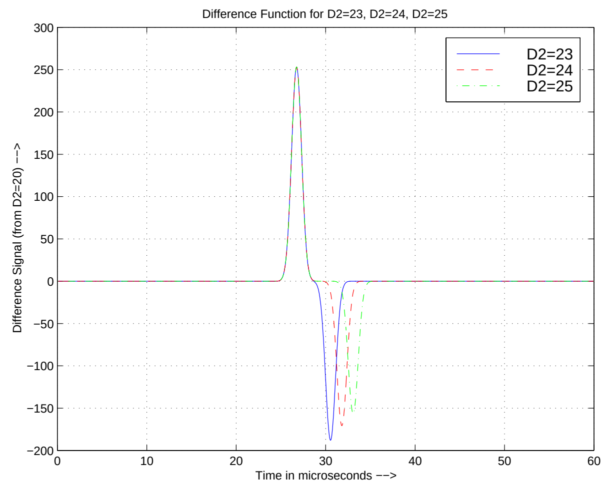

(a) Errors at $D_2 = 23, 24, 25mm$ (b) The Corresponding Difference Signals

Figure 6.14: Difference from signal at $D_2 = 20mm$ for $D_2 = 23, 24, 25mm$

This results in the overall decrease in the error after certain value of D_2. In the asymptotic limit, as the echoes reduce to negligible amplitudes with depth, we the error would go to the square of the magnitude of the second echo of the "data" signal (the positive "hump") in Figure 6.14.

We see that this trend is a problem that we cannot avoid easily. If we happened to start our minimization at a region of D_2 beyond the bowl in the error function Figure 6.11 (b), it never comes back to the bowl but goes further and further away. However it maybe possible to detect by the slope if the minimization is in such a shallow zone or actually inside the error bowl.

Another point to note is that this effect is enhanced for higher frequencies, Figures 6.6(b) and 6.7(b) because a big factor contributing to the trend here, the backscattering and absorption attenuation, increases with frequency.

This raises the next question - why this effect was not present when we varied D_1 keeping D_2 fixed (at 20mm), Figures 6.2 and Figure 6.11(a). To investigate this, we looked at the signal $s(n, \mathbf{p})$ for some large enough values of depths of first plane D_1. We choose $D_1 = 13, 14, 15mm$ for our tests.

As obvious physically and evident from the signals plotted in Figure 6.15, when we change the depth D_1 the second echo varies as well, even though the second depth is held constant. This change in the second echo when we shift D_1 is due to the change in the length of the rays in the second medium. A big factor in the amplitude, the backscatter attenuation factor is particularly sensitive to this change. The change due to other factors are not significant in comparison.

The difference with the s_n for $D_1 = 10mm$ for the three $s(n, \mathbf{p})$ signals at $D_1 = 13, 14, 15mm$ is displayed in Figure 6.16. We observe that in these particular configurations, the increased difference in the second echo more than compensates for the reduction of error due to reduction of the first echoes with depth. This is the reason why the overall error actually increases for this case instead of decreasing. This is a factor in our favor of course.

The last factor was the relative flatness in one direction. We would like to mention that since we are using inversion methods which has second order terms (such as Levenberg-Marquardt), the relative flatness would not pose a ultimate problem. So long as there is a curvature in both directions (which there is), it should work. In the next section we consider a few runs of the Levenberg-Marquardt inversion.

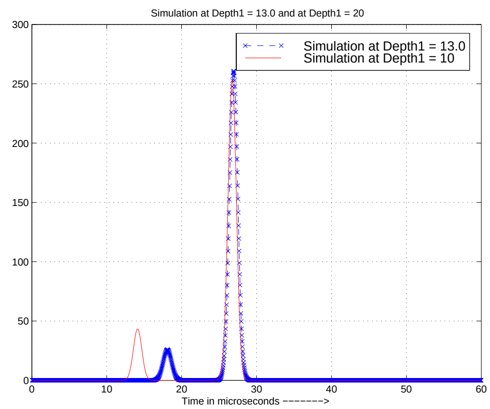

(a) Demodulated Signal at $D_1 = 10$ and $D_1 = 13$ ($D_2 = 20$)

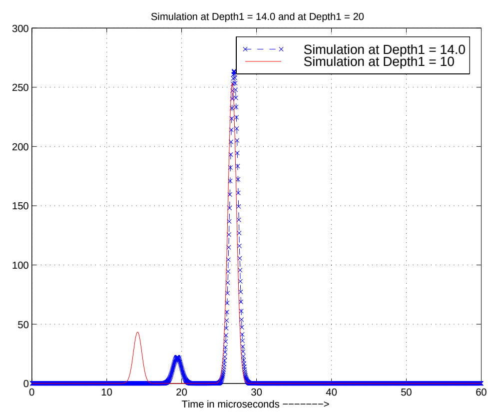

(b) Demodulated Signal at $D_1 = 10$ and $D_1 = 14$ ($D_2 = 20$)

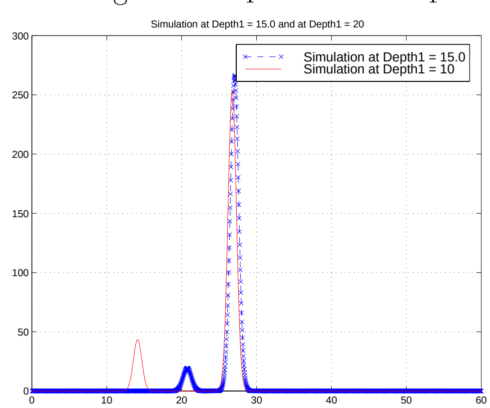

(c) Demodulated Signal at $D_1 = 10$ and $D_1 = 15$ ($D_2 = 20$)

Figure 6.15: Demodulated Signals for $D_1 = 13, 14, 15mm$ and "data" at $D_1 = 10mm$

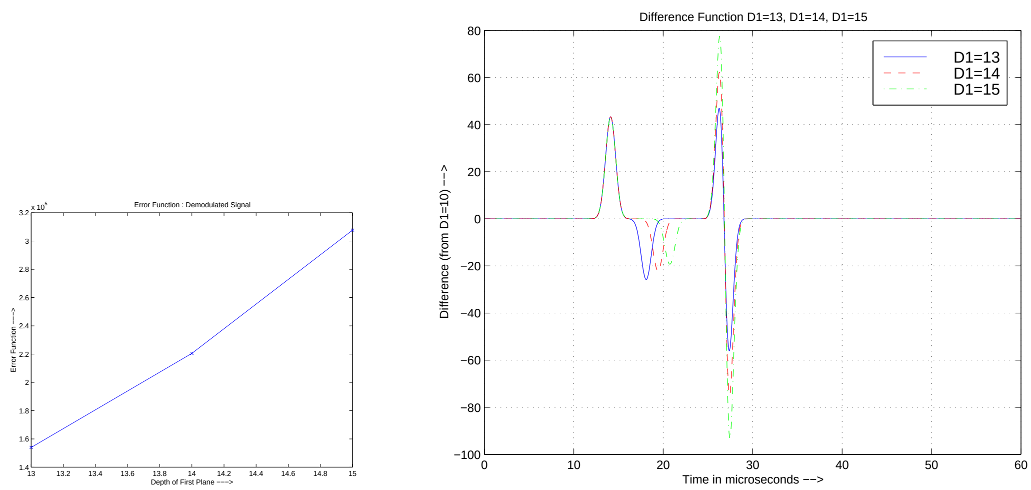

(a) Errors at $D_1 = 13, 14, 15mm$ (b) The Corresponding Difference Signals

Figure 6.16: Difference from signal at $D_1 = 10mm$ for $D_1 = 13, 14, 15mm$

6.3 Levenberg-Marquardt Inversion

The steps of Levenberg-Marquardt Inversion are described in [19]. This method smoothly varies between the gradient descent method and inverse Hessian method.

The objective function and its first and second derivatives are used in this minimization. The objective function is given in Equation 6.1, repeated here for convenience.

$$E(\mathbf{p}) = \sum_n (y_n - y(n; \mathbf{p}))^2 \tag{6.7}$$

The gradient of $E(\mathbf{p})$ is

$$\frac{\partial E(\mathbf{p})}{\partial p_k} = -2 \sum_n (y_n - y(n; \mathbf{p})) \frac{\partial y(n; \mathbf{p})}{\partial p_k} \tag{6.8}$$

where $k = 1, 2, ..., M$ are denote the k-th parameter.

Taking an additional partial derivative,

$$\frac{\partial^2 E(\mathbf{p})}{\partial p_k p_l} = 2\sum_n [\frac{\partial y(n;\mathbf{p})}{\partial p_k}\frac{\partial y(n;\mathbf{p})}{\partial p_l} - (y_n - y(n;\mathbf{p}))\frac{\partial^2 y(n;\mathbf{p})}{\partial p_k p_l}] \tag{6.9}$$

It is conventional to remove the factor of 2 in Equations 6.8 and 6.9. [19] we define use β_k and α_{kl} which are half of the gradient and the second-order derivative respectively.

$$\beta_k = -\frac{1}{2}\frac{\partial y(n;\mathbf{p})}{\partial p_k} \tag{6.10}$$

and

$$\alpha_{kl} = \frac{1}{2}\frac{\partial^2 E(\mathbf{p})}{\partial p_k p_l} \tag{6.11}$$

It is common to ignore the second-order derivatives in Equation 6.9 and calculate the Hessian α-matrix using only the product terms of the first order derivatives. This is because the second order derivatives can lead to instabilities and near the global-minimum, the product terms of first order derivatives approximate the Hessian matrix well [19], because error term multiplying the second order factor is small. The α-matrix is 2x2 in our simple 2-parameter case.

To go smoothly between gradient descent, and the inverse-Hessian approach, a parameter g [1] is to be chosen and a new α-matrix is defined as prescribed in [19].

[1]The reason we use the term "g" here and not λ as in [19] is to avoid confusion with the wavelength λ.

The diagonal elements of the new matrix are given by,

$$\alpha'_{jj} = \alpha_{jj}(1+g) \tag{6.12}$$

The other elements remain the same as that of α.

Then we can solve the set of equations equation

$$\sum_{l} \alpha'_{kl}\delta_l = \beta_k \tag{6.13}$$

to obtain the parameter increment vector δ.

When g is large, the matrix α' is diagonally dominant and the minimization is like gradient-descent. When g is small, the minimization goes towards the inverse-Hessian. More details can be found in [19].

We computed the derivatives with respect to the parameters symbolically in Maple and incorporated them in the C-simulator. It took about one-third of the time more to compute the derivatives than the time it took to compute just the signal output of forward model.

For the demodulated signals, the derivative terms are obtained from the derivatives of the original signals, using the relation given in Equation 6.4.

6.3.1 Inversion Results for Synthetic Cases

We show some results of the 2-parameter inversion for a synthetic case in Figure 6.17. For this case, the data signal s_n is the computed demodulated signal output at $D_1 = 10mm$, $D_2 = 20mm$. Then we start with an initial guess of the parameters, at $D_1 = 8.5mm$, $D_2 = 18.6mm$ and compute the difference function and the derivatives. We update the parameters using the gradient and Hessian. The iterations converged to the right parameters in 14 iterations to within 5 decimal places. The error converged to the expected zero value. In the plot we show a few more iterations.

Then we start with a different initial guess of the parameter, further away. The starting guess is at $D_1 = 8mm$, $D_2 = 18mm$. The error and parameter convergence plots are shown in Figure 6.18. The iterations converged to the right parameters in about 42 iterations (to within 5 decimal places). The error converged to the expected zero value.

However we see an interesting phenomenon in this case. Initially the depth D_1 started moving away from the right value. The depth D_2 went steadily towards the right value. The error steadily decreased. When it came very near the correct value, the D_1 moved back the right direction and eventually both the parameters converged. But this increased the no. of iterations about three times.

The reason for the initial shift of the depth away from the correct parameter value and towards the aperture can be explained physically. In a nutshell, when D_1 shifts up, the effective length of the rays increases in the second medium, and can result in reducing the second echo, which in turn would reduce the error with the "data" signal s_n at $D_2 = 20mm$. Because of the relative magnitudes of the echoes, the error reduction in second echo can more than compensate for the increase in error in the first echo.

We show a few plots of the intermediate iterations to show that this is indeed what happens.

In Figure 6.19 we show the error-functions for the individual echoes as well as the total error for the entire set of iterations. To make more sense of

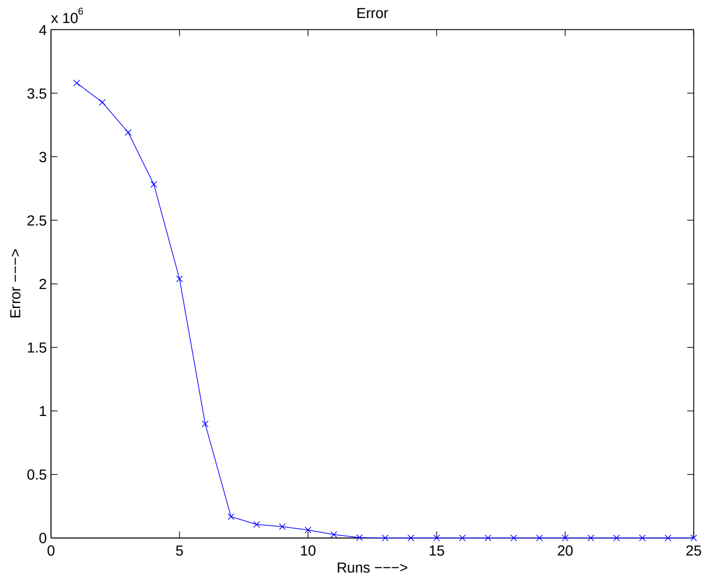

(a) Error Function Convergence

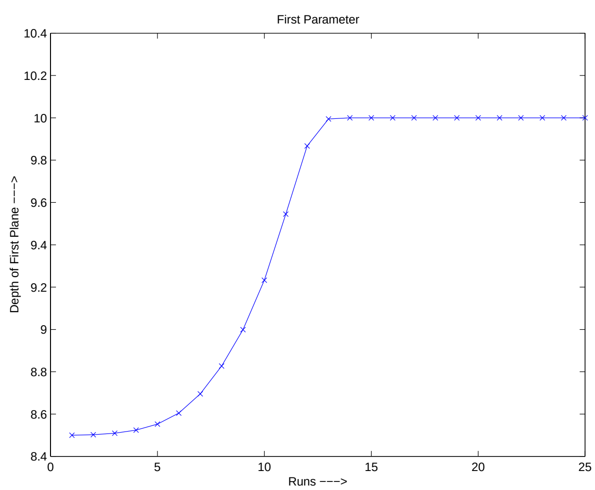

(b) First Parameter, D_1

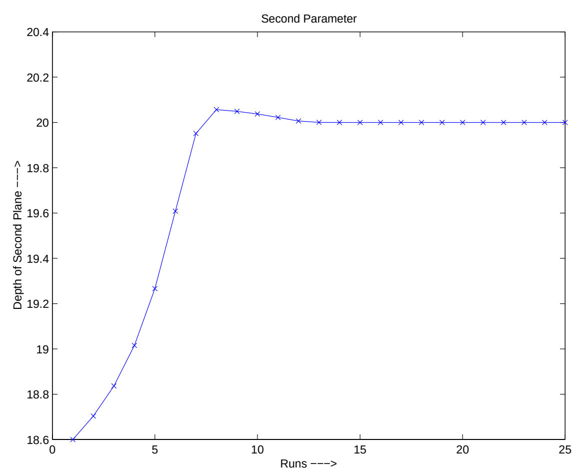

(c) Second Parameter, D_2

Figure 6.17: Levenberg-Marquardt Inversion

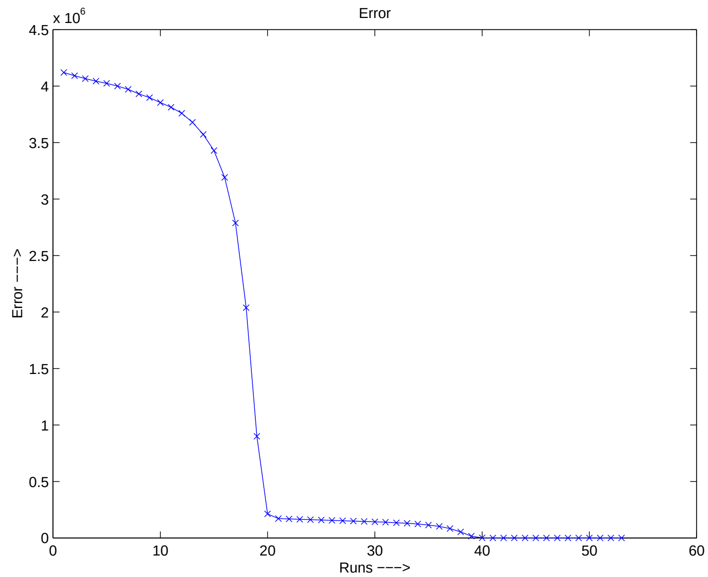

(a) Error Function Convergence

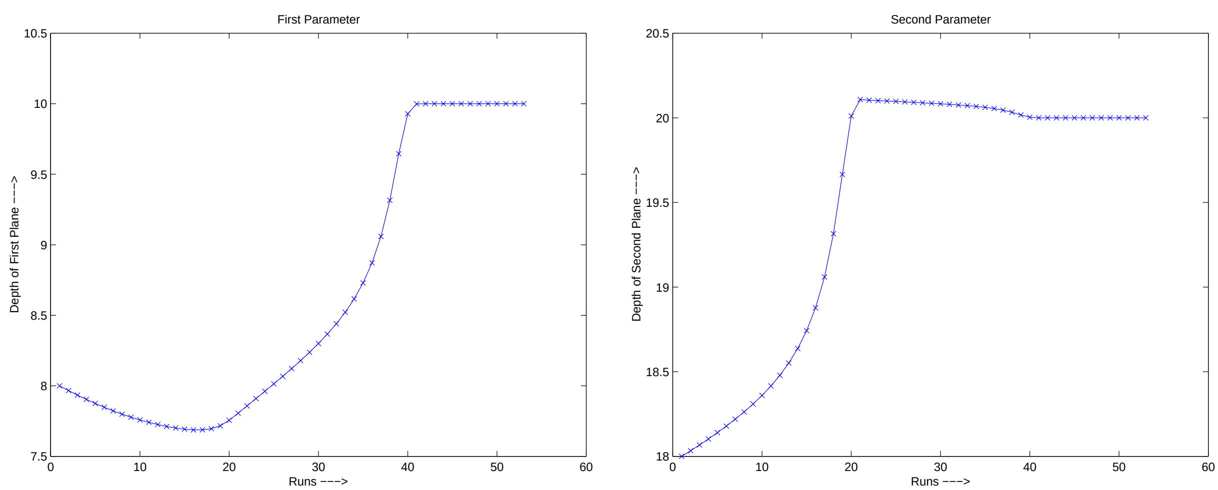

(b) First Parameter, D_1

(c) Second Parameter, D_2

Figure 6.18: Levenberg-Marquardt Inversion: Started from another point

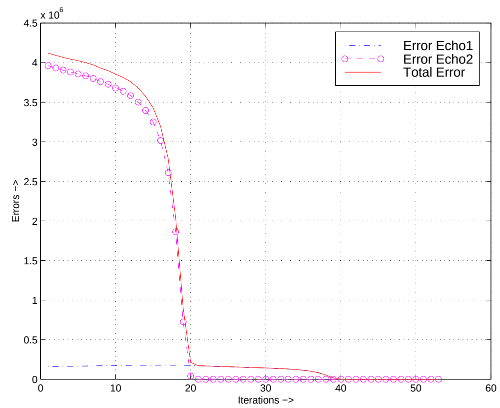

Error Function for Echo 1 and 2 and Total Error

Figure 6.19: Levenberg-Marquardt inversion started from another point

the plots, we show only the relevant iterations (from iteration 10 to 23) in Figure 6.20. In Figure 6.20 (b) we observe the error in the first echo increases as the depth parameter decreases in the first 17 iterations Figure 6.20 (d). But this does not result in an overall increase in the error. The decrease in error in the second echo due to increase in depth D_1 shown in Figure 6.20 (c) more than compensates for the error increase in the first echo. Hence the total error decreases. This is because of the relative magnitudes of the echoes.

The depth D_2 steadily increases (Figure 6.20(e)) and after the 17th iteration, the depth D_1 starts moving the right direction (increases) Figure 6.20(d). And the error in the first echo falls off as expected. From this point both errors fall off and convergence is achieved quickly, in three or four more iterations.

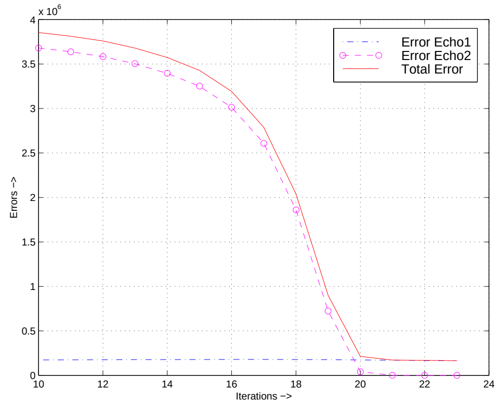

(a) Error Functions : Iterations 10 to 23

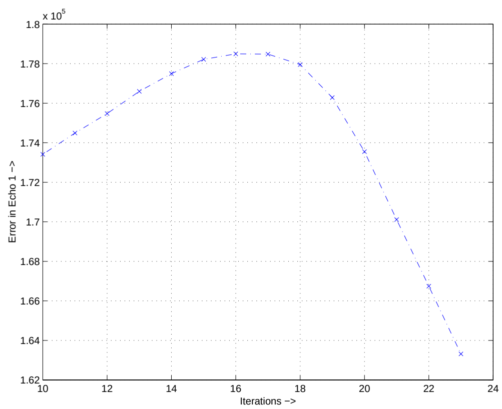

(b) Error Echo 1: Iterations 10 to 23

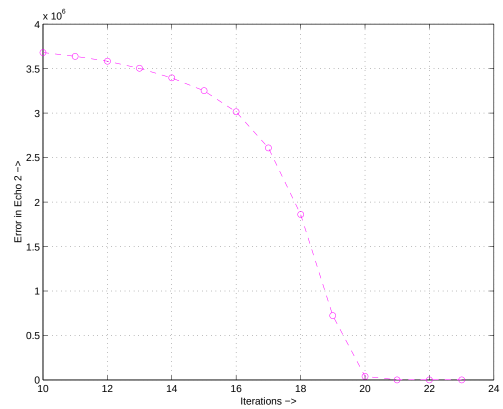

(c) Error Echo 2: Iterations 10 to 23

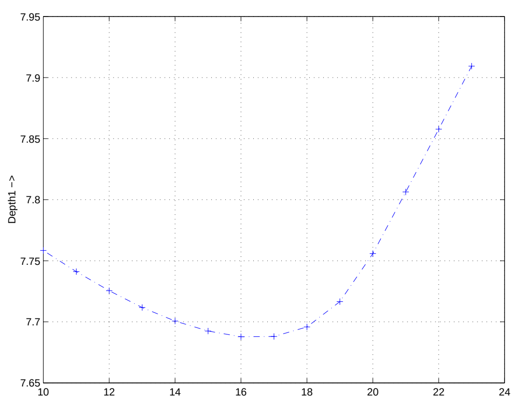

(d) First Parameter, D_1

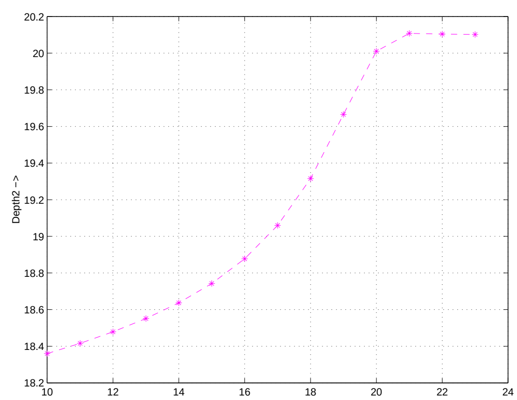

(e) Second Parameter, D_2

Figure 6.20: Errors and Parameters for Critical Runs

6.4 Conclusions

In this chapter we investigated the objective function we would like to minimize for a simple case of varying 2-parameters, the depths of the interfaces, kept parallel to the aperture. Even for this simple case we come across a few problems.

The first one is the oscillating local minima at regular intervals near the global minima. We solved this problem by demodulating the signals first. This effectively increases the error-bowl around the minima.

The second one is an overall declining trend in the error function with respect to one of the parameters. This factor is inherent in the problem and cannot be easily resolved, unless, from the slope it can be deduced if the minimization is in a shallow zone or is inside the error-bowl.

For the multi-parameter inversion, where we are interested in recovering the normals as well as the depths of various surface segments and possibly media parameters, velocity and densities we expect all these errors to appear. The first one can be resolved by demodulating the signal. However, there could be some inherent local minima like the second problem mentioned here. Another effect shown in this chapter, that of one parameter wandering away and then coming back is also likely to be present and in more complicated ways.

Considering all these factors, in order to use the Levenberg-Marquardt inversion, which is prone to local minima, we should start with a good initial guess so that we are inside the error bowl. The extent of the bowl in this two parameter case is of the order of the pulse width, which is fairly small and depends on the transducer parameters and its frequency response. However from the data-signal, it is not difficult to roughly guess the locations of the pulses. A good initial guess is easily obtained if we do a simple thresholding on the demodulated data. With the estimated parameters, we can start the inversion at those locations and hopefully be inside the "bowl" and converge quickly to the global minima.

Chapter 7

Results of the Inversion of the Model on Experimental Data

In chapter 5, we showed the results of some experiments on tissue mimicking phantoms. The experimental procedure is given in details in that chapter and not repeated here.

In this chapter we describe iterative inversion for the forward model for the real experimental case. The goal of the inversion is to obtain the "best" match with the simulation output and the experimental data in the minimum least square error sense.

7.1 Iterative Inversion

The objective function we minimize is the error between the experimental data and a scaled version of the simulation. The experimental "data" signal is the input to the inversion loop in Figure 7.1.

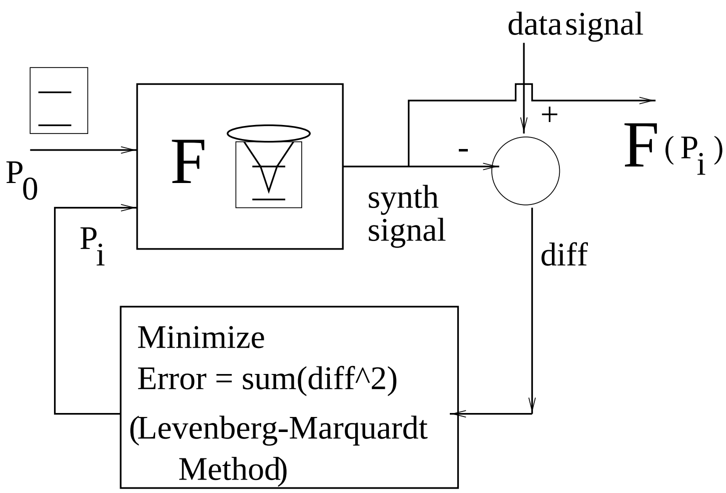

Figure 7.1: Iterative Inversion

The full experimental data is shown here again in Figure 7.2. We show the close-ups of the first and second echo in Figure 7.3. Before using this signal, we remove the first big echo and replace it by a segment of the signal consisting of just the noise.

7.2 The Problem of Scale Factor

As explained in chapter 5, we are able to obtain the transducer pulse to within a scale. Hence there is an unknown scale factor for the simulated data.

The objective function minimized now is

Experiment

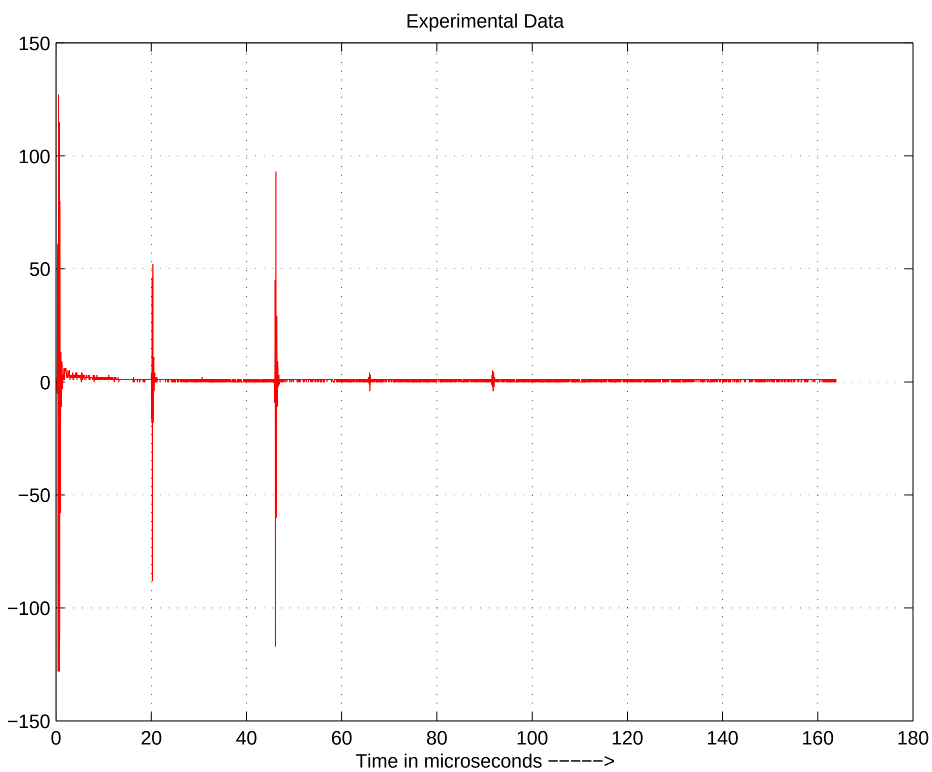

Figure 7.2: **Experiment: Full Signal**

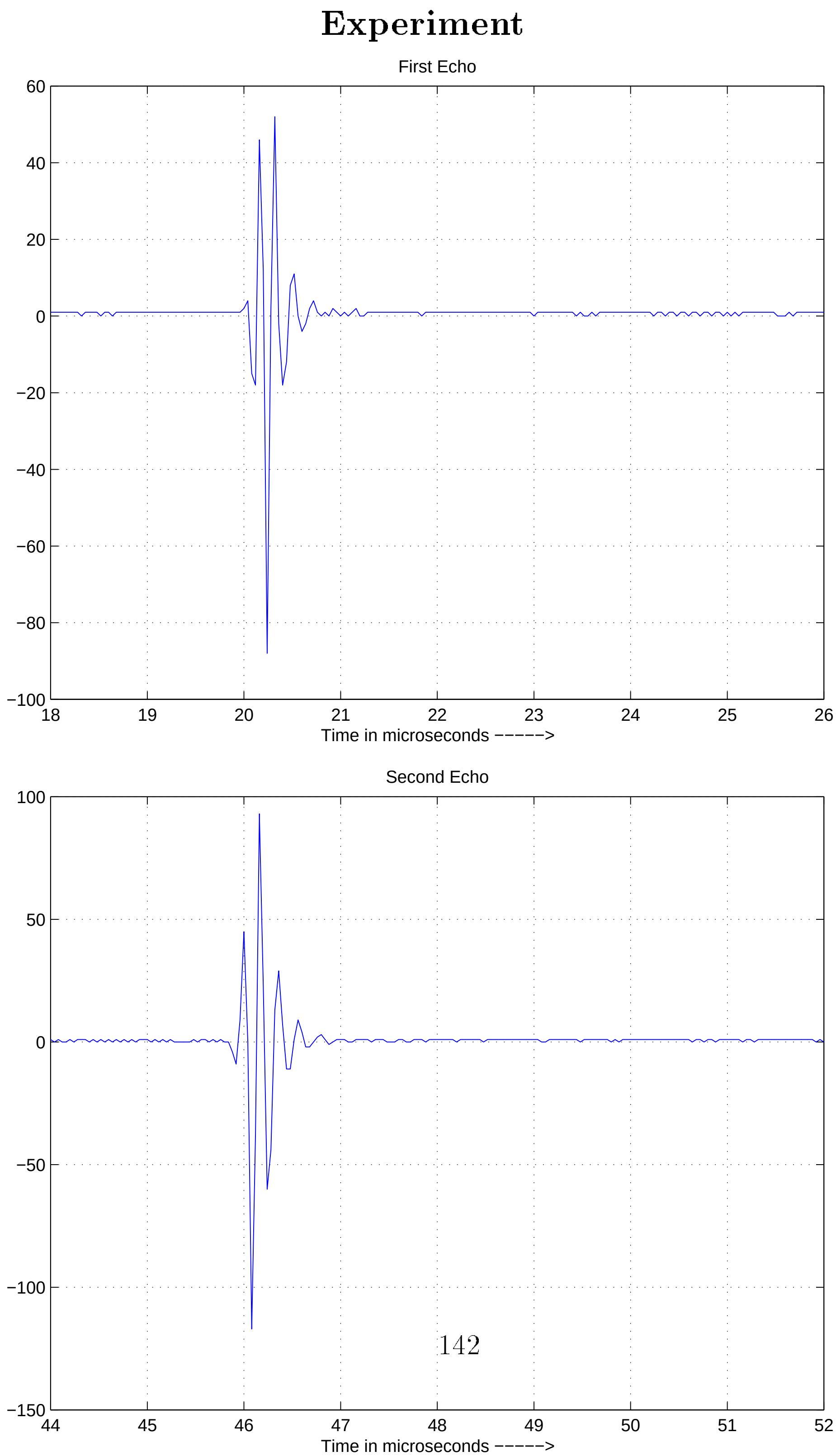

Figure 7.3: **Experiment: Individual Echoes**

$$E(\mathbf{p}) = \sum_n (y_n - Ay(n;\mathbf{p}))^2 \tag{7.1}$$

where A is the unknown scale factor.

Ideally we should add A to the list of parameters.

However, in the present analysis we obtain a rough estimate of the scale factor ahead of time. This estimate is the relative ratio of the energies of the experimental data and the simulated output at the initial guess.

We assume that this estimate is close to the final "correct" scale and would not affect the convergence of the other parameters, D_1 and D_2 in this case.

Once we obtain a good estimate of the parameters $\mathbf{p}$, we can correct for the scale factor in the following way. At the correct parameters, p_c, the energy is given by

$$E(\mathbf{p}) = \sum_n (y_n - Ay(n;\mathbf{p_c}))^2 \tag{7.2}$$

The right scale at which this error is minimum, can be analytically calculated by setting the derivative of $E(\mathbf{p})$ with respect to A to zero. We obtain the "correct" A as

$$A_c = \frac{\sum_n y_n y(n;\mathbf{p_c})}{\sum_n y^2(n;\mathbf{p_c})} \tag{7.3}$$

7.3 Levenberg-Marquardt Inversion Results for Experimental Data

The manufacturer specified value for the phantom thicknesses were $15mm$ and $20mm$, valid to within $1mm$ of manufacturing error. In Chapter 5 we ran a simulation with parameters at the manufacture specified nominal values ($D_1 = 15$ and $D_2 = 15 + 20 = 35$) and scale the simulation data so that the over-all energy of the data and the simulation signals are the same. We saw that the simulations at the manufacturer specified values nominal values of depths do not match very well. There are mismatches in the locations of the echoes (Figure 5.6 to 5.8).

Each forward loop takes around 45 minutes to run on an SGI Onyx. Hence we started with a good guess of the initial parameters.

We start with an initial guess of the parameters closer than $D_1 = 15$, $D_2 = 35$. The goal of the inversion is to see at which parameter values of the simulation the signal matches the experiments best (in a mean-squared sense).

In the last chapter we showed that using the raw modulated signals could lead to falling into a local minimum (unless we are within $\lambda/2$ of the global minimum). Hence we start the inversion with the demodulated signals. For the final fine-tuning we relax the demodulation: we use the final parameters from the output from the demodulation set and perform the inversion again with the modulated signals to get the very final convergence.

In the next section we show the results of the convergence and the final parameter values for the inversion with demodulated signals. We compare the experimental and the simulated output.

In the section after that, we relax the demodulation and run a few iterations and show the final parameters and the simulation results with those parameters.

7.3.1 Results of Inversion With Demodulated Signals

The manufacturer specified value for the phantom thicknesses were $15mm$ and $20mm$, valid to within 1 mm of manufacturing error. The initial parameters should be near $D_1 = 15$ and $D_2 = 35$. From a rough estimate of the location of the echoes from the experimental "data" signal, we start the iteration at $D_1 = 15.0$ and $D_2 = 35.3$.

Figure 7.4 shows the convergence of the error function and the two parameters.

The starting and final errors and converged parameters are given in Table 7.1.

Table 7.1: **Convergence Data: Using Demodulated Signals**

	Start	End
Error	45306	6203
Depth D_1	15.0000mm	14.9568mm
Depth D_2	35.3000mm	35.4342mm

We plot the experimental data and the scaled simulator output for the

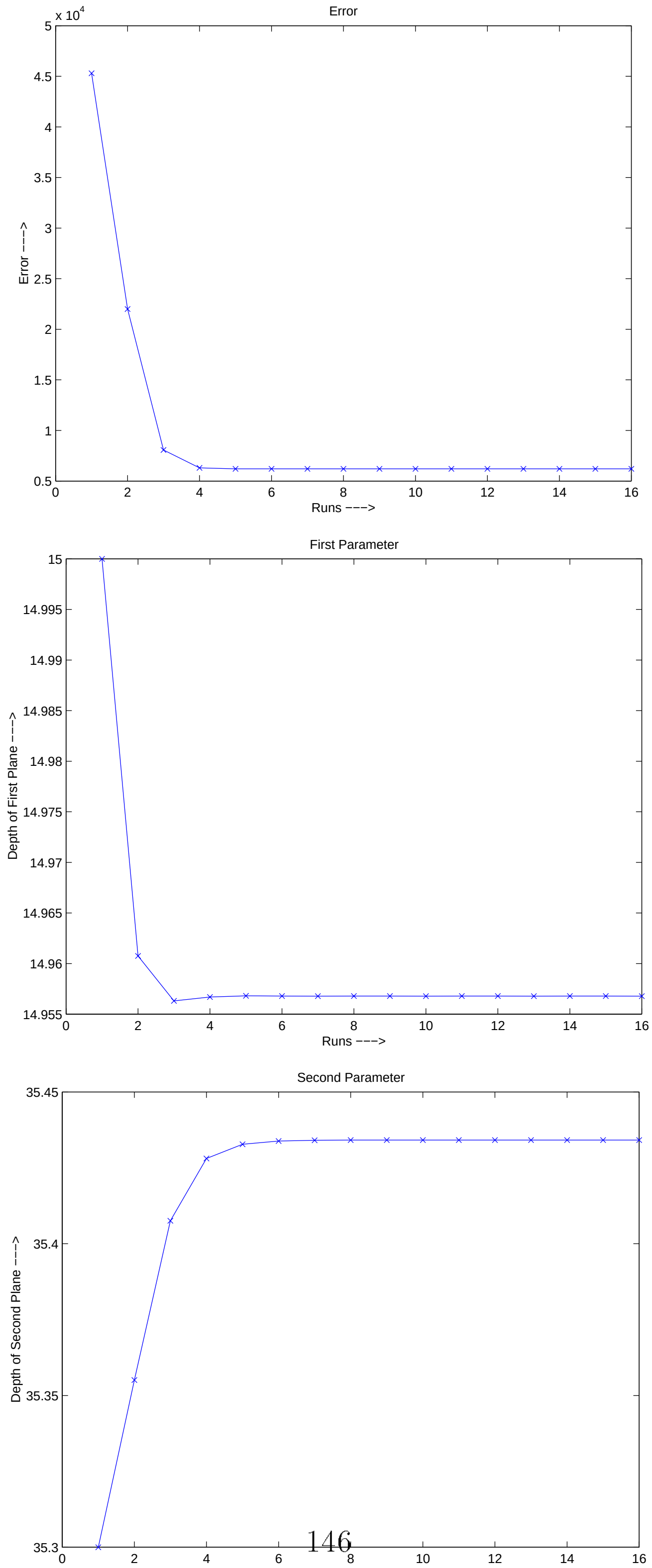

Figure 7.4: Convergence of Error and Parameters for demodulated signals

final converged parameters in Figure 7.5. The close ups of the echoes are given in Figures 7.6 and 7.7.

We notice that the first echo seems to be slightly out of phase in Figure 7.6. This effect is guessed to be due to using the envelope of the signals for the error minimization rather than the signals themselves.

Hence the next obvious step is to relax the demodulation and run the inversion on the raw data and raw simulated signals. The starting parameters for these set of iterations (using the raw signals) is the end parameters arrived at using the demodulated signals.

7.3.2 Results : Final Convergence with Modulated Signals

We show the convergence of the errors and and the parameters in Figure 7.8.

The start/end error and parameter values are in Table 7.2. (The starting parameters are the end-results in Table 7.1).

Table 7.2: **Final Convergence Data**

	Start	End
Error	32651	12702
Depth D_1	14.9568	14.9727
Depth D_2	35.4342	35.4220

We observe that for the same parameters, the starting error is much larger

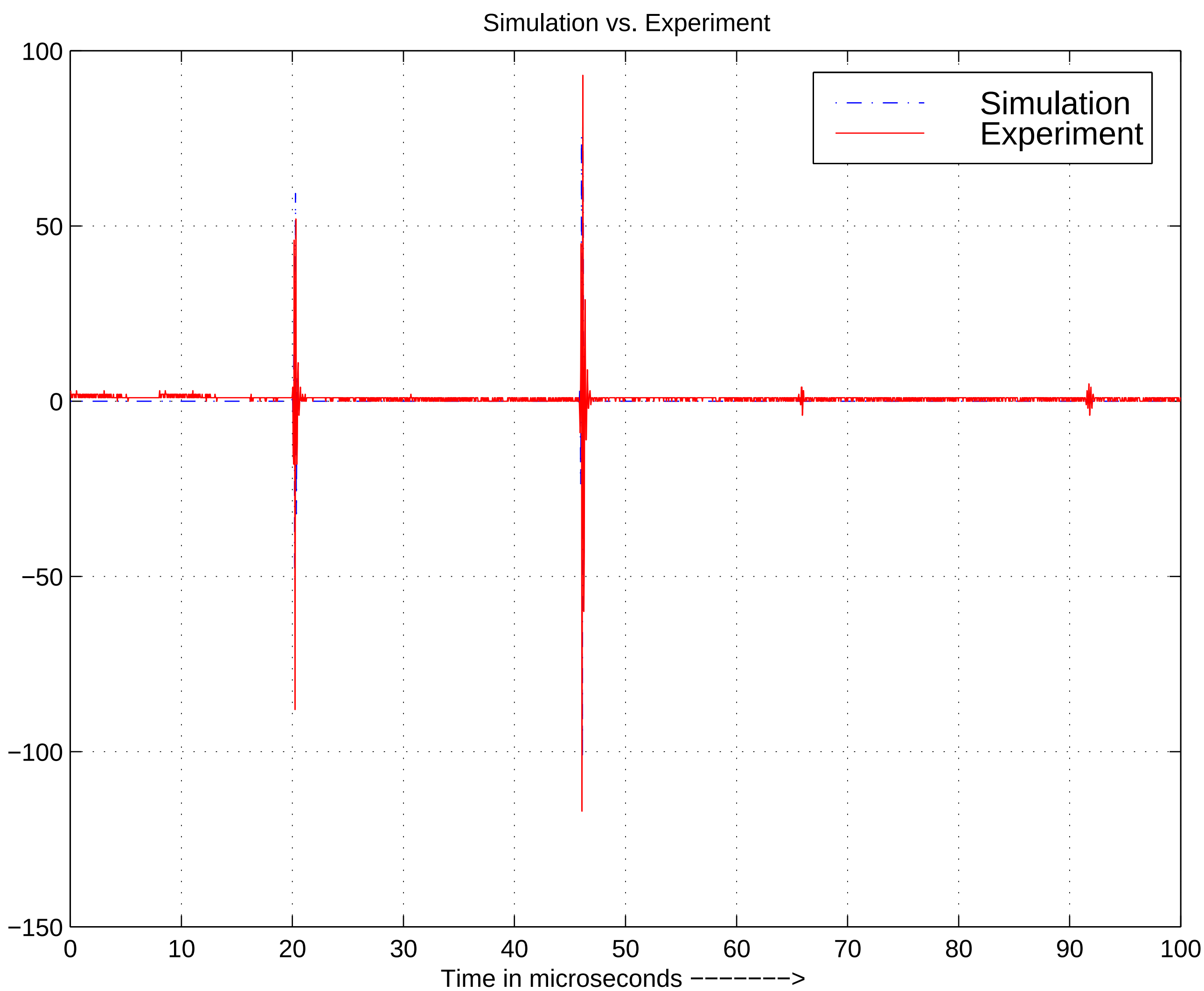

Figure 7.5: Results using demodulated signals

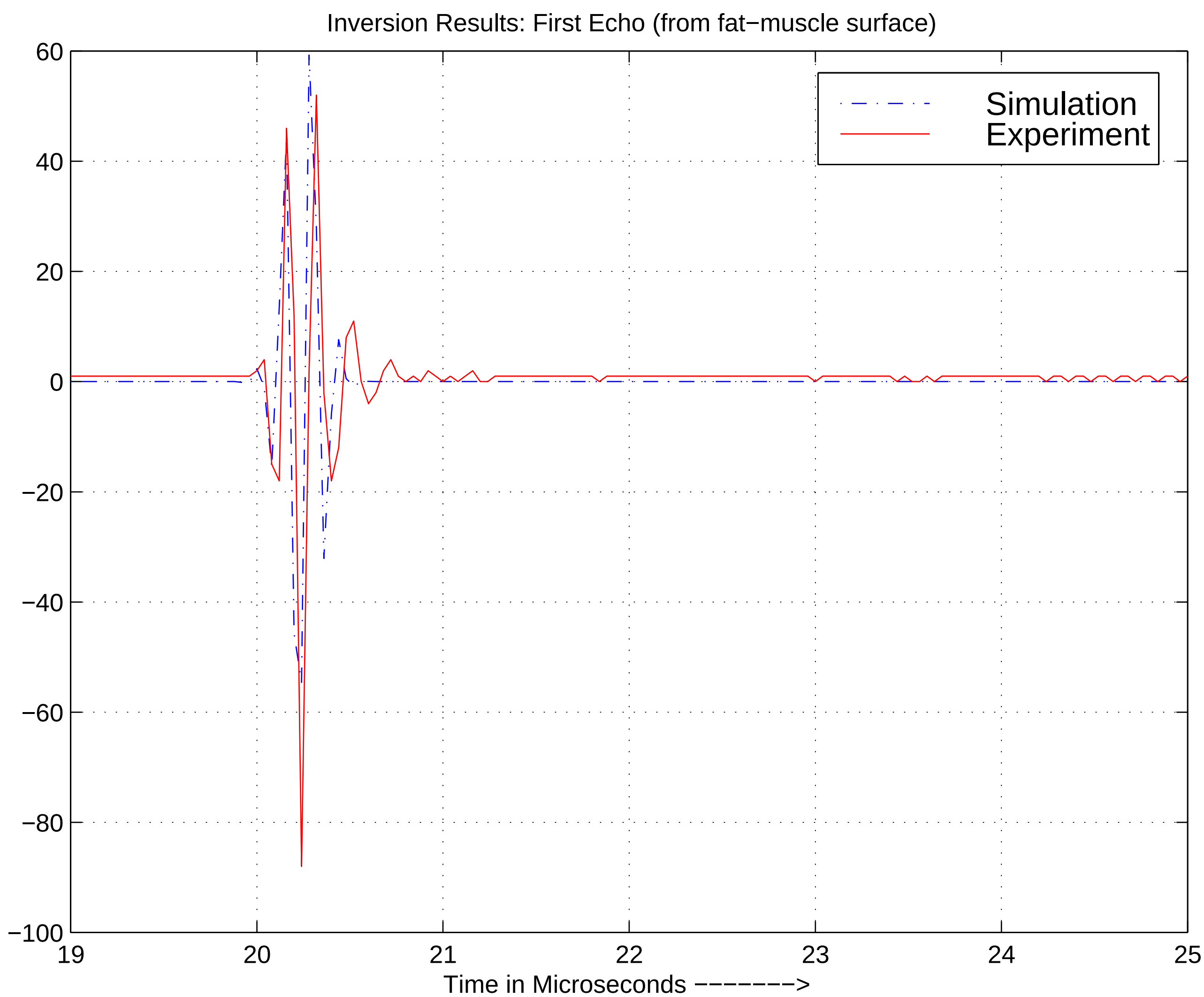

Figure 7.6: Results using demodulated signals: close-up of Echo1

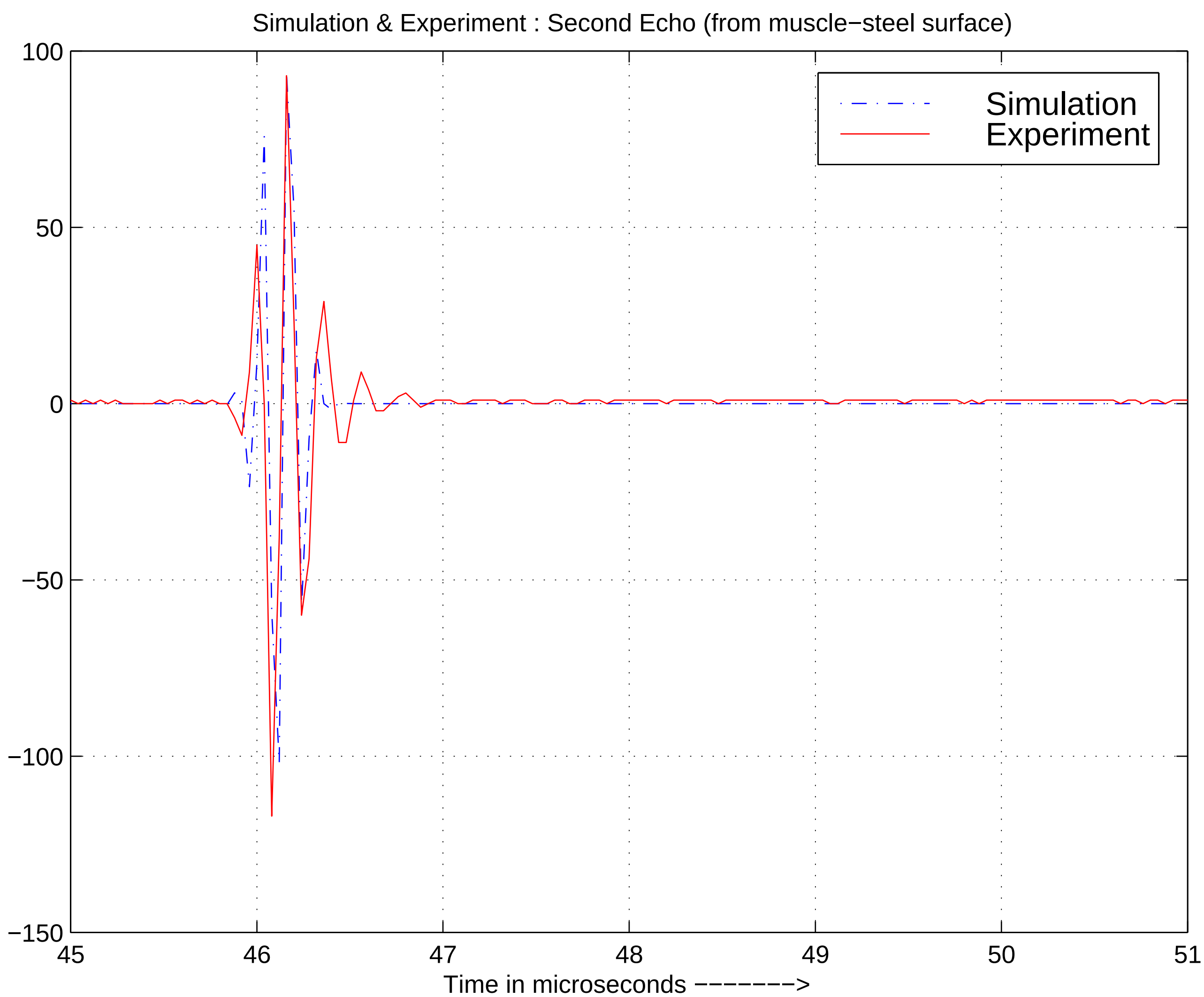

Figure 7.7: Results using demodulated signals: close-up of Echo2

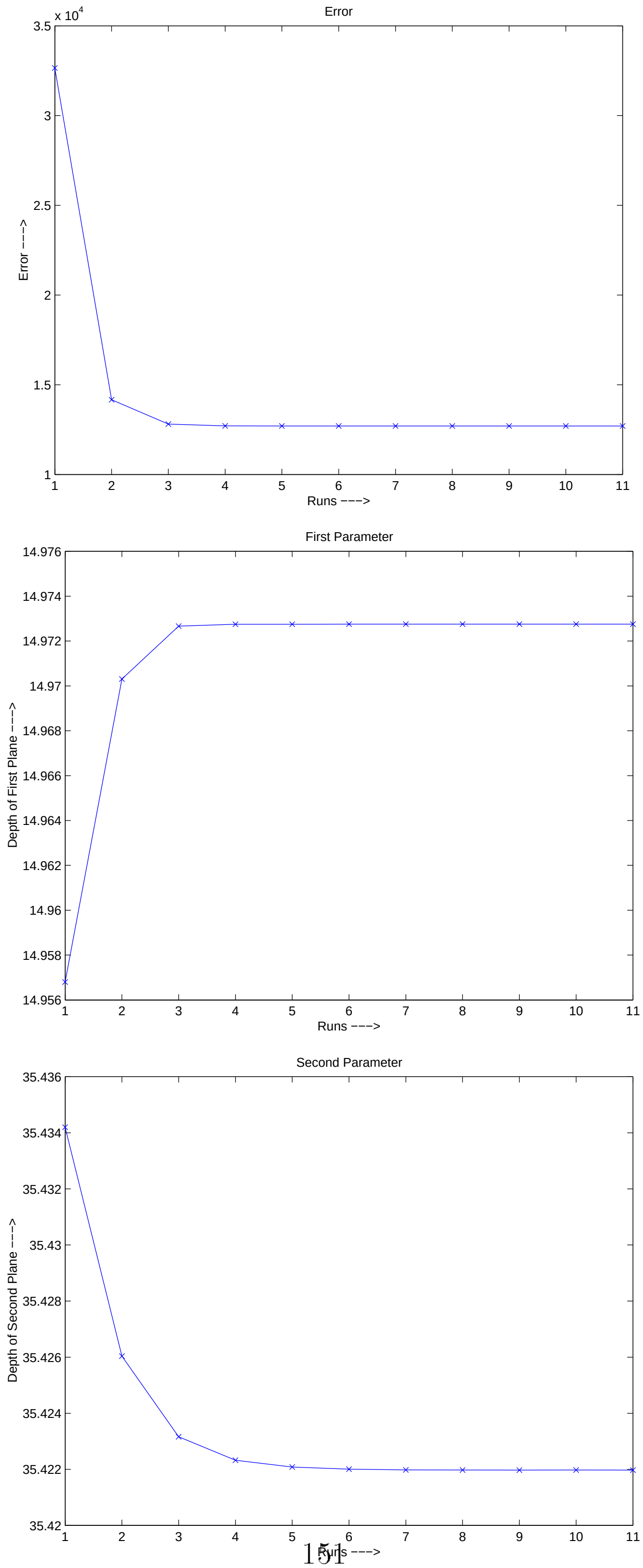

Figure 7.8: Convergence of Error and Parameters for modulated signals

for the modulated case than when we consider the demodulated case in Table 7.1. And the final error is higher than what we obtained at the end of the runs for the demodulated case. But this is not an unexpected result. Matching of envelopes is a different criterion than matching of the signals themselves. And the signals themselves seem to have matched satisfactorily, as shown in Figure 7.9 to 7.11. Figures 7.10 and 7.11 gives the close-up of the echoes.

The various magnitude ratios of the echoes themselves and the normalized RMS error are given in Table 7.3.

Table 7.3: **Magnitude Comparisons: Final parameters of inversion with raw signals**

Comparison with Experiment and Simulation	
[RMS Experiment Echo1]/[RMS Simulation Echo1]	1.0353
[RMS Experiment Echo2]/[RMS Simulation Echo2]	0.9564
[RMS Echo1]/[RMS Echo2] - simulation	0.5987
[RMS Echo1]/[RMS Echo2] - experimental	0.6481
Normalized MS Difference	0.2553

As mentioned in Chapter 5, the first entry is the ratio of RMS amplitude ratio of the experimental first echo to that of the first echo of the fitted model. We see in a root mean-squared sense the match is 1.0353 (or 0.1507 db). Ideally this should be close to unity.

The second entry is the ratio of RMS amplitude ratio of the second echo, experimental to simulation. In this case the the match is -0.1936 db.

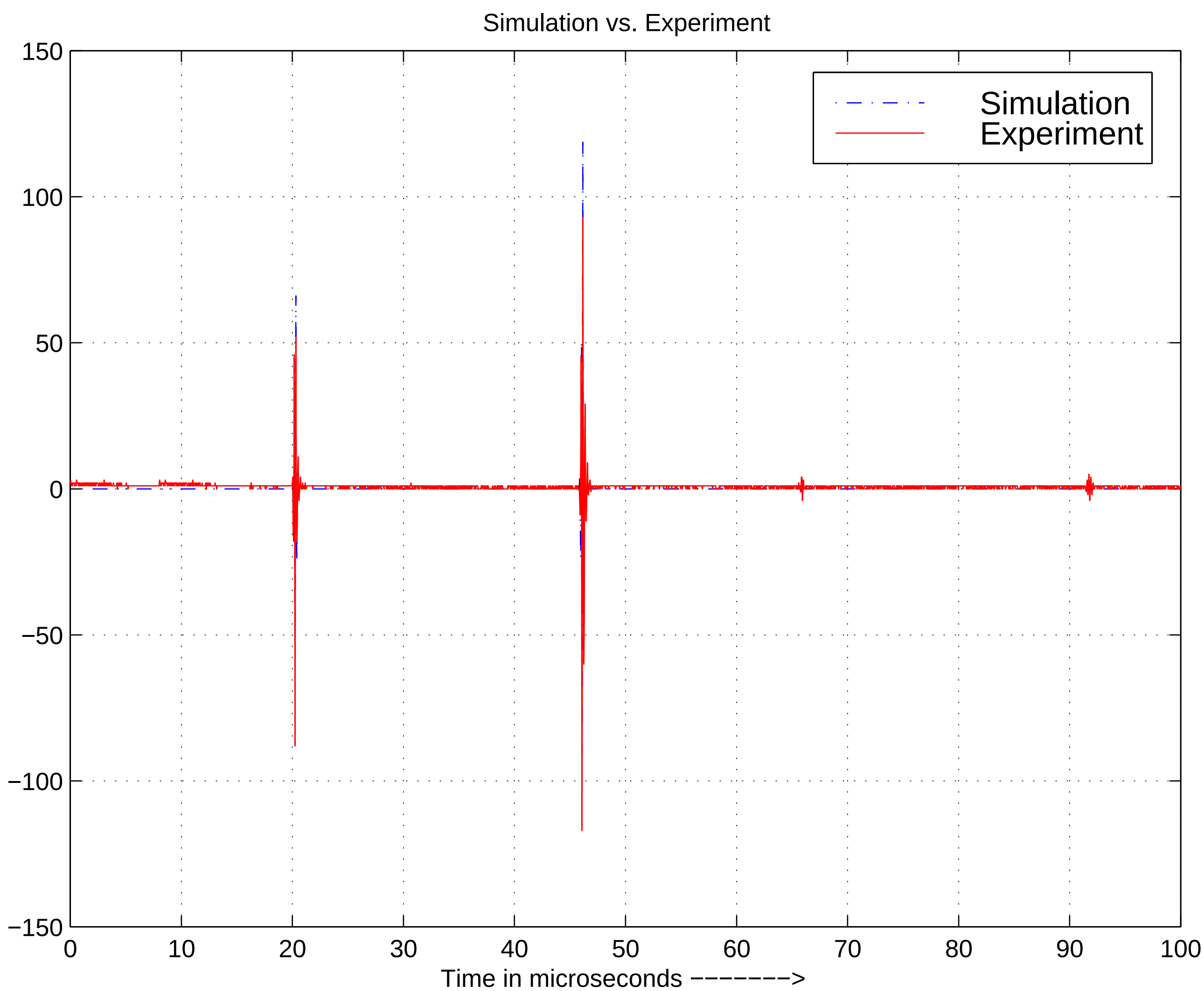

Figure 7.9: Results using modulated signals

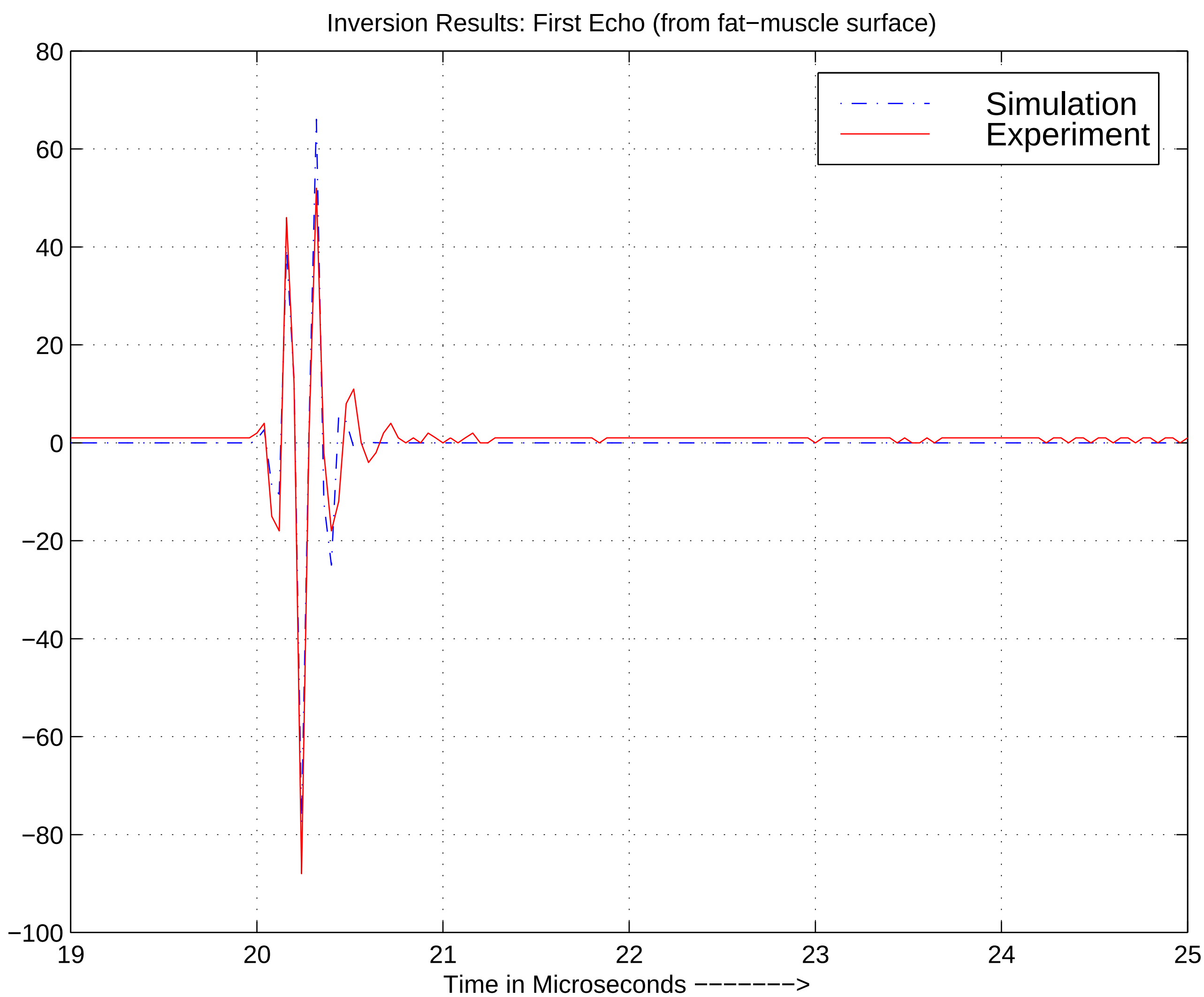

Figure 7.10: Results using modulated signals: close-up of Echo1

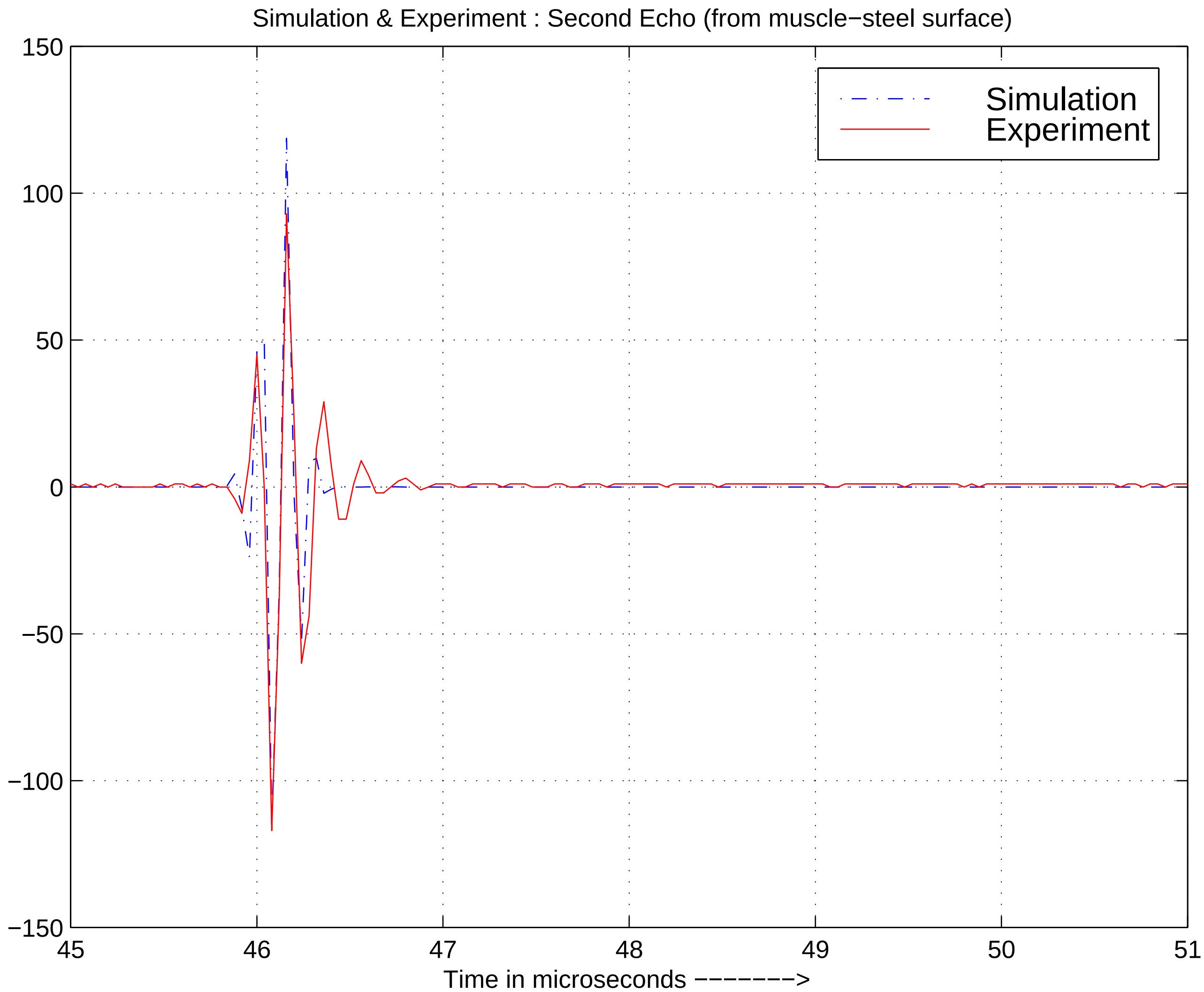

Figure 7.11: Results using modulated signals: close-up of Echo2

The next two entries shows the relative RMS amplitude between the first echo and the second echo for the simulation data and the experimental data respectively. Ideally these ratios should be the same.

The last entry is the root-mean-square of the difference normalized by the energy of the experimental data) shows that the difference in the signals are within 25.53%.

The final converged values are $D_1 = 14.9727mm$ and $D_2 = 35.4220mm$. This indicates that the thicknesses of the two layers are $14.9727mm$ and $20.4493mm$, which are within the manufacturing tolerance of the two layers.

7.3.3 Final Results : After scale correction

As a last step we do the scale correction as explained in Section 7.2 and as prescribed by Equation 7.3.

The original scale was $A = 4.4904$. After the correction, the scale is $A_c = 3.9139$.

The correctly-scaled simulation and the experiments are compared in Figures 7.12 and in Figure 7.13.

We tabulate the amplitude rations results again in Table 7.4. After the scale correction, the normalized MS-error improved by 1.65%. All the other entries, being ratios, remained the same as in Table 7.3

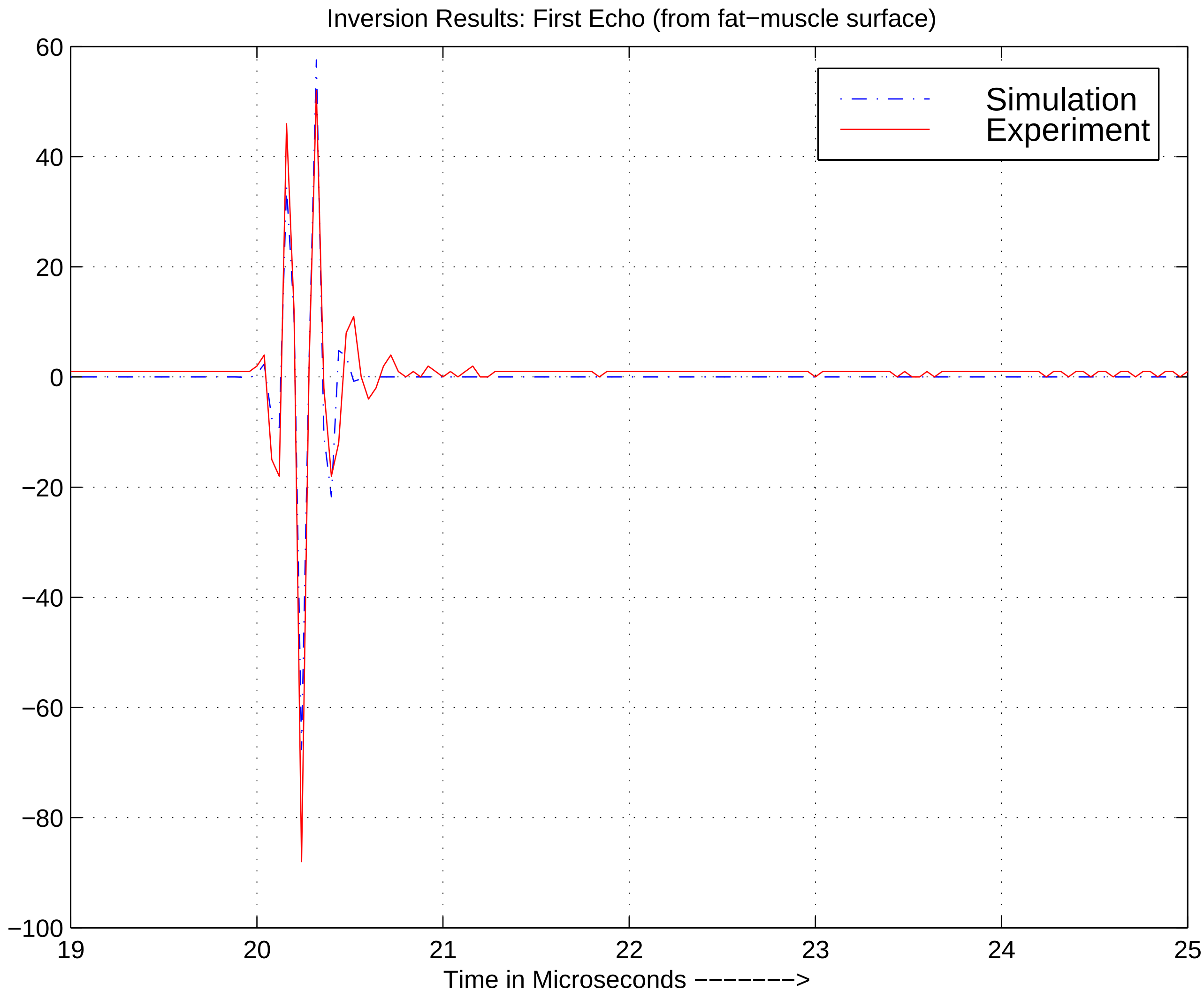

Figure 7.12: Results using modulated signals, after using scale correction: close-up of Echo1

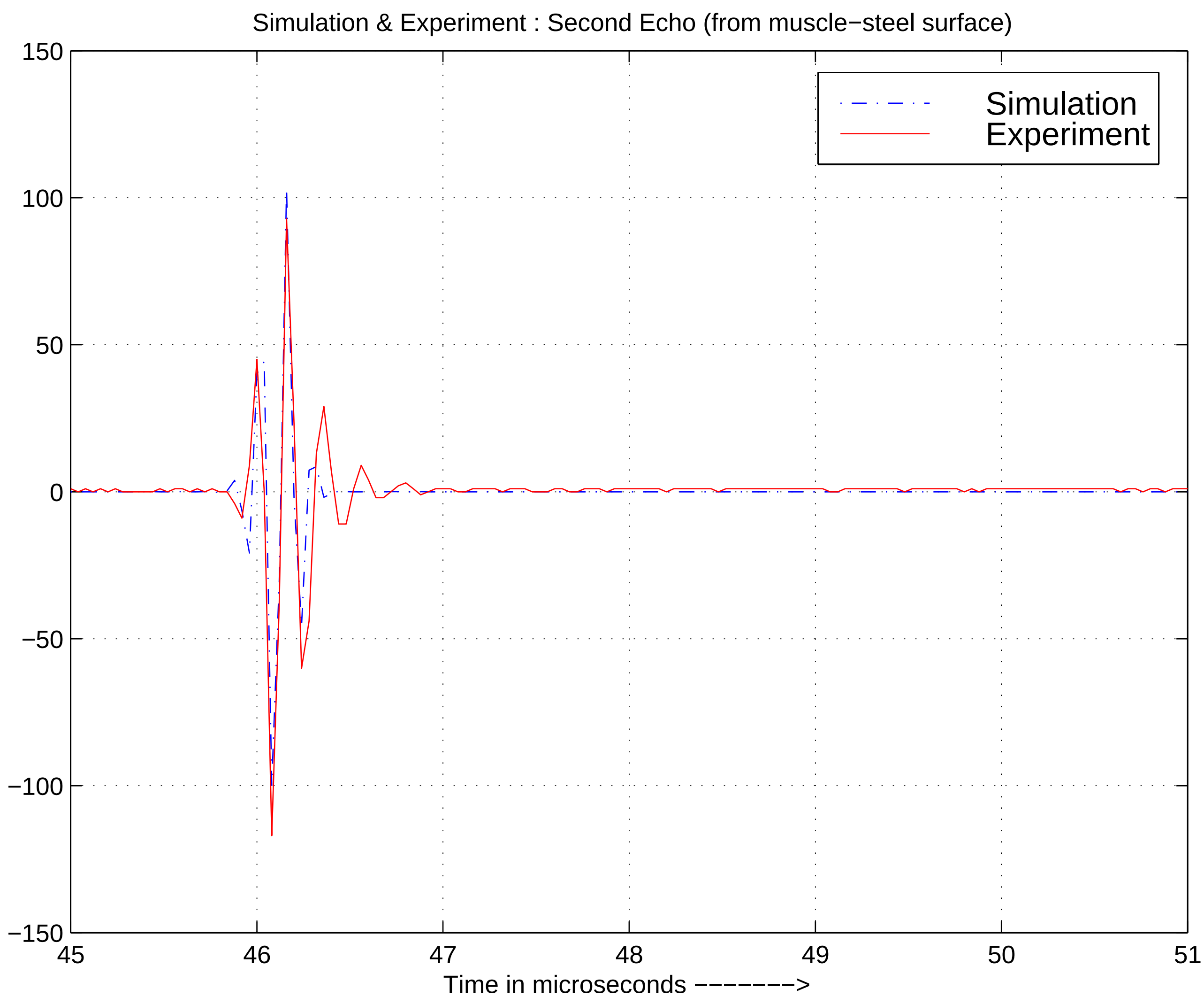

Figure 7.13: Results using modulated signals, after using scale correction: close-up of Echo2

Table 7.4: **Ratios after Scale Correction**

Relative Amplitudes and MS difference	
[RMS Experiment Echo1]/[RMS Simulation Echo1]	1.0353
[RMS Experiment Echo2]/[RMS Simulation Echo2]	0.9564
[RMS Echo1]/[RMS Echo2] - simulation	0.5987
[RMS Echo1]/[RMS Echo2] - experimental	0.6481
Normalized MS Difference	0.2388

7.4 Discussions of Results

Figures 7.12-7.13 show fairly good qualitative match between experiments and simulations. Both the echoes matched well in the central oscillations. The discrepancy is more towards the end and is mainly due to pulse mismatch.

To investigate this further, we plot the difference signal, superposed on the experimental signal in Figures 7.14 and 7.15

We observe that the difference is rather high and almost of a constant amplitude. As point-to-point fractions of the experimental signal, it is more in the outskirts of the signal and much lesser near the center of the signal.

One reason the high error could be partially because a small error in the estimated "correct" parameters (the depths) result in large error in the signal differences because of the signal modulation. We feel that the difference signal for the demodulated versions of the signal would have better a criterion.

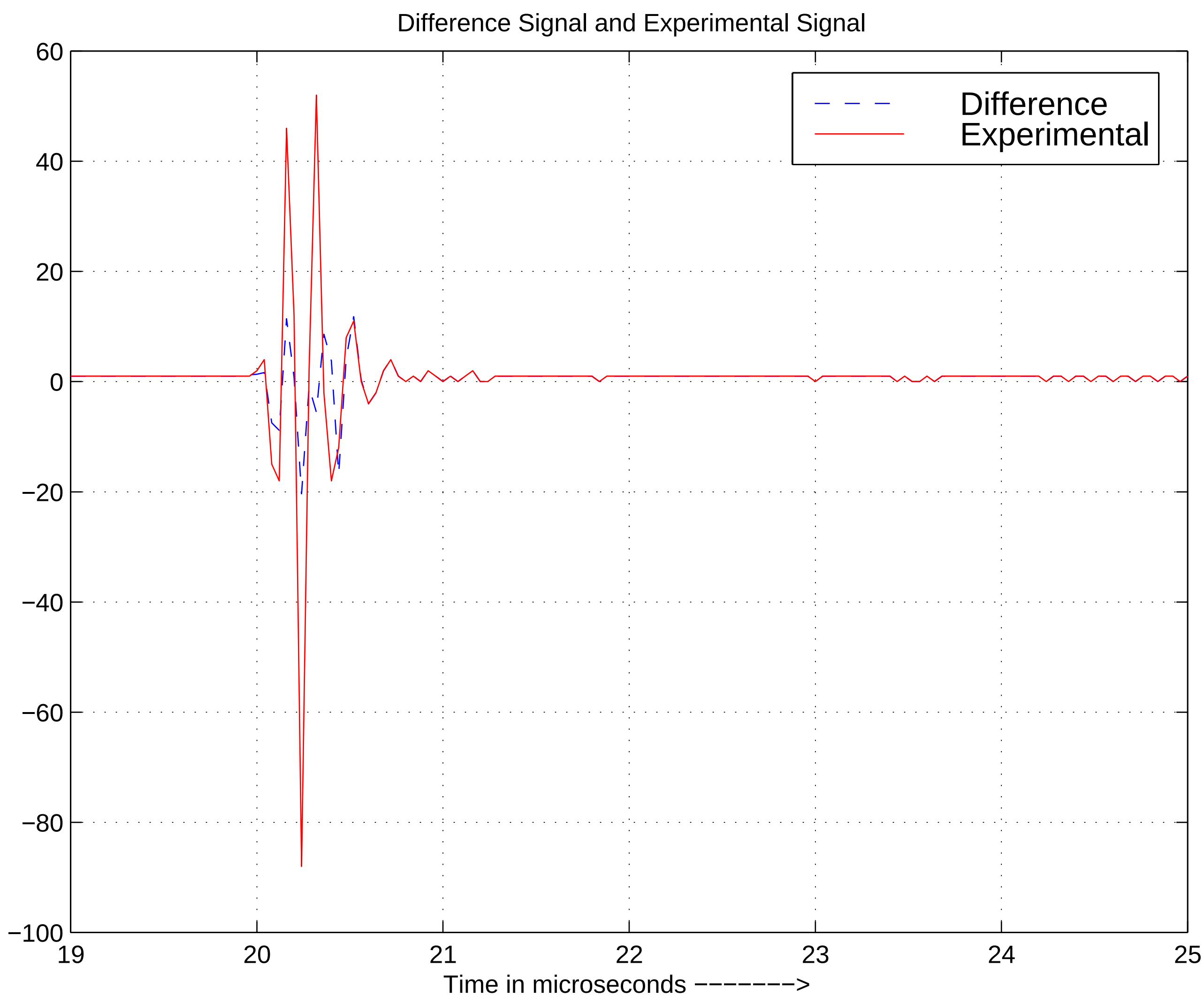

Figure 7.14: Difference and Experimental Signals : Echo1

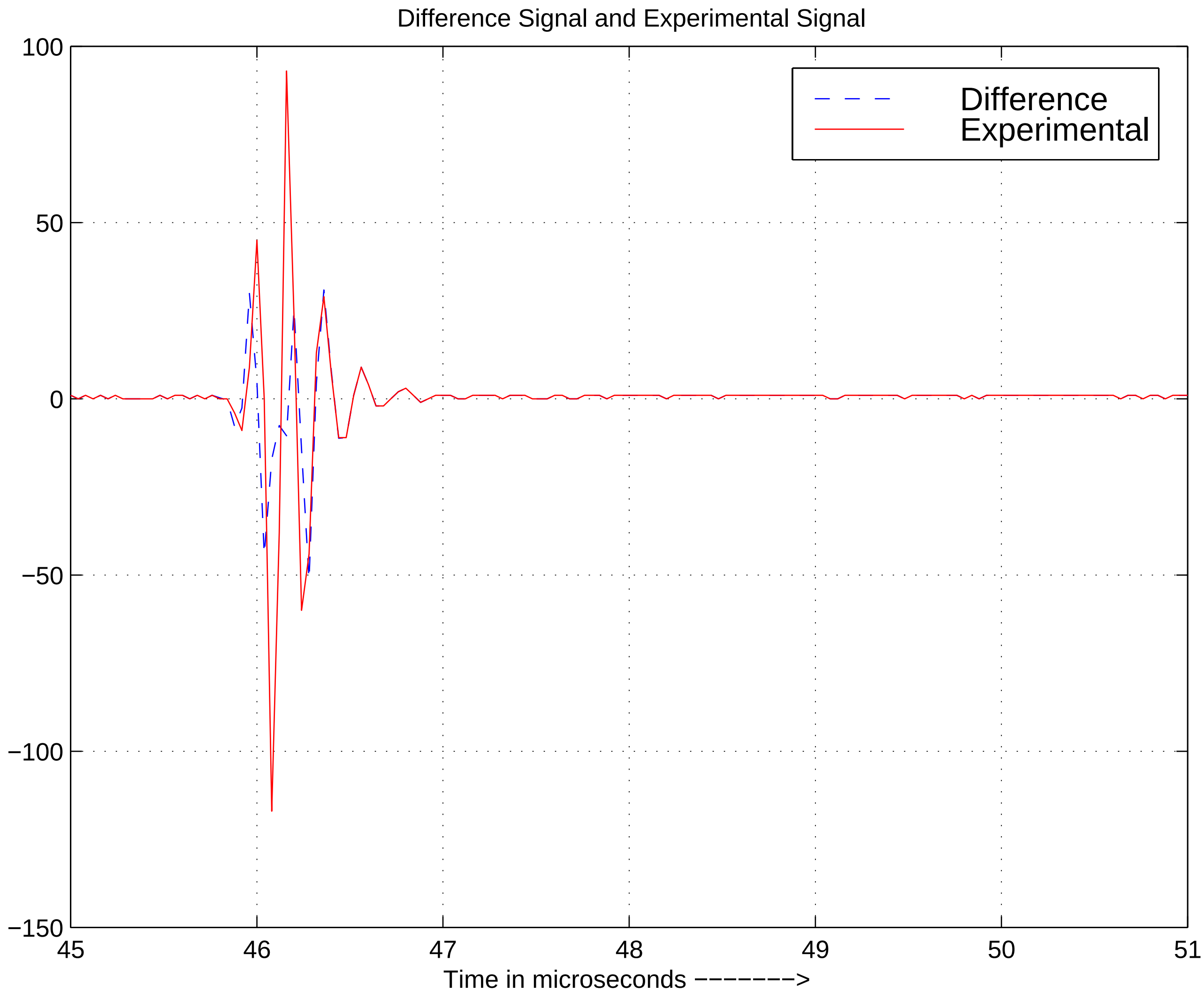

Figure 7.15: Difference and Experimental Signals : Echo2

We check the differences of the demodulated versions of simulation and the experiment echoes, shown in Figures 7.16 and 7.17.

We put the ratio numbers in Table 7.5. We see the normalized MS-error reduced to 13.81% of total energy. The MS-error for the first echo is 8.00% of its own energy. That for the second echo is only 8.03% of its own energy.

Table 7.5: **Error Ratios: After Convergence and Scale Correction**

Comparisons of MS Difference	
Normalized MS Difference: Modulated signal	0.2388
Normalized MS Difference: Demodulated signal	0.1381
NMS Difference: Echo 1 (Demodulated)	0.0800
NMS Difference: Echo 2 (Demodulated)	0.0803

It is mentioned again that for the last two entries the respective normalization is done with respect to the echo signals' respective energies. Hence we give a different notation (NMS) to these than the first two entries (where the normalization is by the entire data signal's energy).

We summarize the important nos. in the Table 7.6

7.5 Conclusions

The simulations with the final parameters of inversion show fairly good qualitative matches with the experimental data. The first and second echo RMS amplitudes matched to 1.0353 (or $0.1507db$) and 0.9564 (or $-0.1936db$) re-

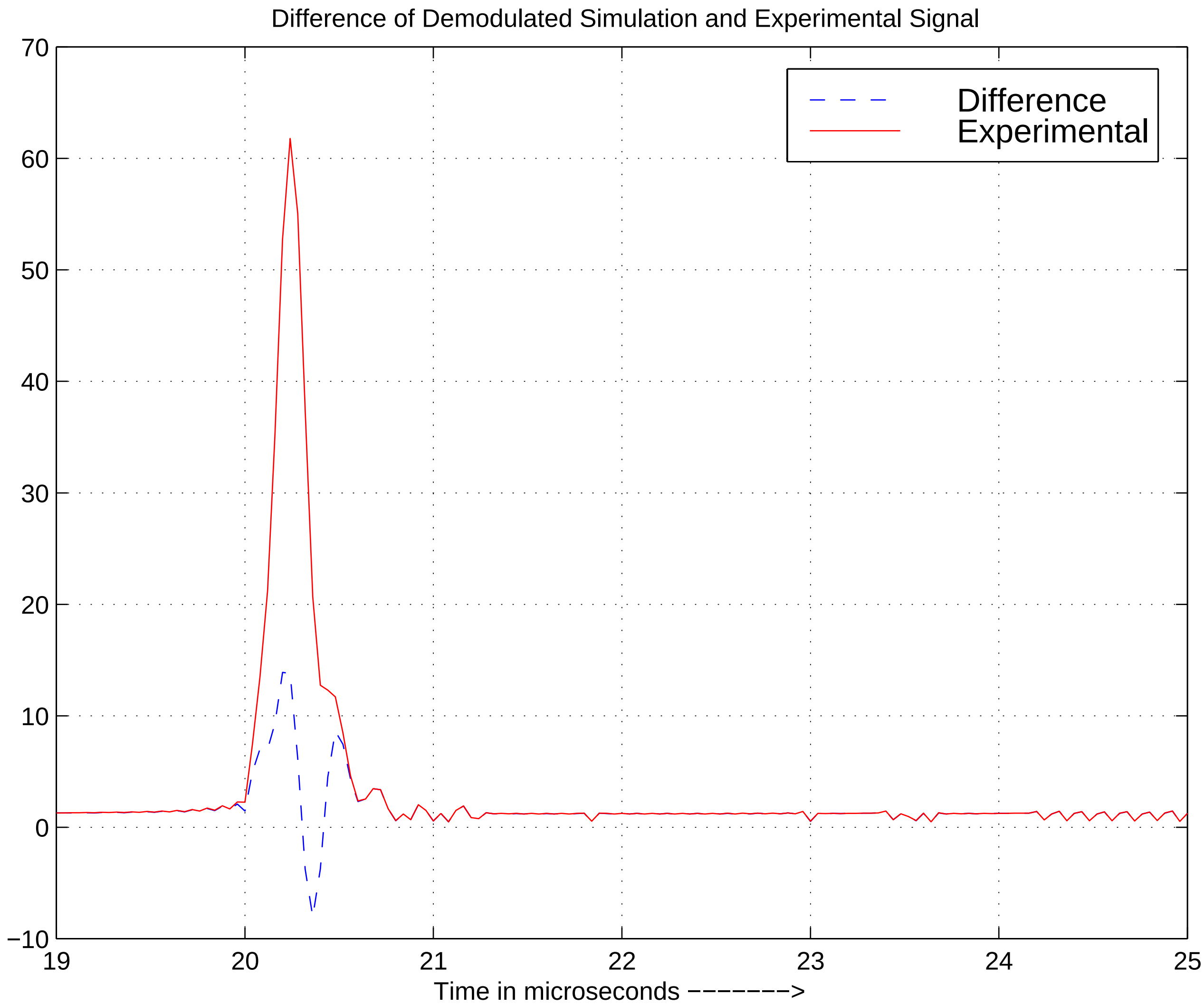

Figure 7.16: Difference of Demodulated Signals: Echo 1

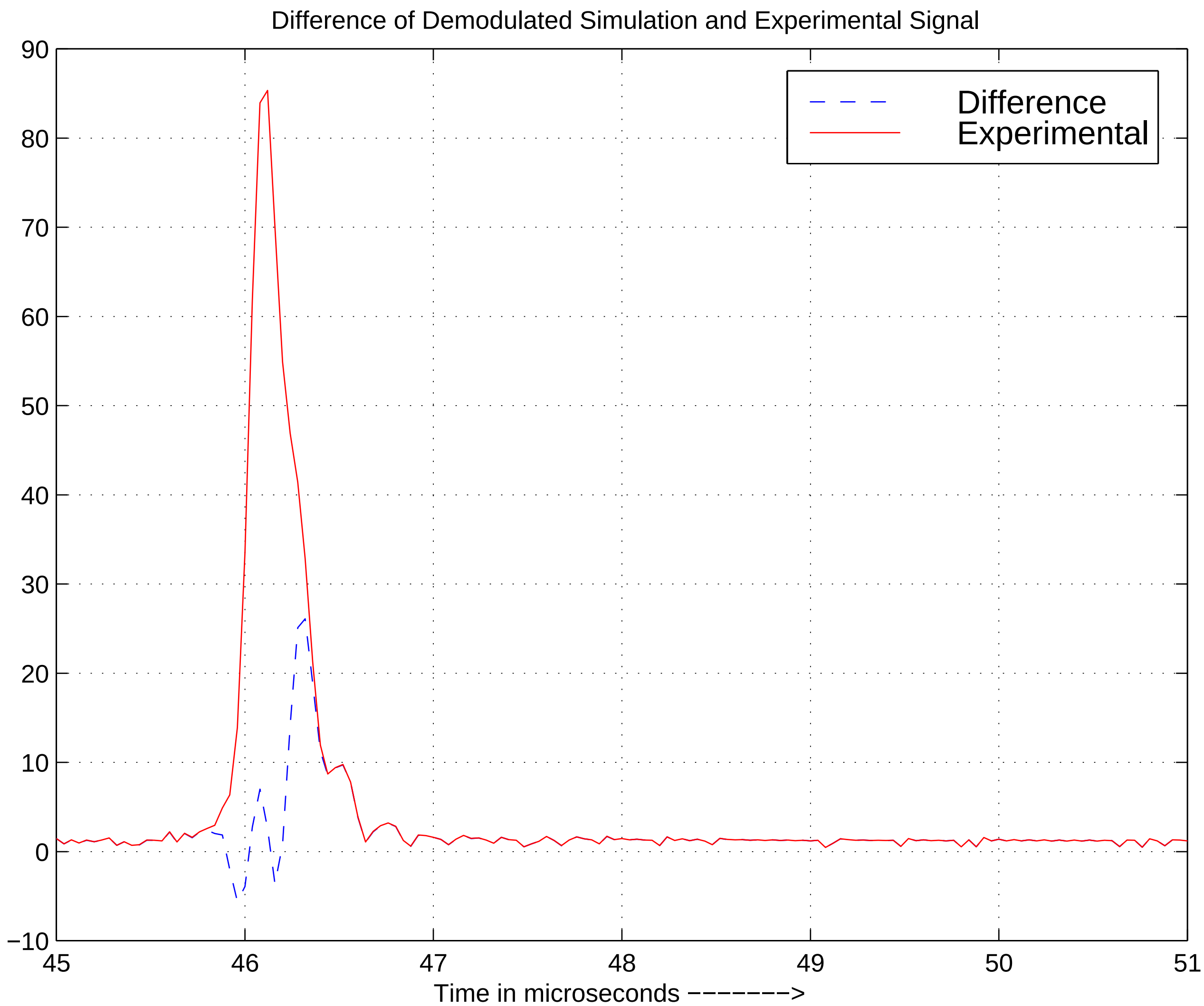

Figure 7.17: Difference of Demodulated Signals: Echo 2

Table 7.6: **Amplitude, Error Ratios and Final Parameters**

Relative Amplitudes and MS Difference	
[RMS Experiment Echo1]/[RMS Simulation Echo1]	1.0353
[RMS Experiment Echo2]/[RMS Simulation Echo2]	0.9564
Normalized MS Difference: Modulated signal	0.2388
Normalized MS Difference: Demodulated signal	0.1381
NMS Difference: Echo 1 (Demodulated)	0.0800
NMS Difference: Echo 2 (Demodulated)	0.0803
Final Parameter D_1	14.9727mm
Final Parameter D_2	35.4220mm

spectively. The means-square error of the envelope signals was 13.81% of the original (envelope) signal energy.

The final inversion parameter results are close to the values specified by the manufacturer and within the tolerance limit.

The reasons for the residual errors in the experimental and simulation could be, partly due to limits of the model and partly due to the inversion procedure. We give some of the possible reasons below.

- Forward Model
  - There is an initial shape mismatch with the transducer pulse and the fitted gaussian in Figure 5.5. Qualitatively, the residual shape mismatches of the echoes are believed to be largely due to this

mismatch in the emitted pulse and the fitted gaussian.

- There is a frequency-dependence of the attenuation coefficient. In the simulation we used the attenuation at the center-frequency. For the first layer, which was more like water, this variation may not be linear. For water this variation is f^2. But, this was expected to be not a severe problem because the attenuation coefficient itself was small for this case. For the second echo in Figure 7.13, we do observe pulse distortion and difference in the zero-crossings. The simulator pulse (dashed) has slightly shorter time period than the experimental. As mentioned in the Chapter 5, this effect can be attributed the fact that the higher frequencies in the signal are more attenuated than the attenuation considered at the center-frequency. And the lower ones are less attenuated than considered in our simulator.

- Inversion.
  - Our inversion procedure could have been more comprehensive. We took the manufacturer specified values for all the parameters except the thicknesses. In reality there could be deviations of these parameters from the manufacturer specified values. Ideally we should fit all the parameters of the model such as attenuation, velocity and so on. Of the two parameters, the output would be more sensitive to variations in attenuation coefficient than that of velocity.

– It also could be that the inversion procedure got stuck at a global minimum and that the final parameters we obtained were values close to the global minimum but not quite exactly at it.

– It is not clear how good a criterion the objective function (Mean Squared Error) to be minimized is as far as the shapes are concerned.

Chapter 8

Conclusions

In this thesis, we have studied the propagation of ultrasound waves in the presence of layered inhomogeneities. Our study has had three parts.

First, we have developed an analytical model for ultrasound longitudinal propagation in multi-skewed media. As parts of this model, we have developed closed form expressions for the field amplitude of hemi-spherical waves for: (1) transmission through a general three-layered media, (2) extension to transmission through multi-layered medium, (3) a special case of modelling the received echoes from a reflective media under two intermediate layers.

Second, we have used this model to develop a simulator for circular aperture transducers as well as linear-arrays for different media geometries. To validate the model, we performed real-life experiments on parallel tissue-mimicking phantoms with nominally known thicknesses.

Third, we have considered the inversion problem for the case of two layers on a reflective interface, where the layers are planar and parallel to the aperture. Our goal was to recover the locations of the planar interfaces for an data signal from the experimental data.

In the rest of this chapter, we describe the contributions of this work and discuss the assumptions and the limitations and the directions in which it can be extended.

8.1 Contributions

- Built a Forward Model for ultrasound propagation in multi layered layered medium
  - can handle multi-layered, skewed media
  - can handle different transducer apertures
  - considers absorption and backscattering loss in the media (but not viscosity losses)
  - has the advantages of ray-tracing - fast, parallelizable (each ray can be evaluated independently)
  - is closed-form. As a result, it is consistent and potentially more accurate than numerical evaluation of amplitudes of each ray. From the point of view of numerical inversion, derivatives can obtained faster. Specifically we do not have to evaluate derivatives by perturbing each parameter and evaluating forward function multiple times.
- built a simulator based on this model

- showed that a demodulation of the signals could be necessary before we can proceed with a numerical inversion.

8.2 Assumptions and Limitations of the Model

We show the main limitations and assumptions made and discuss them.

- Ray-tracing limitations.

  We give some preliminary calculations to show that the ray-tracing approximation is not very restricting.

  A check on the limits of ray-tracing can be done using Equation 2.15 for the field under two-layers for the nominal values of parameters for fat and muscle obtained from [20], for imaging with a 3.5 MHz transducer. With $C_1 = 1.48\frac{mm}{\mu s}$, $C_2 = 1.57\frac{mm}{\mu s}$, (that is $n = \frac{1.48}{1.57} = 0.9427$), we would get,

  $$z >> 0.2017mm \tag{8.1}$$

  That is, for depths sufficiently more than $0.2017mm$ from the boundary, the ray-tracing approximation is valid. This factor is inversely proportional to the frequency used. For example, at 7.5 MHz, we need a depth more than $0.0941mm$ making the condition even less restricting.

- Longitudinal propagation (no shear-waves considered).

  For soft-tissues, this assumption is not very stringent. Transverse or shear-waves are not transmitted very effectively through human soft-tissue [18]. However, for solid media such as bone, shear-waves are also important [1].

- Not considered viscosity loss. This is not a very big restriction for soft-tissues.

- Considered Specular Reflections only.

  In the current model, the reflection off the different interfaces have been considered specular. This is generally true of interfaces between organs. However in some cases, there could be diffuse reflection as well [18].

- Homogeneous Within Layer

  We have assumed each of the medium to be homogeneous. A more generalized model would take into account the within-tissue variations of density and velocity. The ray-tracing approach would be still valid. The rays would not be straight as they pass through a medium but would bend within the medium.

[1] For applications such as insonification through solids such as skull-bone etc, just longitudinal propagation is not valid and we need to adopt a more refined model to take into account shear-waves. Moreover the shear-wave and the longitudinal-waves cannot be analyzed independently, because the physical variables will have components due to both. For example, considering an isotropic, homogeneous medium which can support shear-waves as well as longitudinal-waves, the displacement vector $\mathbf{u}$ has a vector potential ψ as well as the scalar longitudinal potential ϕ. The displacement is given by [10], $\mathbf{u} = \nabla\phi + \nabla \times \psi$. Deriving wave-equations of the form in Equation 2.1 in ϕ as well as in ψ as given in [10] and solving for them, all the other physical variables such as displacement, stress, strain can be deduced from ϕ and ψ.

- Ignored multiple reflections

  We note that we ignored secondary and multiple levels of reflection off the interfaces because they would be highly attenuated because of large path-lengths and also have large delays. This is a standard assumption [1, 7, 21], etc.

- Bulk Model of Scattering

  We also use a bulk-measure to account for the back-scattering due to scatter-centers inside medium. There has been significant amount of work on explicit modeling of ultrasonic scattering [22, 23, 24, 25, 26], as well as the inversion [27, 28, 21, 29, 30]. This is because the scattering is an important parameter for classifying tissue and determining pathologies. However, in this work, we are interested in the echoes off the interfaces. The magnitude of back-scattering effect is far smaller than the magnitudes of specular and diffuse reflections from interfaces of organs [18]. We can try to additionally use the backscattering signatures for various tissues. However, that is added at the expense of complexity. The analysis is would be volumetric rather than surface based.

8.3 Future Work

There are some improvements we can do in the short term.

- Modeling the transducer pulse and obtaining the parameters of the model.

- Implementing the simulator in frequency domain so that we can readily incorporate the frequency-dependence of the attenuation coefficient. At present we assumed a single attenuation coefficient at the center-frequency

- Modeling the directional sensitivity of the transducer.

- More comprehensive inversion.

  Invert with respect to more parameters. The physical parameters would be attenuation, density, velocity. We could also include the parameter(s) involved in the directional sensitivity of the transducer. To encompass the more general case of multi-skewed layers, we have to include more geometric parameters such as the vertices of the segments forming the interfaces.

In the long term we could improve the model.

- More general Ray-Tracing.

  We could relax the criterion that within-layers the tissues are homogeneous. We could still take the ray-tracing approach. The rays would not be straight but continuously bend inside the medium. The trade-off is computational expense and dealing with considerably more parameters than the approach taken here.

- Finite Element methods.

  We could do a full finite element method to take into account diffraction, diffuse reflection, shear-waves, scatter-centers, viscosity and so on. The trade-off again is computational expense. Real-time inversion seems infeasible for such approaches.

- We could work on the applications of interest such as the registration with other modalities such as CT/MRI

Bibliography

[1] L. Odegaard, S. Holm, F. Teigen, and T. Kleveland, "Acoustic field simulation for arbitrarily shaped transducers in a stratified medium," in *Proceedings IEEE Ultrasonics Symposium*, pp. 1535–1538, 1994.

[2] L. M. Brekhovskikh, *Waves In Layered Media.* Academic Press, 1980.

[3] A. D. Pierce, *Acoustics: An Introduction to Its Physical Principles and Applications.* McGraw Hill, Inc, 1981.

[4] E. Hecht and A. Zajac, *Optics.* Addison-Wesley Publishing Company, 1974.

[5] L. Odegaard, S. Holm, and H. Torp, "Phase aberration correction applied to annular array transducers when focusing through a stratified medium," in *Proceedings IEEE Ultrasonics Symposium*, pp. 1159–1162, 1993.

[6] D. A. Carpenter, D. E. Robinson, P. L. Ho, D. Martin, and P. Isaacs, "Body wall aberration correction in medical ultrasonic images using

synthetic-aperture data," in *Proceedings IEEE Ultrasonics Symposium*, pp. 1131–1134, 1993.

[7] G. Kossoff, D. Carpenter, D. Robinson, D. Ostry, and P. Ho, "A sonographic technique to reduce beam distortion by curved transducers," *Ultrasound in Medicine and Biology*, vol. 15, no. 4, pp. 375–382, 1989.

[8] D. Carpenter, G. Kossoff, and K. A. Griffiths, "Correction of distortion in us images caused by subcutaneous tissues: Results in tissue phantoms and human subjects," *Radiology*, vol. 195, pp. 563–567, May 1995.

[9] S. Smith, G. Trahey, and O. V. Ramm, "Phased array ultrasound imaging through planar tissue layers," *Ultrasound in Medicine and Biology*, vol. 12, no. 3, pp. 229–243, 1986.

[10] G. S. Kino, *Acoustic Waves: Devices, Imaging, And Analog Signal Processing*. Prentice-Hall, Inc, 1987.

[11] J. W. Goodman, *Introduction to Fourier Optics*. McGraw Hill, Inc, 1968.

[12] P. M. Morse and K. U. Ingard, *Theoretical Acoustics*. McGraw Hill, Inc, 1968.

[13] G. P. Harris, "Review of transient field theory for a baffled planar piston," *Journal of Acoustical Society of America*, vol. 70, no. 1, pp. 10–20, 1981.

[14] G. E. Tupholme, "Generation of acoustic pulses by baffled plane pistons," *Mathematika*, vol. 16, pp. 209–224, 1969.

[15] D. A. Christensen, *Ultrasonic Bioinstrumentation.* John Wiley & Sons, 1988.

[16] A. Macovski, "Ultrasonic imaging using arrays," *Proceedings of the IEEE*, vol. 67, pp. 484–495, April 1979.

[17] E. B. Miller and F. L. Thurstone, "Linear ultrasonic array design for echosonography," *Journal of Acoustical Society of America*, vol. 61, pp. 1481–1491, June 1977.

[18] J. A. Zagzebski, *Essentials of Ultrasound Physics.* Mosby-Year Book, Inc, 1996.

[19] W. H. Press, B. P. Flannery, S. A. Teukolsky, and W. T. Vetterling, *Numerical Recipes in C.* Cambridge University Press, 1988.

[20] S. A. Goss, R. L. Johnston, and F. Dunn, "A comprehensive compilation of empirical ultrasonic properties of mammalian tissues," *Journal of Acoustical Society of America*, vol. 64, pp. 423–457, August 1978.

[21] E. J. Ayme-Bellegarda and T. M. Habashy, "Ultrasonic inverse scattering of multidimensional objects buried in multilayered elastic background structures," *IEEE Transactions on Ultrasonics, Ferroelectrics and Frequency Control*, vol. 39, pp. 11–18, January 1992.

[22] O. Bozma and R. Kuc, "Characterizing pulses reflected from rough surfaces using ultrasound," *Journal of Acoustical Society of America*, vol. 89, pp. 2519–2531, June 1991.

[23] J. Jensen, "A model for the propagation and scattering of ultrasound in tissue," *Journal of Acoustical Society of America*, vol. 89, pp. 182–190, January 1991.

[24] J. Jensen, "Deconvolution of ultrasound images," *Journal of Acoustical Society of America*, vol. 14, pp. 1–15, 1992.

[25] L. M. Hinkelman, D. Liu, L. A. Metley, and R. C. Waag, "Measurements of ultrasonic pulse arrival time and energy level variations produced by propagation through abdominal wall," *Journal of Acoustical Society of America*, vol. 95, no. 1, pp. 530–541, 1994.

[26] L. M. Hinkelman, T. L. Szabo, and R. C. Waag, "Measurements of ultrasonic pulse distortion produced by human chest wall," *Journal of Acoustical Society of America*, vol. 101, pp. 2365–2373, April 1997.

[27] Y. Li, "Phase aberration correction using near-field signal redundancy - part i: Principles," *IEEE Transactions on Ultrasonics, Ferroelectrics and Frequency Control*, vol. 44, pp. 355–371, March 1997.

[28] Y. Li, D. Robinson, and D. Carpenter, "Phase aberration correction using near-field signal redundancy - part ii: Experimental results," *IEEE Transactions on Ultrasonics, Ferroelectrics and Frequency Control*, vol. 44, pp. 372–379, March 1997.

[29] O. Haddadin and E. Ebbini, "Self-focusing arrays for imaging and therapy through inhomogeneous media," in *Proceedings IEEE Ultrasonics Symposium*, pp. 1563–1566, 1996.

[30] O. Haddadin and E. Ebbini, "Solution to the inverse scattering problem using a modified distorted born iterative algorithm," in *Proceedings IEEE Ultrasonics Symposium*, pp. 1411–1414, 1995.

[31] A. S. Glassner, *An Introduction to Ray Tracing.* London : Academic, 1989.

Appendix A

Derivation of Sides of Cross-sectional Triangles For Flux-Tube

In this chapter the goal is to derive the expressions of various differential vectors (and their lengths) in the different media. In the first section we consider the differential vectors by varying in the $d\psi$-direction. In a subsequent section we adapt these results for the $d\eta$-direction. Both these sections consider only three media. In the last section we find the recursive equations to extend to multiple media.

A.1 Differential vectors in $d\psi$-direction for three media

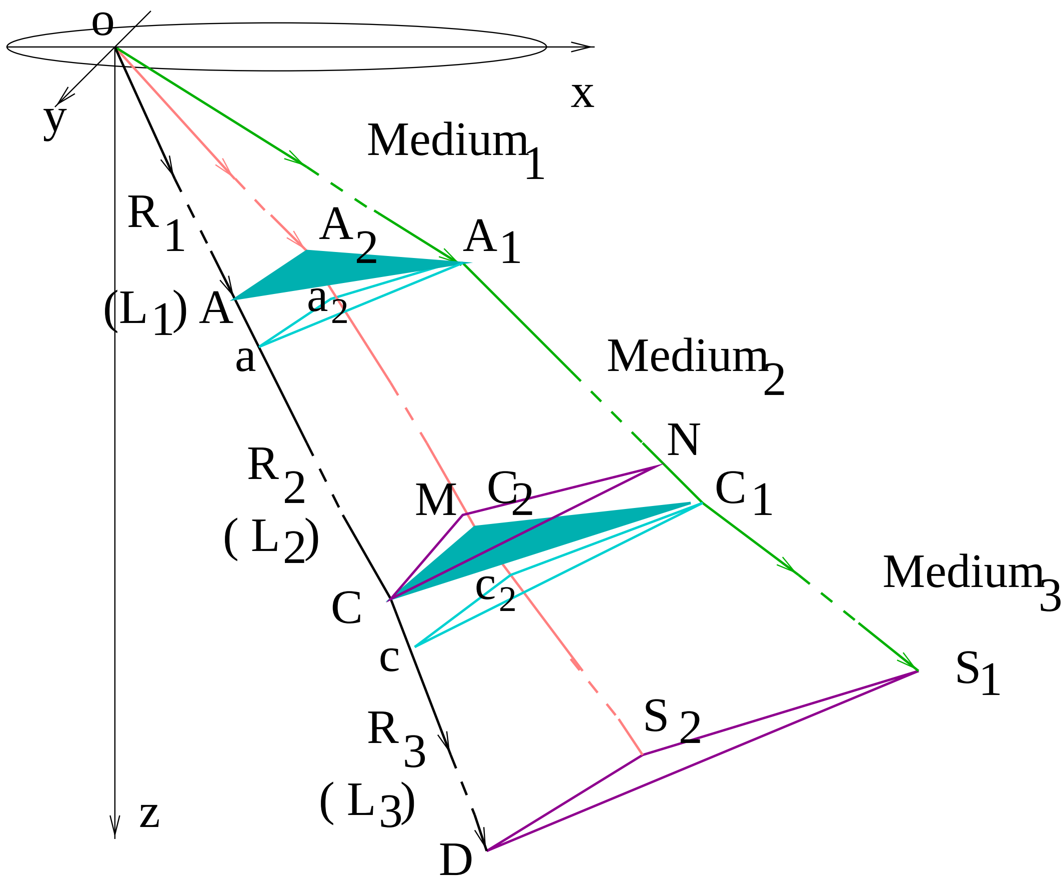

Figure A.1: **Areas of Energy Conservation**

For convenience, we repeat Figure 3.3 in the main text here, shown in Figure A.1.

The eventual goal is to obtain the ratios of the areas orthogonal to the ray. In this appendix, we obtain the various sides of the relevant triangles in order to obtain these areas.

The analysis in this section corresponds to the vectors obtained by variation of the main-ray through angle $d\psi$ (shown in Figure A.2). The differentially shifted is in the plane of the z-axis and the original ray $\mathbf{R_1}$. We note that $\mathbf{R_1}$, $\mathbf{R_2}$ and $\mathbf{n_1}$ are coplanar. And the differentially shifted ray, $\mathbf{OA_1}$, $\mathbf{n_1}$ and refracted ray thereof $\mathbf{A_1C_1}$ are coplanar. However, we cannot say the two refracted rays themselves $\mathbf{R_2}$ and $\mathbf{A_1C_1}$ are not. This same observation holds in subsequent stages.

We want to derive the various differential lengths to the common measure $d\psi$, so that when considering ratios, this quantity is cancelled. Similar analysis holds for the vectors swept out by variation of main-ray through angle $d\eta$, in an orthogonal direction (not shown here for convenience). The equations would be the same in form, except that the variable is η and we want to reduce the various differential lengths to the common measure $d\eta$.

We are interested in the lengths perpendicular to the points just above the interfaces, vectors such as $\mathbf{DS_1}$, as shown in Figure A.2. Also the vectors perpendicular to the rays just below the interfaces, ie, vectors such as $\mathbf{aA_1}, \mathbf{cC_1}$. We derive the vectors $\mathbf{aA_1}$ and $\mathbf{DS_1}$ because they are the most relevant in the main text. But their derivation, (specially that of $\mathbf{DS_1}$) shows how the vectors at any point can be arrived in general. This generalization and extension to multiple media is derived at another section.

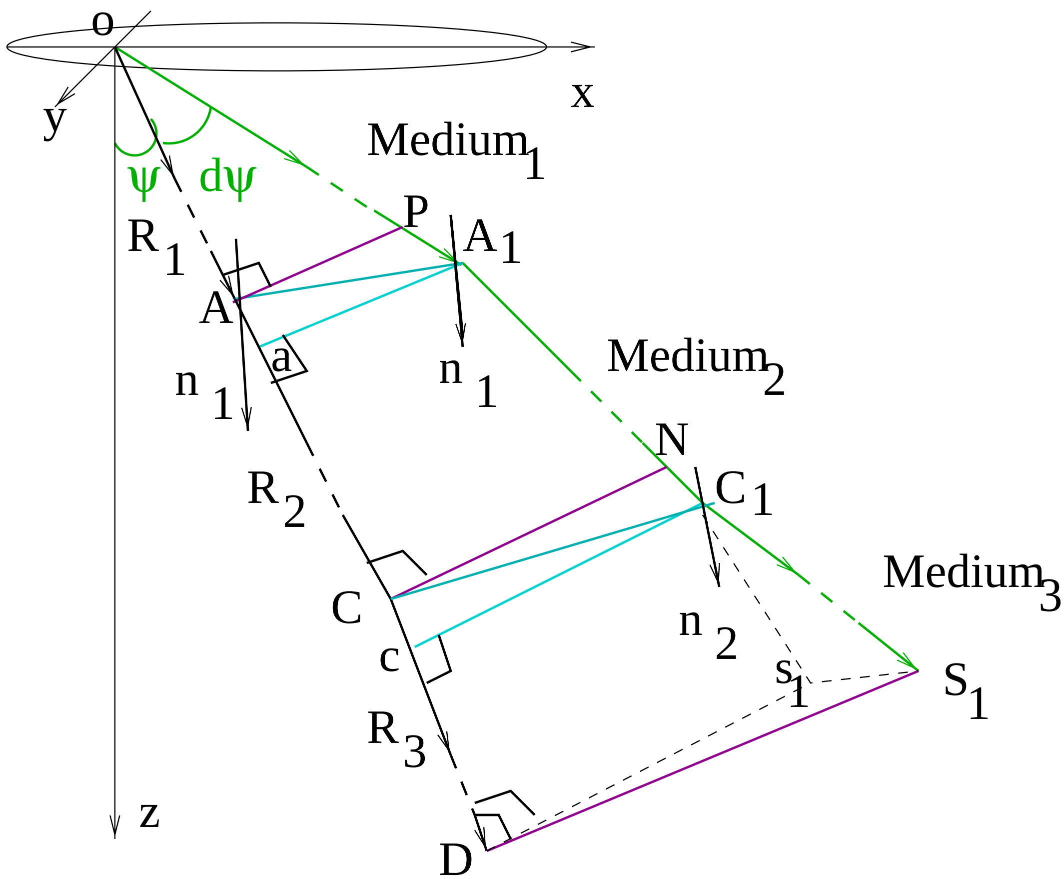

Figure A.2: **Calculation of Differential Vectors**

The vectors that are needed in the main text are marked in boxes.

The vector $\mathbf{R_1}$ is given by

$$\mathbf{R_1} = L_1 \hat{\mathbf{R_1}} \tag{A.1}$$

$$= L_1 \begin{pmatrix} \sin\psi\cos\eta \\ \sin\psi\sin\eta \\ \cos\psi \end{pmatrix} \tag{A.2}$$

$$\tag{A.3}$$

The "hat" over the vectors denotes unit-vectors.

The change in direction of $\mathbf{R_1}$ is given by,

$$\boxed{\begin{aligned} \delta_\psi \hat{\mathbf{R_1}} &= \frac{\partial \hat{\mathbf{R_1}}}{\partial \psi} d\psi \\ &= d\psi \begin{pmatrix} \cos\psi\cos\eta \\ \cos\psi\sin\eta \\ -\sin\psi \end{pmatrix} && \text{(A.4)} \\ &= (d\psi)\hat{\mathbf{x}}_{\mathbf{1}\psi} && \text{(A.5)} \end{aligned}}$$

where the unit-vector $\hat{\mathbf{x}}_{\mathbf{1}\psi}$ is given by

$$\boxed{\hat{\mathbf{x}}_{\mathbf{1}\psi} = \begin{pmatrix} \cos\psi\cos\eta \\ \cos\psi\sin\eta \\ -\sin\psi \end{pmatrix} \qquad \text{(A.6)}}$$

The suffix ψ on δ and other differential variables indicates that the derivative is with respect to ψ.

The vector $\hat{\mathbf{R}}_\mathbf{1}$ is a directional change perpendicular to the ray $\mathbf{R_1}$ (along $\hat{\mathbf{x}}_{\mathbf{1}\psi}$) and is of length d$\psi$. This vector and $\hat{\mathbf{x}}_{\mathbf{1}\psi}$ is a key building block for the others we want to derive.

The first vector we are interested in is $\mathbf{aA_1}$. From the Figure A.2, we see that it is the difference of two vectors as follows,

$$
\begin{aligned}
\mathbf{aA_1} &= \mathbf{AA_1} - \mathbf{Aa} \\
&= (\delta_\psi \mathbf{P_A}) - ((\delta_\psi \mathbf{P_A}) \cdot \hat{\mathbf{R}}_\mathbf{2})\hat{\mathbf{R}}_\mathbf{2} \qquad \text{(A.7)}
\end{aligned}
$$

where $\delta_\psi \mathbf{P_A}$ is the vectorial shift in the point of intersection $\mathbf{P_A}$ of ray $\mathbf{R_1}$ and the first planar segment when the $\mathbf{R_1}$ is changed by angle dψ. We have to derive $\hat{\mathbf{R}}_\mathbf{2}$ and $\delta_\psi \mathbf{P_A}$ next to obtain $\mathbf{aA_1}$.

The unit-vector $\hat{\mathbf{R}}_\mathbf{2}$ is the refracted ray, co-planar with $\hat{\mathbf{R}}_\mathbf{2}$ and $\mathbf{n_1}$. It can be derived as a linear sum of vectors $\hat{\mathbf{R}}_\mathbf{2}$ and $\mathbf{n_1}$. Following derivation of refracted ray in terms of incident ray and the normal, given in [31], we get,

$$
\boxed{\hat{\mathbf{R}}_\mathbf{2} = \frac{1}{n}\hat{\mathbf{R}}_\mathbf{1} + [\cos\theta_1 - \frac{\cos\theta}{n}]\mathbf{n_1} \qquad \text{(A.8)}}
$$

where n is the relative refractive index between the two media, θ is the angle of incidence ($\cos\theta = \mathbf{n_1} \cdot \hat{\mathbf{R}}_\mathbf{1}$) and θ_1 is the angle of refraction ($\cos\theta_1 = \mathbf{n_1} \cdot \hat{\mathbf{R}}_\mathbf{2}$). The two angles are related by Snell's Law, $\sin\theta = n\sin\theta_1$

We derive the $\delta_\psi \mathbf{P_A}$ as follows. The point $\mathbf{P_A}$ is given by

$$\mathbf{P_A} = \hat{\mathbf{R}}_\mathbf{1} t_1 \tag{A.9}$$

where $t_1 = L_1$ is the scale along $\mathbf{R_1}$.

Hence, $\delta_\psi \mathbf{P_A}$ is given by,

$$\begin{aligned} \delta_\psi \mathbf{P_A} &= \hat{\mathbf{R}}_\mathbf{1} dt_1 + t_1(\delta_\psi \hat{\mathbf{R}}_\mathbf{1}) \\ &= \hat{\mathbf{R}}_\mathbf{1} dt_1 + L_1(d\psi)\hat{\mathbf{x}}_{\mathbf{1}\psi} \end{aligned} \tag{A.10}$$

To find t_1 we intersect the ray and the plane (with unit-normal $\mathbf{n_1}$). Any point $\mathbf{X}$ on the plane satisfies the relation,

$$\mathbf{n_1} \cdot \mathbf{X} + D_1 = 0 \tag{A.11}$$

where D_1 is the distance of the plane from the origin.

Then putting $\mathbf{X} = t_1 \hat{\mathbf{R}}_\mathbf{1}$, we would get,

$$t_1 = -\frac{D_1}{\mathbf{n_1} \cdot \hat{\mathbf{R}}_\mathbf{1}} \tag{A.12}$$

$$\begin{aligned} dt_1 &= \frac{D_1(\mathbf{n_1} \cdot (\delta_\psi \hat{\mathbf{R}}_\mathbf{1}))}{(\mathbf{n_1} \cdot \hat{\mathbf{R}}_\mathbf{1})^2} \\ &= -\frac{t_1(\mathbf{n_1} \cdot (\delta_\psi \hat{\mathbf{R}}_\mathbf{1}))}{(\mathbf{n_1} \cdot \hat{\mathbf{R}}_\mathbf{1})} \\ &= -\frac{L_1(d\psi)(\mathbf{n_1} \cdot \hat{\mathbf{x}}_{\mathbf{1}\psi})}{(\mathbf{n_1} \cdot \hat{\mathbf{R}}_\mathbf{1})} \end{aligned} \tag{A.13}$$

(where the last but one step is obtained from the previous Equation A.12 for t_1). We note that this dt_1 expression can be intuitively obtained geometrically as well.

We can put this last Equation A.13 in Equation A.10 and get,

$$\delta_\psi \mathbf{P_A} = L_1 d\psi[\hat{\mathbf{x}}_{\mathbf{1}\psi} - \frac{(\mathbf{n_1} \cdot \hat{\mathbf{x}}_{\mathbf{1}\psi})}{(\mathbf{n_1} \cdot \hat{\mathbf{R}}_\mathbf{1})}\hat{\mathbf{R}}_\mathbf{1}] \tag{A.14}$$

Hence we can arrive at the expression for the required vector $\mathbf{aA_1}$ in terms of known quantities, and dψ by putting $\delta_\psi \mathbf{P_A}$ in Equation A.7.

$$\boxed{\begin{aligned} \mathbf{aA_1} &= L_1 d\psi[\hat{\mathbf{x}}_{\mathbf{1}\psi} - \frac{(\mathbf{n_1} \cdot \hat{\mathbf{x}}_{\mathbf{1}\psi})}{(\mathbf{n_1} \cdot \hat{\mathbf{R}}_\mathbf{1})}\hat{\mathbf{R}}_\mathbf{1} \\ &\quad -((\hat{\mathbf{x}}_{\mathbf{1}\psi} \cdot \hat{\mathbf{R}}_\mathbf{2}) - \frac{(\mathbf{n_1} \cdot \hat{\mathbf{x}}_{\mathbf{1}\psi})(\hat{\mathbf{R}}_\mathbf{1} \cdot \hat{\mathbf{R}}_\mathbf{2})}{(\mathbf{n_1} \cdot \hat{\mathbf{R}}_\mathbf{1})})\hat{\mathbf{R}}_\mathbf{2}] \qquad (A.15) \end{aligned}}$$

where $\hat{\mathbf{R}}_\mathbf{i}$ are the ray-vectors, $\hat{\mathbf{x}}_{\mathbf{1}\psi}$ is the direction perpendicular to $\hat{\mathbf{R}}_\mathbf{1}$, given in Equation A.6. $\mathbf{n_1}$ is the normal to the first interface, and the length L_1 is the intercept of ray $\hat{\mathbf{R}}_\mathbf{1}$ at the first medium.

The other vector of interest is $\mathbf{DS_1}$. From the reference Figure we see

$$\begin{aligned} \mathbf{DS_1} &= \mathbf{Ds_1} + \mathbf{s_1 S_1} \\ &= \mathbf{cC_1} + L_3(\delta_\psi \hat{\mathbf{R}}_\mathbf{3}) \end{aligned} \tag{A.16}$$

where we make use of the fact that $\mathbf{Ds_1} = \mathbf{cC_1}$ (by construction, in Figure A.2). The ray $\mathbf{C_1 s_1}$ is parallel to $\mathbf{R_3}$ and, therefore the vector $\mathbf{s_1 S_1}$ is the increment vector, $L_3(\delta_\psi \hat{\mathbf{R}}_\mathbf{3})$. $\delta_\psi \hat{\mathbf{R}}_\mathbf{3}$ is the change in direction of the unit-vector ray $\hat{\mathbf{R}}_\mathbf{3}$. Multiplication by the length L_3 is needed to get the arc-length swept by the ray.

This Equation shows that we have derive the vector $\mathbf{cC_1}$ (which can be derived in similar way as was done for $\mathbf{aA_1}$) and $(\delta_\psi \hat{\mathbf{R}}_\mathbf{3})$. We tackle $\mathbf{cC_1}$ first.

The vector $\mathbf{cC_1}$ is given by,

$$\begin{aligned} \mathbf{cC_1} &= \mathbf{CC_1} - \mathbf{Cc} && \text{(A.17)} \\ &= \delta_\psi \mathbf{P_C} - (\hat{\mathbf{R}}_\mathbf{3} \cdot \delta_\psi \mathbf{P_C})\hat{\mathbf{R}}_\mathbf{3} && \text{(A.18)} \end{aligned}$$

First we derive vector $\mathbf{CC_1}$ as the differential of the point of intersection of $\mathbf{R_2}$ and the second interface. The point $\mathbf{P_C}$ is given vectorially by,

$$\mathbf{P_C} = \mathbf{P_A} + \hat{\mathbf{R}}_\mathbf{2} t_2 \tag{A.19}$$

where $t_2 = L_2$ denotes the scale.

Differentiating this, as we did before for $\mathbf{P_A}$, we get

$$\begin{aligned} \delta_\psi \mathbf{P_C} &= \delta_\psi \mathbf{P_A} + t_2(\delta_\psi \hat{\mathbf{R}}_\mathbf{2}) + \hat{\mathbf{R}}_\mathbf{2} dt_2 \\ &= \delta_\psi \mathbf{P_A} + (L_2)(\delta_\psi \hat{\mathbf{R}}_\mathbf{2}) + \hat{\mathbf{R}}_\mathbf{2} dt_2 \\ &= \delta_\psi \mathbf{P_A} + L_2(d\psi)\hat{\mathbf{x}}_{\mathbf{2}\psi} + \hat{\mathbf{R}}_\mathbf{2} dt_2 && \text{(A.20)} \end{aligned}$$

We know the first term from Equation A.14. The second two terms needs derivation of $\delta_\psi \hat{\mathbf{R}}_\mathbf{2}$ and dt_2.

Taking the derivative of Equation A.8, we get $\delta_\psi \hat{\mathbf{R}}_\mathbf{2}$ as

$$\delta_\psi \hat{\mathbf{R}}_\mathbf{2} = [\frac{d\psi}{n} \hat{\mathbf{x}}_{\mathbf{1}\psi} + (\delta_\psi F)\mathbf{n_1}] \tag{A.21}$$

where $F = \cos\theta_1 - \cos\theta/n$

$$\begin{aligned} \delta_\psi F &= \frac{\partial F}{\partial \psi} d\psi \\ &= d\psi(-\sin\theta_1 \frac{d\theta_1}{d\psi} + \frac{\sin\theta}{n}\frac{d\theta}{d\psi}) \end{aligned} \tag{A.22}$$

To find $d\theta/d\psi$, we remember that $\cos\theta = \mathbf{n_1} \cdot \hat{\mathbf{R}}_\mathbf{1}$.

Hence we get, $\sin\theta \frac{d\theta}{d\psi} = -\mathbf{n_1} \cdot \hat{\mathbf{x}}_{\mathbf{1}\psi}$.

We can differentiate the Snell's Law, to get the relation between $d\theta$ and $d\theta_1$.

Thus we get, $\frac{d\theta_1}{d\psi} = \frac{d\theta}{d\psi}\frac{\cos\theta}{n\cos\theta_1}$

Substituting this in Equation A.22 after a little manipulation, we would get,

$$\delta_\psi F = -\frac{d\psi}{n}(1 - \frac{\tan\theta_1}{\tan\theta})(\mathbf{n_1} \cdot \hat{\mathbf{x}}_{\mathbf{1}\psi}) \tag{A.23}$$

Putting Equation A.23 in

$$\boxed{\begin{aligned} \delta_\psi \hat{\mathbf{R}}_\mathbf{2} &= \frac{d\psi}{n}[\hat{\mathbf{x}}_{\mathbf{1}\psi} - \mathbf{n_1}(1 - \frac{\tan\theta_1}{\tan\theta})(\mathbf{n_1} \cdot \hat{\mathbf{x}}_{\mathbf{1}\psi})] && \text{(A.24)} \\ &= (d\psi)\hat{\mathbf{x}}_{\mathbf{2}\psi} && \text{(A.25)} \end{aligned}}$$

where (as was done for $\delta_\psi \hat{\mathbf{R}}_\mathbf{1}$), in the last step, we define a vector corresponding to $\delta_\psi \hat{\mathbf{R}}_\mathbf{2}$, given by

$$\hat{\mathbf{x}}_{\mathbf{2}\psi} = \frac{1}{n}[\hat{\mathbf{x}}_{\mathbf{1}\psi} - \mathbf{n_1}(1 - \frac{\tan\theta_1}{\tan\theta})(\mathbf{n_1} \cdot \hat{\mathbf{x}}_{\mathbf{1}\psi})] \quad \text{(A.26)}$$

These vectors $\hat{\mathbf{x}}_{\mathbf{1}\psi}$, $\hat{\mathbf{x}}_{\mathbf{2}\psi}$ etc, have a **recursive** relationship (as evident from Equation A.26) which will help in generalizing the proof, as shown later.

To derive the last term dt_2 in Equation A.20 we have to find t_2 as the point of intersection of the ray $\mathbf{R_2}$ and the second interface (normal $\mathbf{n_2}$) and distance D_2. As a similar derivation was shown earlier, the details are left out.

$$t_2 = -\frac{(\mathbf{n_2} \cdot \mathbf{P_A}) + D_2}{(\mathbf{n_2} \cdot \hat{\mathbf{R}}_\mathbf{2})} \quad \text{(A.27)}$$

Taking the derivative and after some manipulations, we get

$$\begin{aligned} dt_2 &= -\frac{(\mathbf{n_2} \cdot \delta_\psi \mathbf{P_A})}{(\mathbf{n_2} \cdot \hat{\mathbf{R}}_\mathbf{2})} - \frac{t_2(\mathbf{n_2} \cdot \delta_\psi \hat{\mathbf{R}}_\mathbf{2})}{(\mathbf{n_2} \cdot \hat{\mathbf{R}}_\mathbf{2})} \\ &= -\frac{(\mathbf{n_2} \cdot \delta_\psi \mathbf{P_A})}{(\mathbf{n_2} \cdot \hat{\mathbf{R}}_\mathbf{2})} - \frac{L_2(d\psi)(\mathbf{n_2} \cdot \hat{\mathbf{x}}_{\mathbf{2}\psi})}{(\mathbf{n_2} \cdot \hat{\mathbf{R}}_\mathbf{2})} \quad \text{(A.28)} \end{aligned}$$

We note that this dt_2 expression can be intuitively obtained geometrically as well.

Substituting Equation A.28 in Equation A.20 and rearranging we get,

$$\begin{aligned}\delta_\psi \mathbf{P_C} &= \delta_\psi \mathbf{P_A} - \hat{\mathbf{R}}_\mathbf{2}[\frac{(\mathbf{n_2} \cdot \delta_\psi \mathbf{P_A})}{(\mathbf{n_2} \cdot \hat{\mathbf{R}}_\mathbf{2})}] \\ &\quad + L_2(d\psi)\hat{\mathbf{x}}_{\mathbf{2}\psi} - L_2(d\psi)\hat{\mathbf{R}}_\mathbf{2}[\frac{(\mathbf{n_2} \cdot \hat{\mathbf{x}}_{\mathbf{2}\psi})}{(\mathbf{n_2} \cdot \hat{\mathbf{R}}_\mathbf{2})}] \qquad (A.29)\end{aligned}$$

This equation shows an useful **recursive** relation ($\delta_\psi \mathbf{P_C}$ in terms of $\delta_\psi \mathbf{P_A}$) to be used later.

We could get the full final form of $\delta_\psi \mathbf{P_C}$ (in terms of $d\psi$) by substituting $\delta_\psi \mathbf{P_A}$ from Equation A.14 into the above equation and rearranging,

$$\begin{aligned}\delta_\psi \mathbf{P_C} &= (d\psi)[L_1(\hat{\mathbf{x}}_{\mathbf{1}\psi} - \frac{(\mathbf{n_1} \cdot \hat{\mathbf{x}}_{\mathbf{1}\psi})}{(\mathbf{n_1} \cdot \hat{\mathbf{R}}_\mathbf{1})}\hat{\mathbf{R}}_\mathbf{1}) \\ &\quad - L_1\hat{\mathbf{R}}_\mathbf{2}(\frac{(\mathbf{n_2} \cdot \hat{\mathbf{x}}_{\mathbf{1}\psi})(\mathbf{n_1} \cdot \hat{\mathbf{R}}_\mathbf{1}) - (\mathbf{n_1} \cdot \hat{\mathbf{x}}_{\mathbf{1}\psi})(\mathbf{n_2} \cdot \hat{\mathbf{R}}_\mathbf{1}))}{(\mathbf{n_1} \cdot \hat{\mathbf{R}}_\mathbf{1})(\mathbf{n_2} \cdot \hat{\mathbf{R}}_\mathbf{2})}) \\ &\quad + L_2\hat{\mathbf{x}}_{\mathbf{2}\psi} - L_2\hat{\mathbf{R}}_\mathbf{2}\frac{(\mathbf{n_2} \cdot \hat{\mathbf{x}}_{\mathbf{2}\psi})}{(\mathbf{n_2} \cdot \hat{\mathbf{R}}_\mathbf{2})}] \qquad (A.30)\end{aligned}$$

We had set out to derive Equation A.18. We have almost got it except for an expression for $\hat{\mathbf{R}}_\mathbf{3}$. We write the latter now. From the standard formula for the refracted ray [31], we get,

$$\hat{\mathbf{R}}_\mathbf{3} = \frac{1}{n'}\hat{\mathbf{R}}_\mathbf{2} + [\cos\theta_t' - \frac{\cos\theta_t}{n'}]\mathbf{n_2} \qquad (A.31)$$

where $n' = \frac{C_2}{C_3}$ is the relative refractive index between Medium 2 and

Medium 3, θ_t is the angle of incidence and $\theta_t{}'$ is the angle of refraction. The two angles are related by Snell's Law, $\sin\theta_t = n' \sin\theta_t{}'$

Hence substituting Equation A.31 and A.30 in Equation A.18 we would get the vector $\mathbf{cC_1}$.

The original goal was to derive $\mathbf{DS_1}$ as given in Equation A.16, expanded here in Equation A.32 for convenience.

$$\begin{aligned}
\mathbf{DS_1} &= \mathbf{Ds_1} + \mathbf{s_1 S_1} \\
&= \mathbf{cC_1} + L_3(\delta_\psi \mathbf{\hat{R}_3}) \\
&= \delta_\psi \mathbf{P_C} - (\mathbf{\hat{R}_3} \cdot \delta_\psi \mathbf{P_C})\mathbf{\hat{R}_3} + L_3(\delta_\psi \mathbf{\hat{R}_3}) \qquad \text{(A.32)}
\end{aligned}$$

We derived $\delta_\psi \mathbf{P_C}$ so far. But we see that we need another factor, the differential change in the vector $\mathbf{\hat{R}_3}$. We can derive this in the same identical way as done before for $\mathbf{\hat{R}_2}$ and get,

$$\boxed{\begin{aligned}
\delta_\psi \mathbf{\hat{R}_3} &= \frac{d\psi}{n'}[\mathbf{\hat{x}_{2\psi}} - \mathbf{n_2}(1 - \frac{\tan\theta_t{}'}{\tan\theta_t})(\mathbf{n_2} \cdot \mathbf{\hat{x}_{2\psi}})] \qquad \text{(A.33)} \\
&= (d\psi)\mathbf{\hat{x}_{3\psi}} \qquad \text{(A.34)}
\end{aligned}}$$

where (as was done for $\delta_\psi \mathbf{\hat{R}_1}$ and $\delta_\psi \mathbf{\hat{R}_2}$), in the last step, we define a vector corresponding to $\delta_\psi \mathbf{\hat{R}_3}$, given by

$$\boxed{\mathbf{\hat{x}_{3\psi}} = \frac{1}{n'}[\mathbf{\hat{x}_{2\psi}} - \mathbf{n_2}(1 - \frac{\tan\theta_t{}'}{\tan\theta_t})(\mathbf{n_2} \cdot \mathbf{\hat{x}_{2\psi}})] \qquad \text{(A.35)}}$$

We can therefore substitute Equations A.34 and A.30 in Equation A.32 to arrive at the vector $\mathbf{DS_1}$.

A.2 Differential vectors in dη-direction for three media

The analysis for the dη-direction is similar to last section, except we take the differentials with respect to dη and not dψ. The figure in the main text illustrating the flux-tube Figure A.1 is referred to when necessary instead of drawing a separate diagram showing the dη-ray exclusively. We write the final results here without detailed analysis, except when it is necessary to explain and illustrate a point of difference, specially when deriving the vector $\mathbf{DS_2}$.

The vector $\mathbf{R_1}$ is given in Equation A.3, reproduced here again for convenience.

$$
\begin{aligned}
\mathbf{R_1} &= L_1 \hat{\mathbf{R_1}} && \text{(A.36)} \\
&= L_1 \begin{pmatrix} \sin\psi\cos\eta \\ \sin\psi\sin\eta \\ \cos\psi \end{pmatrix} && \text{(A.37)} \\
& && \text{(A.38)}
\end{aligned}
$$

The "hat" over the vectors denotes unit-vectors as before.

The change in direction of $\mathbf{R_1}$ is given by,

$$
\begin{aligned}
\delta_\eta \hat{\mathbf{R}}_{\mathbf{1}} &= \frac{\partial \hat{\mathbf{R}}_{\mathbf{1}}}{\partial \eta} d\eta \\
&= d\eta \begin{pmatrix} -\sin\psi \sin\eta \\ \sin\psi\cos\eta \\ 0 \end{pmatrix} && \text{(A.39)} \\
&= (d\eta)\hat{\mathbf{x}}_{\mathbf{1}\eta} && \text{(A.40)}
\end{aligned}
$$

where the unit-vector $\hat{\mathbf{x}}_{\mathbf{1}\eta}$ is given by

$$
\hat{\mathbf{x}}_{\mathbf{1}\psi} = \begin{pmatrix} -\sin\psi \sin\eta \\ \sin\psi\cos\eta \\ 0 \end{pmatrix} \quad \text{(A.41)}
$$

The suffix η on δ and other differential variables indicates that the derivative is with respect to η.

The change in the point of intersection (of $\mathbf{R_1}$ and first interface) $\mathbf{P_A}$, is given by

$$
\delta_\eta \mathbf{P_A} = L_1 d\eta[\hat{\mathbf{x}}_{\mathbf{1}\eta} - \frac{(\mathbf{n_1} \cdot \hat{\mathbf{x}}_{\mathbf{1}\eta})}{(\mathbf{n_1} \cdot \hat{\mathbf{R}}_{\mathbf{1}})}\hat{\mathbf{R}}_{\mathbf{1}}] \quad \text{(A.42)}
$$

The vector $\mathbf{aa_2}$ (refer to Figure A.3) is almost identical in length and direction to $\mathbf{a}^{'}\mathbf{A_2}$ (drawn perpendicular to ray $\mathbf{R_2}$ from point $\mathbf{A_2}$). The difference between these two vectors, $\mathbf{aa_2}$ and $\mathbf{a}^{'}\mathbf{A_2}$ is of second order of length (arc swept by a differential length in going through a differential angle).

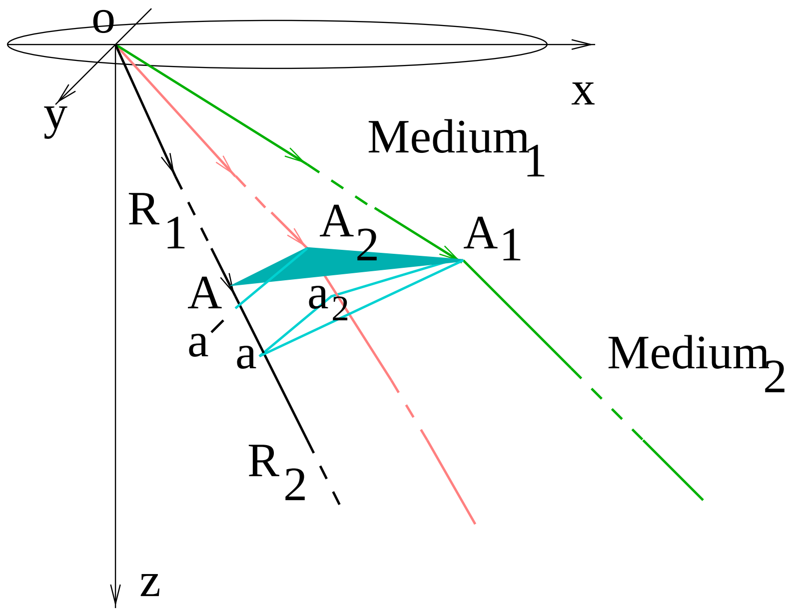

Figure A.3: **Vectors $\mathbf{a'A_2}$ and $\mathbf{aa_2}$**

Hence we can derive the vector $\mathbf{aa_2}$ as

$$
\boxed{
\begin{aligned}
\mathbf{aa_2} &= \mathbf{a'A_2} \\
&= \mathbf{AA_2} - \mathbf{Aa'} \\
&= (\delta_\eta \mathbf{P_A}) - ((\delta_\eta \mathbf{P_A}) \cdot \hat{\mathbf{R}}_2)\hat{\mathbf{R}}_2 \\
&= L_1 d\eta[\hat{\mathbf{x}}_{1\eta} - \frac{(\mathbf{n_1} \cdot \hat{\mathbf{x}}_{1\eta})}{(\mathbf{n_1} \cdot \hat{\mathbf{R}}_1)}\hat{\mathbf{R}}_1 \\
&\quad -((\hat{\mathbf{x}}_{1\eta} \cdot \hat{\mathbf{R}}_2) - \frac{(\mathbf{n_1} \cdot \hat{\mathbf{x}}_{1\eta})(\hat{\mathbf{R}}_1 \cdot \hat{\mathbf{R}}_2)}{(\mathbf{n_1} \cdot \hat{\mathbf{R}}_1)})\hat{\mathbf{R}}_2] \qquad \text{(A.43)}
\end{aligned}
}
$$

The $\hat{\mathbf{R}}_2$ is given in Equation A.8. Taking the derivative with respect to dη, we would get,

$$\delta_\eta \hat{\mathbf{R}}_{\mathbf{2}} = \frac{d\eta}{n}[\hat{\mathbf{x}}_{\mathbf{1}\eta} - \mathbf{n}_{\mathbf{1}}(1 - \frac{\tan\theta_1}{\tan\theta})(\mathbf{n}_{\mathbf{1}} \cdot \hat{\mathbf{x}}_{\mathbf{1}\eta})] \quad (A.44)$$

$$= (d\eta)\hat{\mathbf{x}}_{\mathbf{2}\eta} \quad (A.45)$$

where (as was done for $\delta_\eta \hat{\mathbf{R}}_{\mathbf{1}}$), in the last step, we define a vector corresponding to $\delta_\eta \hat{\mathbf{R}}_{\mathbf{2}}$, given by

$$\hat{\mathbf{x}}_{\mathbf{2}\eta} = \frac{1}{n}[\hat{\mathbf{x}}_{\mathbf{1}\eta} - \mathbf{n}_{\mathbf{1}}(1 - \frac{\tan\theta_1}{\tan\theta})(\mathbf{n}_{\mathbf{1}} \cdot \hat{\mathbf{x}}_{\mathbf{1}\eta})] \quad (A.46)$$

The next step involves derivation of the change in the point of intersection (of $\mathbf{R}_{\mathbf{2}}$ and second interface) $\mathbf{P}_{\mathbf{C}}$. This follows, similar to derivation of Equations A.29 and A.30. We would get, therefore,

$$\delta_\eta \mathbf{P}_{\mathbf{C}} = \delta_\eta \mathbf{P}_{\mathbf{A}} - \hat{\mathbf{R}}_{\mathbf{2}}[\frac{(\mathbf{n}_{\mathbf{2}} \cdot \delta_\eta \mathbf{P}_{\mathbf{A}})}{(\mathbf{n}_{\mathbf{2}} \cdot \hat{\mathbf{R}}_{\mathbf{2}})}] + L_2(d\eta)\hat{\mathbf{x}}_{\mathbf{2}\eta} - L_2(d\eta)\hat{\mathbf{R}}_{\mathbf{2}}[\frac{(\mathbf{n}_{\mathbf{2}} \cdot \hat{\mathbf{x}}_{\mathbf{2}\eta})}{(\mathbf{n}_{\mathbf{2}} \cdot \hat{\mathbf{R}}_{\mathbf{2}})}] \quad (A.47)$$

And by substituting $\delta_\eta \mathbf{P}_{\mathbf{A}}$ from Equation A.42 we would get,

$$
\begin{aligned}
\delta_\eta \mathbf{P_C} &= (d\eta)[L_1(\hat{\mathbf{x}}_{\mathbf{1}\eta} - \frac{(\mathbf{n_1}\cdot\hat{\mathbf{x}}_{\mathbf{1}\eta})}{(\mathbf{n_1}\cdot\hat{\mathbf{R}}_\mathbf{1})}\hat{\mathbf{R}}_\mathbf{1}) \\
&\quad - L_1\hat{\mathbf{R}}_\mathbf{2}(\frac{(\mathbf{n_2}\cdot\hat{\mathbf{x}}_{\mathbf{1}\eta})(\mathbf{n_1}\cdot\hat{\mathbf{R}}_\mathbf{1}) - (\mathbf{n_1}\cdot\hat{\mathbf{x}}_{\mathbf{1}\eta})(\mathbf{n_2}\cdot\hat{\mathbf{R}}_\mathbf{1}))}{(\mathbf{n_1}\cdot\hat{\mathbf{R}}_\mathbf{1})(\mathbf{n_2}\cdot\hat{\mathbf{R}}_\mathbf{2})}) \\
&\quad + L_2\hat{\mathbf{x}}_{\mathbf{2}\eta} - L_2\hat{\mathbf{R}}_\mathbf{2}\frac{(\mathbf{n_2}\cdot\hat{\mathbf{x}}_{\mathbf{2}\eta})}{(\mathbf{n_2}\cdot\hat{\mathbf{R}}_\mathbf{2})}]
\end{aligned}
\tag{A.48}
$$

Next we attempt to derive the vector $\mathbf{DS_2}$ in Figure A.1.

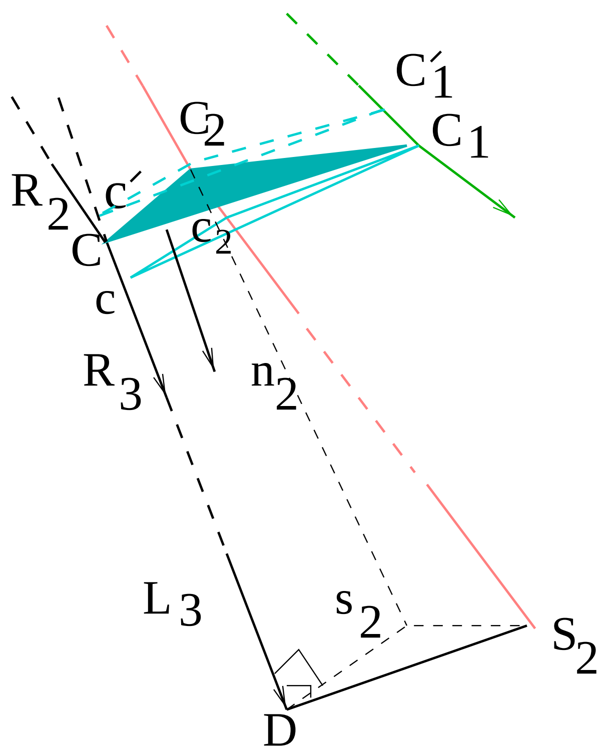

Figure A.4: **Construction of $\mathbf{DS_2}$**

Parts of Figure A.1 are redrawn in Figure A.4 for clarity and further construction. In Figure A.4 $\Delta\mathbf{cc_2C_1}$ is the triangle formed by the points where the three-rays intersect the plane orthogonal to $\mathbf{R_3}$ passing through $\mathbf{C_1}$. In the main text, we show that ignoring second order differentials, this is a projection onto that orthogonal plane, passing through the point $\mathbf{C_1}$. In Figure A.4, we similarly get the triangle at $\mathbf{C_2}$, orthogonal to the ray $\mathbf{R_3}$, (extended backwards in dotted lines), meeting the other two rays at $\mathbf{c}'$, and $\mathbf{C_1}'$, respectively. This is also a projection, if we ignore second-order differentials. Hence, the two triangles $\Delta\mathbf{cc_2C_1}$ and $\Delta\mathbf{c}'\mathbf{C_2C_1}'$ (shown in dotted lines) are congruent (to first order of differentials).

To get the vector $\mathbf{DS_2}$ we concentrate on the dotted triangle, $\Delta\mathbf{c}'\mathbf{C_2C_1}'$ in Figure A.4.

$$\begin{aligned}\mathbf{DS_2} &= \mathbf{D}\mathrm{s}_\mathbf{2} + \mathrm{s}_\mathbf{2}\mathbf{S_2} \\ &= \mathbf{c}'\mathbf{C_2} + L_3(\delta_\eta\hat{\mathbf{R}}_\mathbf{3}) \qquad (A.49)\end{aligned}$$

$\mathbf{C_2S_2}$ is parallel to $\mathbf{R_3}$ and plane $\mathbf{D}\mathrm{s}_\mathbf{2}\mathbf{S_2}$ is orthogonal to $\mathbf{R_3}$ and $\delta_\eta\hat{\mathbf{R}}_\mathbf{3}$ is the differential change in direction of $\hat{\mathbf{R}}_\mathbf{3}$.

But, $\mathbf{c}'\mathbf{C_2}$ is given by,

$$\mathbf{c}'\mathbf{C_2} = \mathbf{CC_2} - \mathbf{Cc}' \qquad (A.50)$$

$$= \delta_\eta\mathbf{P_C} - (\hat{\mathbf{R}}_\mathbf{3}\cdot\delta_\eta\mathbf{P_C})\hat{\mathbf{R}}_\mathbf{3} \qquad (A.51)$$

We know $\delta_\eta\mathbf{P_C}$ from Equation A.48 and $\hat{\mathbf{R}}_\mathbf{3}$ from Equation A.31.

Substituting Equation A.51 in the Equation for $\mathbf{DS_2}$ we would get,

$$\mathbf{DS_2} = \delta_\eta \mathbf{P_C} - (\hat{\mathbf{R}}_\mathbf{3} \cdot \delta_\eta \mathbf{P_C})\hat{\mathbf{R}}_\mathbf{3} + L_3(\delta_\eta \hat{\mathbf{R}}_\mathbf{3}) \tag{A.52}$$

We are yet to derive the last term, in Equation A.52, involving $\delta_\eta \hat{\mathbf{R}}_\mathbf{3}$. We can proceed as in previous section and to get,

$$\delta_\eta \hat{\mathbf{R}}_\mathbf{3} = \frac{d\eta}{n'}[\hat{\mathbf{x}}_{\mathbf{2}\eta} - \mathbf{n_2}(1 - \frac{\tan\theta_t{}'}{\tan\theta_t})(\mathbf{n_2} \cdot \hat{\mathbf{x}}_{\mathbf{2}\eta})] \tag{A.53}$$

$$= (d\eta)\hat{\mathbf{x}}_{\mathbf{3}\eta} \tag{A.54}$$

where (as was done for $\delta_\eta \hat{\mathbf{R}}_\mathbf{1}$ and $\delta_\eta \hat{\mathbf{R}}_\mathbf{2}$), in the last step, we define a vector corresponding to $\delta_\eta \hat{\mathbf{R}}_\mathbf{3}$, given by

$$\hat{\mathbf{x}}_{\mathbf{3}\eta} = \frac{1}{n'}[\hat{\mathbf{x}}_{\mathbf{2}\eta} - \mathbf{n_2}(1 - \frac{\tan\theta_t{}'}{\tan\theta_t})(\mathbf{n_2} \cdot \hat{\mathbf{x}}_{\mathbf{2}\eta})] \tag{A.55}$$

We can therefore substitute Equation A.48 and A.31 and Equations A.54 in Equation A.52 to arrive at the vector $\mathbf{DS_2}$.

A.3 Generalization to multiple media

The last two sections shows an underlying recursive pattern. We can derive a vector in the i-the layer in terms of vectors related to the $i-1$-th layer. In this section we explicitly write the recursive relations. The details of the analysis are the same as last two sections and hence left out. The differentials are with respect to a general angle ν.

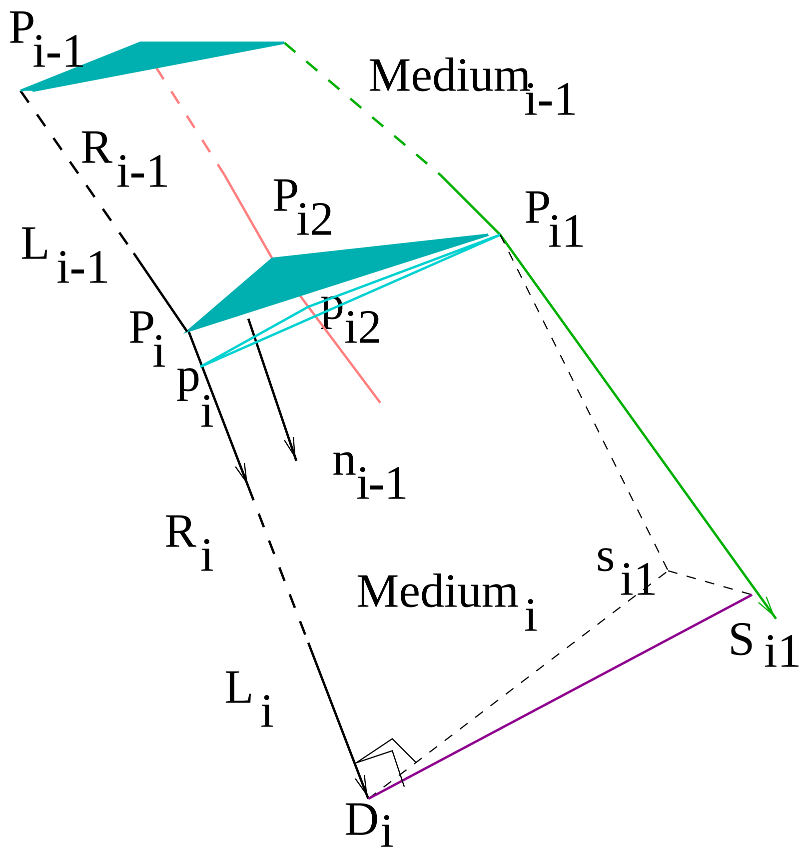

Figure A.5: **Recursive Relations**

$$\begin{aligned}\mathbf{P_i} &= \mathbf{P_{i-1}} + \hat{\mathbf{R}}_{\mathbf{i-1}} t_{i-1} \\ &= \mathbf{P_{i-1}} + \hat{\mathbf{R}}_{\mathbf{i-1}} L_{i-1}\end{aligned} \tag{A.56}$$

Taking the derivative, we get

$$
\begin{aligned}
\delta_\nu \mathbf{P_i} &= \delta_\nu \mathbf{P_{i-1}} + L_{i-1}(\delta_\nu \mathbf{\hat{R}_{i-1}}) + \mathbf{\hat{R}_{i-1}} dL_{i-1} \\
&= \delta_\nu \mathbf{P_{i-1}} + L_{i-1}(d\nu)\mathbf{\hat{x}_{i-1}}_\nu \\
&\quad -\mathbf{\hat{R}_{i-1}}[\frac{(\mathbf{n_{i-1}} \cdot \delta_\nu \mathbf{P_{i-1}})}{(\mathbf{n_{i-1}} \cdot \mathbf{\hat{R}_{i-1}})} + L_{i-1} d\nu \frac{(\mathbf{n_{i-1}} \cdot \mathbf{\hat{x}_{i-1}}_\nu)}{(\mathbf{n_{i-1}} \cdot \mathbf{\hat{R}_{i-1}})}] \\
&= \delta_\nu \mathbf{P_{i-1}} - \mathbf{\hat{R}_{i-1}}[\frac{(\mathbf{n_{i-1}} \cdot \delta_\nu \mathbf{P_{i-1}})}{(\mathbf{n_{i-1}} \cdot \mathbf{\hat{R}_{i-1}})}] \\
&\quad + L_{i-1}(d\nu)\mathbf{\hat{x}_{i-1}}_\nu - L_{i-1}(d\nu)\mathbf{\hat{R}_{i-1}} \frac{(\mathbf{n_{i-1}} \cdot \mathbf{\hat{x}_{i-1}}_\nu)}{(\mathbf{n_{i-1}} \cdot \mathbf{\hat{R}_{i-1}})}
\end{aligned}
\tag{A.57}
$$

Where the vector $\mathbf{x_i}$ is defined as follows and follows a recursive relation as well.

$$
\delta_\nu \mathbf{\hat{R}_i} = (d\nu)\mathbf{\hat{x}_i}_\nu \tag{A.58}
$$

where $\mathbf{\hat{x}_i}_\nu$ is given by

$$
\mathbf{\hat{x}_i}_\nu = \frac{1}{n_{i-1}}[\mathbf{\hat{x}_{i-1}}_\nu - \mathbf{n_{i-1}}(1 - \frac{\tan\theta_{i-1}{}'}{\tan\theta_i})(\mathbf{n_{i-1}} \cdot \mathbf{\hat{x}_{i-1}}_\nu)] \tag{A.59}
$$

The final length we want can be obtained in terms of all these vectors as,

$$
\mathbf{DS_{i1}} = \delta_\nu \mathbf{P_i} - (\mathbf{\hat{R}_i} \cdot \delta_\nu \mathbf{P_i})\mathbf{\hat{R}_i} + L_i(\delta_\nu \mathbf{\hat{R}_i}) \tag{A.60}
$$